Dynamic Modeling of Crack Propagation in Ceramic Laminate-Toughened Composites with Weak Interfaces by Using Discrete Element Method

Von der Fakultät für Georessourcen und Materialtechnik

der Rheinisch -Westfälischen Technischen Hochschule Aachen

zur Erlangung des akademischen Grades eines

Doktors der Ingenieurwissenschaften

genehmigte Dissertation

vorgelegt von **M.Sc.**

Wen Zhang

aus Hunan, China

Berichter: Univ.-Prof. Dr. rer. nat. Rainer Telle

Univ.-Prof. Dr. rer. nat. Georg Roth

Tag der mündlichen Prüfung: 19. Dezember 2013

Diese Dissertation ist auf den Internetseiten der Hochschulbibliothek online verfügbar

Acknowledgement

I wish to express my deep and sincere gratitude to many individuals, without their contribution this thesis would not have been completed.

I am very grateful to Professor Rainer Telle for his excellent guidance, valuable advice, constant encouragement and enormous patience with my progress through the years of this study. Beyond his invaluable supervising, he provided me a creative atmosphere and a working environment full of freedom which inspired and motivated me for the research. I also admire and respect his scientific vision, his attitude to the scientific work, and will always try my best to learn from him as much as I can.

Great thanks to all my dear colleagues and ex-colleagues in GHI for my most precious experiences with them. Nine years in Aachen/Germany and over 8 years in GHI, the years tell everything. Thank you all!

My gratitude to Dr. Joachim Uebel, who offered great assistance for helping me to learn and practice with the DEM software, without that this research, would be impossible. Thanks to Professor Janos Urai and Dr. Steffen Abe for their suggestion and help on the numerical modeling.

Grateful thanks go to my parents, my grandmothers, and all my family, for your endless supports.

Last but not least my deepest thanks go to my lovely wife Jingjin, for always being there for me and standing by me. Since you came to me, I made the biggest step to finish this dissertation. To Leon, my recently born son, your arrival helped daddy to make the last kick for all this, without you my life would still be the same. This thesis is dedicated to you and your mama…

Index

1. Introduction and Objective....1
1.1 Ceramic laminates with weak interfaces....1
1.1.1 Mechanical Modeling of Ceramic Laminates....4
1.1.2 Crack Deflection Criteria....5
1.2 Discrete Element Method (DEM)....6
1.2.1 Particle Flow Code in 2 Dimensions (PFC2D)....7
1.2.2 Bonded Particle Model (BPM)....9
1.2.2.1 Grain Behavior....10
1.2.2.2 Cement Behavior/Parallel Bond....13
1.2.2.3 Microproperty Characterization....15
1.2.2.4 Particle Size of the BPM....18
1.2.2.5 Application of BPM in Ceramics....21
1.3 Objectives of this work....22
2. Discrete Element Modeling of SiC Ceramic and Graphite....23
2.1 Particle Assembly Preparation....23
2.1.1 Initial Particle Compaction....25
2.1.2 Installation of Specific Isotropic Stress....26
2.1.3 Elimination of the "Floating" Particles....28
2.1.4 Installation of the Parallel Bond....29
2.2 Calibration....30
2.2.1 Material Tests/Virtual Tests....31
2.2.1.1 Unconfined Compression....32
2.2.1.2 Brazilian Test....32
2.2.1.3 Three-Point Bending Test....33
2.2.1.4 Single-Edge-Notched Bending Test....33

2.2.2 Macro- and Micro-Properties of the BPM.....34
2.3 BPM of SiC-C Laminates.....37
2.3.1 BPM with Graphite Layer.....37
2.3.2 BPM without Graphite Layer.....38
2.4 Load and Boundary Conditions.....39
2.4.1 Loading.....39
2.4.2 Boundary Conditions.....40
2.4.3 Time Step.....40
3. Fracture Modeling of SiC Bulk Material and SiC-C Laminates.....41
3.1 Fracture Modeling of SiC Bulk Material.....41
3.2 Fracture Modeling of SiC-C Laminates.....42
3.2.1 BPM Including the Thickness of Graphite Interlayer.....42
3.2.1.1 Interlayer Thickness of 30 μm.....42
3.2.1.2 Interlayer Thickness of 10 μm.....44
3.2.2 BPM Excluding the Thickness of Graphite Interlayer.....45
3.2.2.1 One Interface.....46
3.2.2.2 Two Interfaces.....48
3.2.2.3 Three Interfaces.....51
3.2.2.4 Four Interfaces.....53
3.2.2.5 Five Interfaces.....56
3.2.2.6 Six Interfaces.....59
3.2.2.7 Seven Interfaces.....62
3.2.2.8 Eight Interfaces.....65
3.2.2.9 Nine Interfaces.....70
3.3 R-Curve Behavior of SiC-C Laminates.....74
3.4 Bending Strength of SiC-C Laminates.....76
3.5 Fracture Energy of SiC-C Laminates.....78
4. Discussion.....81

4.1 About the Discrete Element Method.....81
4.2 About the Fracture Modeling of SiC-C Laminate.....84
4.2.1 Qualitative Comparison.....86
4.2.2 Quantitative Comparison.....89
4.2.3 Fracture Energy of SiC-C Laminates.....91
4.2.4 Parameters of BPM for SiC-C Laminates.....92
4.3 Limitations.....93
5. Conclusions and Future Work.....96
Reference.....98
Curriculum Vitae.....104
Abstract.....105
Zusammenfassung.....106

1. Introduction and Objective

1.1 Ceramic laminates with weak interfaces

Ceramics have some desirable features which make them very useful for many specific applications. However, ceramics have a large fraction of ionic or covalent bonds that resulted their brittleness and the large scatter in the mechanical properties [1, 2]. The brittleness is the major problem of ceramics with their reliable use in engineering [3]. In 1964, Cook & Gordon proposed one way to overcome this problem by introducing weak interfaces to deflect a growing crack [4]. The presence of weak interfaces transverse to a crack growing in a brittle material can cause the deflection of the crack with a consequent increase in the resistance to crack growth [5]. The utilization of crack deflection as toughening has direct analogues in some biological structures [6].

Natural materials like bone, wood and nacre have very complex hierarchical designs in their highly sophisticated structure, revealing properties that are superior to what could be expected from a simple mixture of their components [7, 8]. This is the long developed ability of nature that combines brittle minerals and organic molecules into composites with exceptional fracture resistance and structural capabilities [8-10]. A prime example is nacre, which has the unique micro-nanoscale masonry architecture (Figure 1), composed of alternating layers of hard aragonite sheets separated by thin layers of organic biopolymer. The toughness of nacre is believed to originate from this "brick-and-mortar" structure [12-16]. The biological structure of nacre has long inspired researchers to reproduce nature's achievements and synthesize structural materials using the similar design [17]. Natural composites achieve strength and toughness through this complex hierarchical structure are extremely difficult to replicate synthetically. However some practical advances have been achieved. Clegg *et. al.* [3] coated thin sheets made from silicon carbide powder with graphite to give the weak interface and then pressed together and sintered without pressure. Relative to the monolithic material, the apparent fracture toughness for cracks propagating normal to the weak interfaces is increased more than fourfold, and the work required to break the samples increased substantially more than a hundredfold. Munch *et. al.* [18] synthesized composites with alumina and polymethyl methacrylate by freeze casting, the specific strength and toughness properties of these freeze-cast composites match with those of engineering aluminum alloys. Several attempts to

produce synthetically laminated organo-ceramic nanocomposites with nacre-like structure under ambient or biomineralization-like mild conditions have also been reported [9, 19, 20]. Zlotnikov *et. al*. [17] successfully synthesized bioinspired zirconia/organic nanolaminates with controlled layer thickness by PVD sputtering of ZrO_2 on organic nanofilms deposited by a polyelectrolyte based layer-by-layer technique.

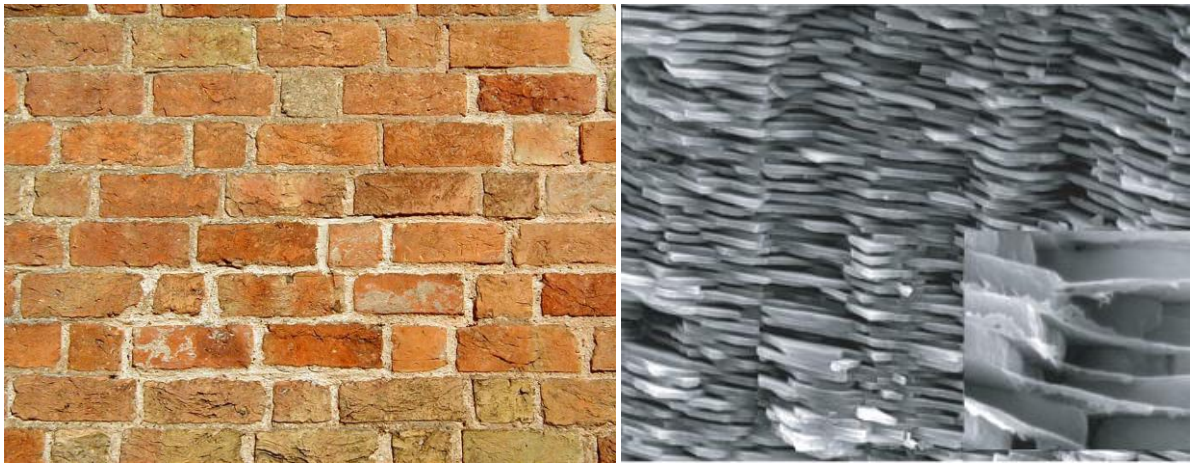


Figure 1: Masonry architecture (left) and the structure of nacre (right) [11].

Unlike monolithic ceramics, the ceramic laminates will exhibit the so-called "graceful failure" (Figure 2) when tested in bending [21]. The drop-off in load beyond the maximum is non-precipitous rather than catastrophic fall. As the load continues, a series of smaller load-displacement peaks will arise until the laminate eventually fails. Deflection of the crack at the first interface it impinges has been observed in-situ in the fracture process of the notched bend specimens. Then a de-lamination crack grows along the graphite layer. This process is illustrated in Figure 3. Finally, fracture of the layer adjacent to the de-lamination crack occurs, and the crack traverses the SiC lamina only to be deflected once more at the next graphite layer. In Figure 2, this corresponds to the point of the maximum load. The crack traverses the SiC layer initiated at a point well away from the tip of the original de-lamination crack. This led Clegg & Seddon to suggest that the second crack grows from an existing defect within the SiC lamina [22], which in turn implies that the strength of the composite is determined by the strength of the individual SiC layers and that is a possible strategy for enhancing the mechanical behavior of the laminate. Subsequently, this idea has been confirmed by Clegg who introduced artificial flaws of different sizes into the SiC

layers, and the apparent fracture toughness showed linear dependence with the strength of the unnotched bar [23].

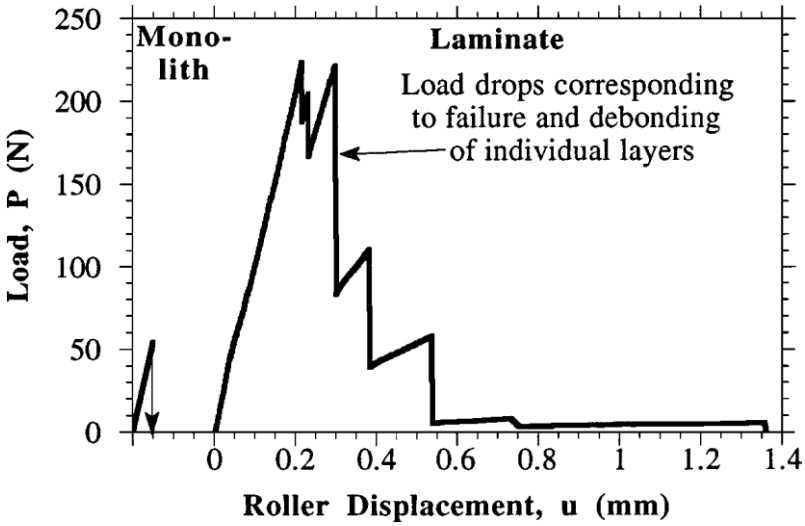


Figure 2: Load-displacement diagram (graceful failure) of notched SiC/graphite laminate tested under three-points bending, behavior of monolithic SiC is included for comparison (from W.J. Clegg in [21]).

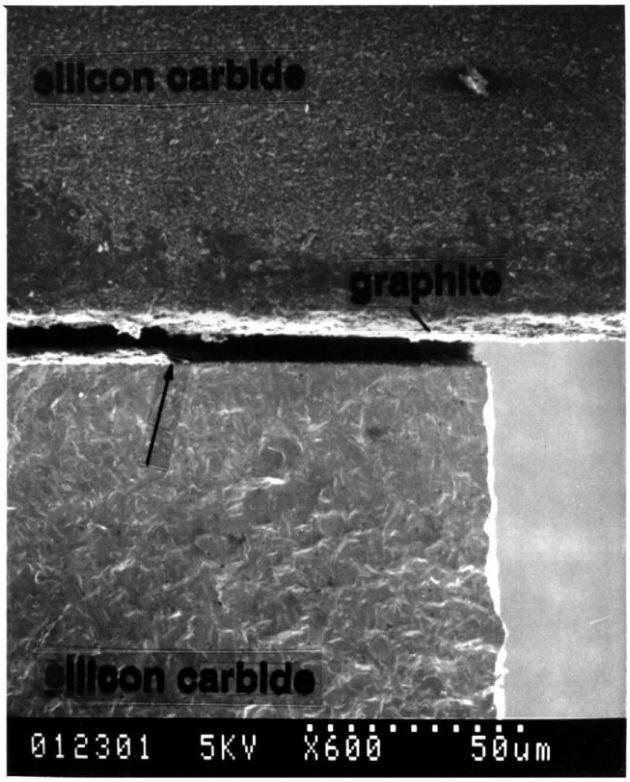


Figure 3: SEM micrograph showing a deflected crack at the first SiC/graphite interface it meets in a notched sample tested in three-point bend, it grows along the graphite layer after deflection (from W.J. Clegg in [21]).

Fibrous monolith system is another class of ceramic composites that exhibits graceful deformation and fracture characteristics. The cell-boundary material has been deliberately chosen so as to promote de-lamination in the fibrous monolith system [21]. Halloran and co-workers proposed some promising fibrous monolith systems as like SiC/graphite [24, 25], SiC/BN [25-27] and Si_3N_4/BN [27]. These systems exhibit a peak flexural stress followed by a series of load drops associated with shear de-lamination along the cell boundaries, where failure is non-catastrophic with the specimen retaining load-bearing capacity after the onset of cracking. This is in a manner directly analogous to the behavior of the SiC/graphite laminate studied by Clegg and co-workers [3, 21-23].

1.1.1 Mechanical Modeling of Ceramic Laminates

Modeling of the mechanical behavior of laminar composites with weak interlayers has been conducted by Phillipps *et. al.* [28] and Folsom *et. al.* [29, 30]. These two models are different; the former is more of a fracture mechanics approach and considers the competition between the growths of de-lamination cracks versus the propagation of transversal cracks. However, the latter is based on continuum elasticity and assumes that the toughness of the interfaces is essentially zero. Both models give insight into the behavior of this class of laminar composites.

The model by Phillips *et. al.* [28] considered a situation where de-lamination and layer cracking occur sequentially. The elastic strain energy released on fracture of the preceding layer determined the extent of growth of the interfacial crack. When the tensile stress exceeded the strength, fracture of the layers was considered to occur. At every point, the compliance was taken to be that of the uncracked portions of the body. In aim of tailoring the laminate geometry/composition to achieve the maximum work of fracture, the major predictions of the model were as follows: (a) increase the strength of the constituent layers, (b) increase the interfacial toughness so that more energy can be dissipated during de-lamination (however, the interfaces must still be sufficiently weak to promote crack deflection), and (c) decrease the Young's modulus of the layers.

Based on Euler-Bernoulli beam theory, Folsom *et. al.* [29] considered the redistribution of stress and strain in a multilayer composite as successive rupture of layers. They made two important assumptions of the model: (a) a layer is considered

to be removed from the system once it is cracked, since it does not support any load, and (b) the layers are stronger in compression than in tension. This work addressed why layered composites exhibit markedly different behavior depending on whether they are tested in tension or bending. The Weibull modulus of the strength distribution of the individual layers turns out to be an important consideration in this respect. As the Weibull modulus approaches infinity (each layer of the layered composite has the same deterministic strength), the model predicts that the strength of the composite in bending is equal to the tensile strength. This is due to the fact that in flexure the maximum tensile stress appears on the outermost layer, and the first load drop occurs when that tensile stress becomes equal to the layer strength. Nevertheless, the flexural strain to failure (as measured by the load point displacement) is significantly greater than the tensile strain to failure because of the increasing compliance of the specimen as successive layers fracture. If the layers are assumed to have a statistical distribution of strengths, then fracture will no longer begin with the outermost layer, i.e. no sequential fracture will occur. When this situation is compared with the tension case, the model predicts that the flexural strength is consistently higher than the tensile strength. Good agreement was obtained as the results of the model were compared with experiment in a companion paper [30].

1.1.2 Crack Deflection Criteria

Up to now, it has been clarified that the presence of weak interfaces in ceramic laminates causes crack deflection, which act as the principal toughening mechanism in laminar composites. Issues regarding the criterion of crack deflection at weak interfaces need to be discussed next. Stress-based criteria, in which de-bonding of the interface depends on the ratio of the interfacial strength to that of the matrix phase, have been derived by Cook & Gordon [4] and Gupta *et. al.* [31]. Cook & Gordon inferred that the interface will de-bond ahead of the main crack to allow deflecting when the interface with a theoretical tensile strength of less than 1/5 that of the matrix [4]. However, Gupta *et. al.* predicted that for crack deflection the interface must have a strength less than about 0.35 that of the matrix where there was no elastic mismatch [31]. Energy-based approaches, where the tendency for de-bonding is related to the relative fracture energies of the interface and the reinforcement, have also been developed [32-34]; among these, the work of He & Hutchinson [34] has

gained widespread acceptance. It was considered by those workers that there was an elastic mismatch across the interface, *i.e.* a primary crack with the crack tip situated at the interface between two dissimilar materials. They compared the energy release rates for a crack crossing the interface (penetration) and a crack traveling along the interface (deflection). For two materials with the same elastic modulus (no elastic mismatch), a critical ratio about 0.25 was predicted for the energy release rate for a deflected crack to that of a penetrating crack. Furthermore, the tendency for deflection increases remarkably when the crack is approaching a stiffer material (from compliant to stiff). Conversely, if the crack is approaching a more compliant material, it will tend to penetrate through the interface. The above mentioned fracture mechanics analyses have all assumed that a stationary transversal crack exists at the interface and the crack deflection is assumed to occur when the applied forces are such that the interfacial crack can grow but not the transversal crack. However, this is not the real situation, the through thickness crack often moves in an unstable way, and where the continued growth of this crack will result other energy changes. In this regard, the intrinsic flaw distribution across from the through thickness crack and along the interface will clearly have influence on the crack path. Moreover, there is also possibility that the sequence of events in the crack deflection process may differ from that modeled by He & Hutchinson [34]. As in the experiments on polymethylmethacrylate (PMMA) laminates, the crack deflection has been observed to take place by the growth of an interfacial de-bond (de-lamination) ahead of the through thickness crack [35]. This led Lee & Clegg [35] to suggest that a critical condition for deflection is the onset of growth of any pre-existing interfacial flaws. Subsequently, they derived a crack deflection criterion based on the inability of the interfacial crack to kink out of the interface.

1.2 Discrete Element Method (DEM)

Discrete element method (DEM), also called distinct element method is a numerical method for computing the motion and interaction of a large assembly of particles (disks/spheres) in micro-scale size and above. Particles can deform and displace independently from one another and interact through contacts or interfaces between them. The motion and interaction of a system of particles is simulated by a time-marching scheme that integrates the equations of motion by a central, finite-difference method that ensures excellent accuracy and freedom from drift. In 1971,

the DEM was first proposed by Cundall [36]. In 1979, Cundall & Strack [37] initiated the development of DEM in geomechanical fields in the context of studying mechanics of rock and granular materials. The original application of this method was as a tool to study the behavior of granular material. Models containing several hundred particles were tested numerically for some representative elements to understand element behaviors. And then a continuum method was used to solve real problems that involve sophisticated deformation patterns (with the element behaviors derived from the particle model). Later on, two main factors have brought about a change in this approach [38]. First, the derivation of the general constitutive laws from test results on particle assemblies is very difficult. Second, as personal computers have tremendously increased in their power, it is possible to model entire problem with particles (the constitutive behavior is automatically built into the model). In 1981, Cundall (as one the five cofounders) founded *Itasca consulting group*, which provide services in rock mechanics, numerical modeling of geotechnical environments, and underground space use. Today DEM is becoming widely accepted as an effective method of addressing engineering problems in granular and discontinuous materials, especially in granular flows, powder mechanics, and rock mechanics [38, 39].

1.2.1 Particle Flow Code in 2 Dimensions (PFC2D)

The first commercial DEM code PFC2D from *Itasca* was released in 1994. It was designed as an efficient tool to model complicated problems in solid mechanics and granular flow. PFC2D is a discontinuum code used in analysis, testing, and research in any field where the interaction of many discrete objects exhibiting large-strain and/or fracturing is required. Since PFC2D is not designed to examine a specific type of problem, its range extends to any analysis that examines the dynamic behavior of a particulate system [38].

Materials can be modeled in PFC2D as either bonded (cemented) or unbonded (granular) assemblies of particles. Though the code uses circular particles by default, sophisticated particle shape can be defined in a PFC2D model through use of the built-in clump logic. An explicit solution scheme that gives stable solutions to unstable processes has been adopted by PFC2D. Nonlinear behavior and localization can be described with accuracy, which cannot be matched by typical finite element programs. This makes PFC2D the only commercially available code of its kind [38]. Figure 4

shows the explicit calculation cycle that solves two sets of equations (motion and constitutive). In both sets, variables on the right-hand-side of expressions are all known, and can be regarded as fixed during the step. Therefore, nonlinear contact relations (e.g. as brittle bond rupture) are used without difficulty, as only local conditions are relevant during the time-step. Moreover, no iterations are necessary to follow nonlinear laws and no matrices are formed.

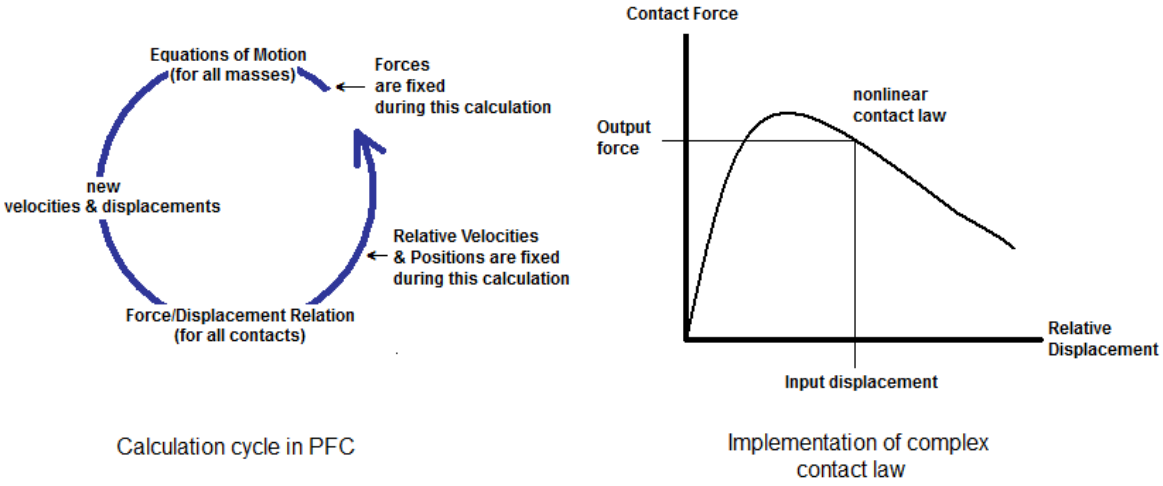


Figure 4: PFC2D computation cycle (left) and implementation of nonlinear contact law in PFC2D (right).

In parallel with the mechanical calculations, the code has implemented with advanced contact detection algorithms, which continuously detect new contacts between particles and delete contacts when particles separate. The algorithms are invisible to the user of PFC, and they are optimized to consume very little calculation time. For instance, the detection logic is only triggered at a local level when movement sufficient to allow potential new contacts has accumulated. Overall, the searching and detection scheme executes in a time that is linearly dependent on the number of particles. The efficient contact detection scheme and the explicit solution method ensure that a wide variety of simulations - from rapid flow to brittle fracture of a stiff solid - are modeled accurately and rapidly. In addition, all the equations used in PFC2D are documented. The user has access to almost all internal variables via the powerful built-in programming language FISH [39].

1.2.2 Bonded Particle Model (BPM)

The Bonded Particle Model (BPM) is first proposed by Potyondy & Cundall to study mechanical behavior of rock in 2004 [40]. In the 2D model, the rock is represented by a dense packing of non-uniform-sized circular particles that are bonded together at their contact points. Many features of rock behavior that correspond very well with those of real rock have been reproduced, including elasticity, fracturing, acoustic emission, hysteresis, damage accumulation caused material anisotropy, dilation, post-peak softening and strength increase with confinement.

Unlike the common definition of the term "particle" in the field of mechanics, where the "particle" is treated as a body of negligible size and occupies only a single point in space; in the present context, the term “particle” denotes a body that occupies a finite amount of space. At the contacts, where the rigid particles only interact, possess finite normal and shear stiffnesses. The mechanical behavior of the BPM system is described by the movement of each particle together with the force and moment acting at each contact. The fundamental relation between particle motion and the resultant forces and moments causing that motion is provided by the Newton's laws of motion [38].

The following are the inherent assumptions of the BPM in PFC2D [40]:

1. The particles are rigid circular bodies with finite masses.
2. The particles move independently from each other and can both translate and rotate.
3. The particles interact only at contacts; since the particles are circular, a contact is involved with exactly two particles.
4. Overlaps are allowed between the particles, however, overlaps are small compare to particle size and contacts occur only over a small region (at a point).
5. Bonds with finite stiffness can present at contacts, bonds carry load and therefore can break; overlap is not required for the particles at a bonded contact.

6. Generalized force–displacement laws are applied at each contact to relate the relative particle motion to the force and moment at that contact.

It is reasonable to assume that the particles are rigid, since the movements along interfaces account for most of the deformation in a material. For a granular assembly such like sand or a packed-particle assembly, the deformation of the assembly can be well described by this assumption, since the deformation is primarily resulted from the sliding and rotation of the particles as rigid bodies and the opening and interlocking at interfaces, rather than from individual particle deformation. The bonds presented between the particles in the assembly correspond with the real cement presented between the grains of a sedimentary rock, such as sandstone, or the notional cement between the grains of a crystalline rock, such as granite. Therefore, the deformation of a bonded-particle assembly should be similar as a rock, and both systems should exhibit similar damage-formation processes under increasing load as the bonds are broken in a progressive pattern and both systems gradually evolve toward a granular state. Moreover, the BPM can also accommodate other microstructural features as grain crushing and material inhomogeneity at certain scale (larger than the grain size) when individual grains or other microstructural features are represented as clusters of bonded particles [41-43].

The rock is mimicked in the BPM as a collection of grains joined by cement. In PFC2D, each grain is considered as a particle and each cement entity as a parallel bond. Two contact behaviors are presented in the model, i.e. the grain behavior and the cement behavior. The total force and moment acting at each cemented contact is comprised of a force, F_i, arising from particle–particle overlap, denoted in Figure 5 as the grain behavior, and a force and moment, $\overline{F_i}$ and $\overline{M_i}$, carried by the parallel bond and denoted as the cement behavior. These quantities contribute to the resultant force and moment acting on the two contacted particles. In the following, the force–displacement law for both the grain behavior and the cement behavior will be described. Note that if a parallel bond is not present at a contact, then only the grain-based portion of the force–displacement behavior occurs [40].

1.2.2.1 Grain Behavior

Six parameters are necessary for describing the grain-based portion of the force–displacement behavior at each contact (see Fig. 5). These are: the normal and shear

stiffnesses, k_n and k_s, and the friction coefficient, μ, for the two contacting particles, which are assumed to be disks with unit thickness in PFC2D. If overlap between two particles exists, a contact is formed at the center of the overlap region along the line joining the particle centers ($x_i^{(c)}$ in Fig. 5), and two linear springs acting in series are inserted (with the stiffness derived from the particle stiffnesses) along with a slider in the shear direction [40].

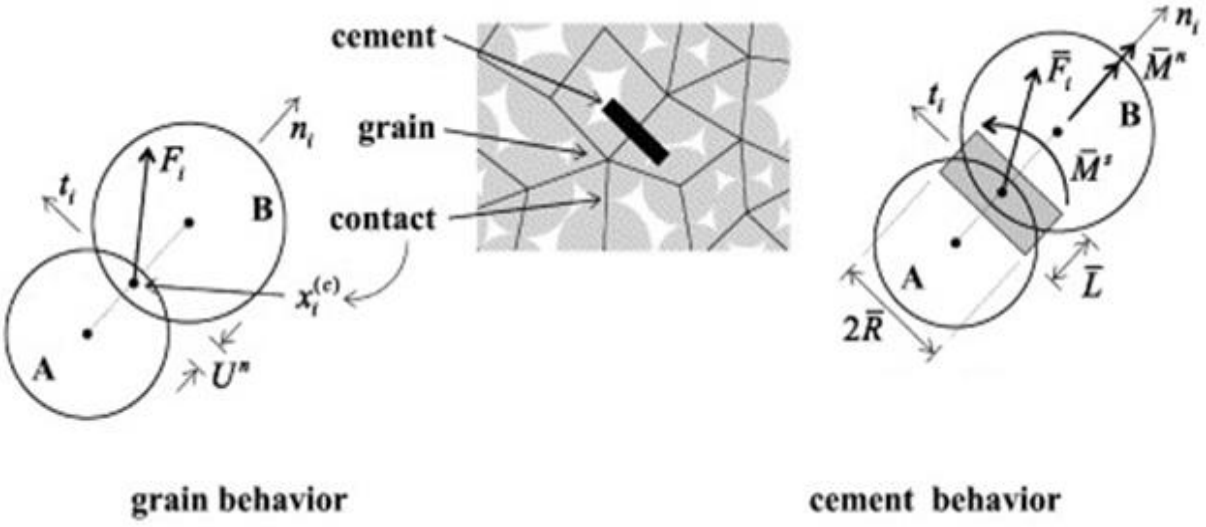


Figure 5: Force-displacement behavior of grain-cement system [40].

F_i is the contact force vector and represents the action of particle A on particle B, this vector can be decomposed with respect to the contact plane into normal and shear components as

$$F_i = F^n n_i + F^s t_i \tag{1}$$

where F^n and F^s denote the normal and shear force components, respectively, and n_i and t_i are the unit vectors that define the contact plane. The normal force then can be written as

$$F^n = K^n U^n \tag{2}$$

where U^n is the overlap and K^n is the contact normal stiffness (two linear springs in series) given by

$$K^n = \frac{k_n^{(A)} k_n^{(B)}}{k_n^{(A)} + k_n^{(B)}} \tag{3}$$

with $k_n^{(A)}$ and $k_n^{(B)}$ being the normal stiffnesses of the two particles A and B [38, 40].

The shear force is computed in an incremental fashion. When the contact is formed, F^s is initialized to zero. Each subsequent relative shear–displacement increment, ΔU^s, produces an increment of elastic shear force, ΔF^s, that is added to F^s (after F^s has been rotated to account for motion of the contact plane). Therefore, the increment of elastic shear force is given by

$$\Delta F^s = -k^s \Delta U^s \tag{4}$$

where k^s is the contact shear stiffness given by

$$k^s = \frac{k_s^{(A)} k_s^{(B)}}{k_s^{(A)} + k_s^{(B)}} \tag{5}$$

with $k_s^{(A)}$ and $k_s^{(B)}$ being the shear stiffnesses of particle A and B. The relative displacement increment during the time step Δt is given by $\Delta U_i = V_i \Delta t$, where V_i is the contact velocity

$$V_i = \left(\dot{x}_i^{(c)}\right)_B - \left(\dot{x}_i^{(c)}\right)_A = \left(\dot{x}_i^{(B)} + e_{ijk}\omega_j^{(B)}\left(x_k^{(c)} - x_k^{(B)}\right)\right) - \left(\dot{x}_i^{(A)} + e_{ijk}\omega_j^{(A)}\left(x_k^{(c)} - x_k^{(A)}\right)\right) \tag{6}$$

$\dot{x}_i$ and ω_j stand for translational and rotational velocities of the particle, respectively, and e_{ijk} is the permutation symbol. The relative shear–displacement increment vector is

$$\Delta U_i^s = V_i^s \Delta t = \left(V_i - V_i^n\right)\Delta t = \left(V_i - V_j n_j n_i\right)\Delta t \tag{7}$$

When $U^n \le 0$ (a gap exists), both normal and shear forces are set to zero; otherwise, slip is accommodated by computing the contact friction coefficient

$$\mu = \min\left(\mu^{(A)}, \mu^{(B)}\right) \tag{8}$$

with $\mu^{(A)}$ and $\mu^{(B)}$ being the particle friction coefficients, and setting $F^s = \mu F^n$ if $F^s > \mu F^n$ [40].

1.2.2.2 Cement Behavior/Parallel Bond

The cement-based portion of the force-displacement behavior at each cemented contact is described as a parallel bond, which can be envisioned as a set of elastic springs uniformly distributed over a rectangular cross-section and centered at the contact point [40]. These springs behave similar to that of a beam whose length, $\bar{L}$ in Fig. 5, approaches zero. A parallel bond approximates the mechanical and physical behavior of a cement-like substance lying between and joining the two bonded particles. Moreover, parallel bonds establish an elastic interaction between these particles that acts in parallel with the grain-based portion of the force-displacement behavior; thus, the existence of a parallel bond does not prevent slip, *i.e.* if two particles overlap, the point-contact springs which described above can be in effect simultaneously. Unlike grains can only transmit force, parallel bonds can transmit both force and moment between particles. To define a parallel bond, five parameters are needed (see Fig. 6): normal and shear stiffnesses per unit area, $\bar{k}^n$ and $\bar{k}^s$; tensile and shear strengths, $\bar{\sigma}_c$ and $\bar{\tau}_c$; and bond-radius multiplier, $\bar{\lambda}$, this defines the parallel-bond radius by

$$\bar{R} = \bar{\lambda} \min\left(R^{(A)}, R^{(B)}\right) \tag{9}$$

where $R^{(A)}$ and $R^{(B)}$ being the particle radii.

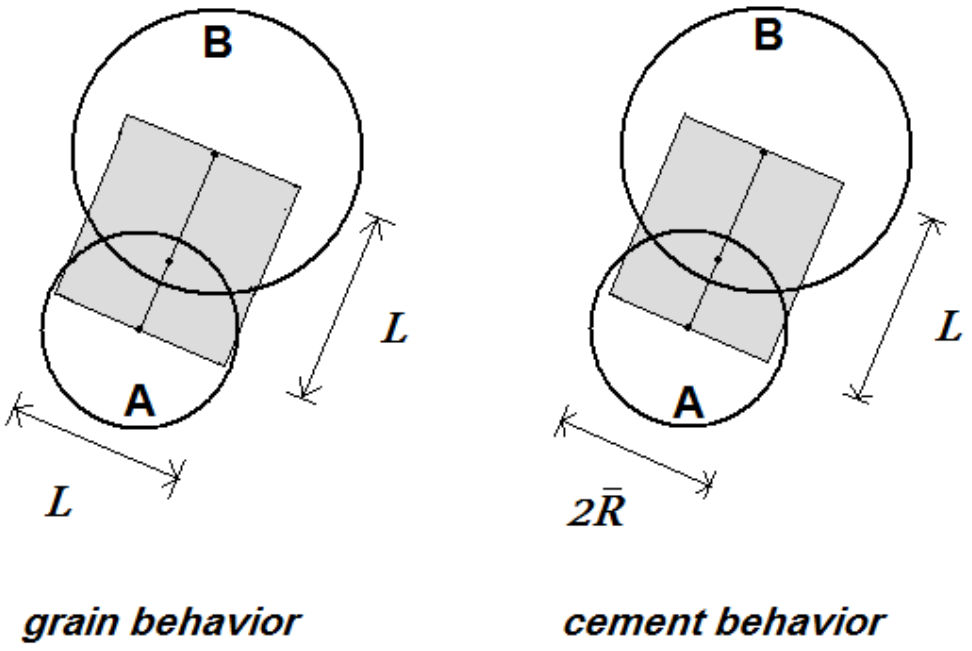


Figure 6: Equivalent continuum material of grain (left) and cement system (right) [40].

The action of the bond on particle A (same as on particle B) are the total force $\overline{F}_i$ and moment $\overline{M}_i$, which carried by the parallel bond. Similar to F_i, the force and moment vectors can be decomposed into normal and shear components with respect to the contact plane as

$$\overline{F}_i = \overline{F}^n n_i + \overline{F}^s t_i \tag{10a}$$

and

$$\overline{M}_i = \overline{M}^n n_i + \overline{M}^s t_i \tag{10b}$$

where $\overline{F}^n$, $\overline{F}^s$ and $\overline{M}^n$, $\overline{M}^s$ stand for the axial- and shear-directed forces and moments, respectively, and n_i and t_i are the unit vectors that define the contact plane. When a parallel bond is formed, $\overline{F}_i$ and $\overline{M}_i$ are initialized to zero. Each subsequent relative displacement- and rotation increment (ΔU^n, ΔU^s, $\Delta\theta^n$, $\Delta\theta^s$ with $\Delta\theta_i = \left(\omega_i^{(B)} - \omega_i^{(A)}\right)\Delta t$) produces an increment of elastic force and moment that is added to the current values (after the shear-component vectors have been rotated to account for motion of the contact plane). The increments of elastic force and moment are given by

$$\Delta\overline{F}^n = \bar{k}^n A \Delta U^n \tag{11a}$$

$$\Delta\overline{F}^s = -\bar{k}^s A \Delta U^s \tag{11b}$$

$$\Delta\overline{M}^n = -\bar{k}^s J \Delta\theta^n \tag{11c}$$

$$\Delta\overline{M}^s = -\bar{k}^n I \Delta\theta^s \tag{11d}$$

where A and I are the area and moment of inertia of the parallel bond cross-section, respectively. J is the polar moment of inertia and is not available for PFC2D cases. These quantities are given by

$$A = 2\overline{R}t \tag{12a}$$

$$I = \frac{2}{3}\overline{R}^3 t \tag{12b}$$

where $t = 1$ in PFC2D [38, 40].

The maximum tensile and shear stresses acting on the parallel-bond periphery are calculated from beam theory to be

$$\bar{\sigma}^{\max} = \frac{-\bar{F}^{n}}{A} + \frac{\left|\bar{M}^{s}\right|\bar{R}}{I} \tag{13a}$$

$$\bar{\tau}^{\max} = \frac{\left|\bar{F}^{s}\right|}{A} + \frac{\left|\bar{M}^{n}\right|\bar{R}}{J} \tag{13b}$$

Note that, for the PFC2D model, the twisting moment, $\bar{M}^{n} = 0$, and the bending moment, $\bar{M}^{s}$, acts in the out-of-plane direction. When $\bar{\sigma}^{\max} \geq \bar{\sigma}_{c}$ or $\bar{\tau}^{\max} \geq \bar{\tau}_{c}$, then the parallel bond will break, and will be removed from the model along with its accompanying force, moment and stiffnesses [38, 40].

1.2.2.3 Microproperty Characterization

Unlike in the continuum modeling, where the input properties such as elastic modulus and strength can be derived directly from measurements performed on specimens. In PFC2D, or generally in DEM code, the input properties of the microscopic constituents, from which the macro-scale material behavior has been synthesized, are usually unknown. Therefore, a calibration process, in which the responses of the synthetic material are compared directly with the relevant measured responses of the intended physical material, is conducted. A flow chart of this calibration process is illustrated in Figure 7. In chapter 2, this calibration process will be described for sintered ceramics in detail after the synthesis of the particle-packing assembly.

In the synthesized particle assembly (here means the BPM for a synthesized material), the particle diameters satisfy a uniform particle-size distribution bounded by $D_{\min}$ and $D_{\max}$, a dense packing is obtained using the material-genesis procedure (details in Chapter 2). The packing fabric or the connectivity of the bonded assembly are controlled by the $D_{\max}/D_{\min}$ ratio. For a fixed ratio, varying $D_{\min}$ changes the absolute particle size but does not affect the packing fabric. Such a microproperty characterization separates the effects of packing fabric and particle size on material behavior and clearly identifies $D_{\min}$ as the controlling length scale of the synthesized material. In general, the BPM is characterized by the grain density, grain shape, grain size distribution, grain packing and grain-cement microproperties. The grain means

here particle or cluster. Each of these items influences the model behavior. A list of nomenclature for those microproperties which are mentioned above is summarized in Table 4.

The grain density, ρ, does not affect the quasi-static behavior but is included for completeness. The final item that characterizes the BPM is the grain-cement microproperties [38-40]:

$$\{E_c, (k_n/k_s), \mu\} \tag{14a}$$

for grain microproperties, and

$$\{\bar{\lambda}, \bar{E}_c, (\bar{k}^n/\bar{k}^s), \bar{\sigma}_c, \bar{\tau}_c\} \tag{14b}$$

for cement microproperties, where E_c and $\bar{E}_c$ are the Young's moduli of the grains and cement, respectively; (k_n/k_s) and $(\bar{k}^n/\bar{k}^s)$ are the ratios of normal to shear stiffness of the grains and cement, respectively; $\bar{\lambda}$ is the radius multiplier used to set the parallel-bond radii via Eq. (9); μ is the grain friction coefficient; and $\bar{\sigma}_c$ and $\bar{\tau}_c$ are the tensile and shear strengths of the cement, respectively. E_c and $\bar{E}_c$ are different from the ensemble Young's modulus, which is usually smaller than the E_c and $\bar{E}_c$. In the analysis below, the grain and cement moduli are related to the corresponding normal stiffnesses such that the particle and parallel-bond stiffnesses are assigned as

$$k_n = 2tE_c \tag{15a}$$

$$k_s = \frac{k_n}{(k_n/k_s)} \tag{15b}$$

$$\bar{k}^n = \frac{\bar{E}_c}{R^{(A)} + R^{(B)}} \tag{15c}$$

$$\bar{k}^s = \frac{\bar{k}^n}{(\bar{k}^n/\bar{k}^s)} \tag{15d}$$

where R is particle radius and $t = 1$ for PFC2D. The usefulness of these modulus–stiffness scaling relations is confirmed by the self-test where it is shown that the

macroscopic elastic constants are independent of particle size for the PFC2D material and exhibit only a minor size effect for the PFC3D material [40].

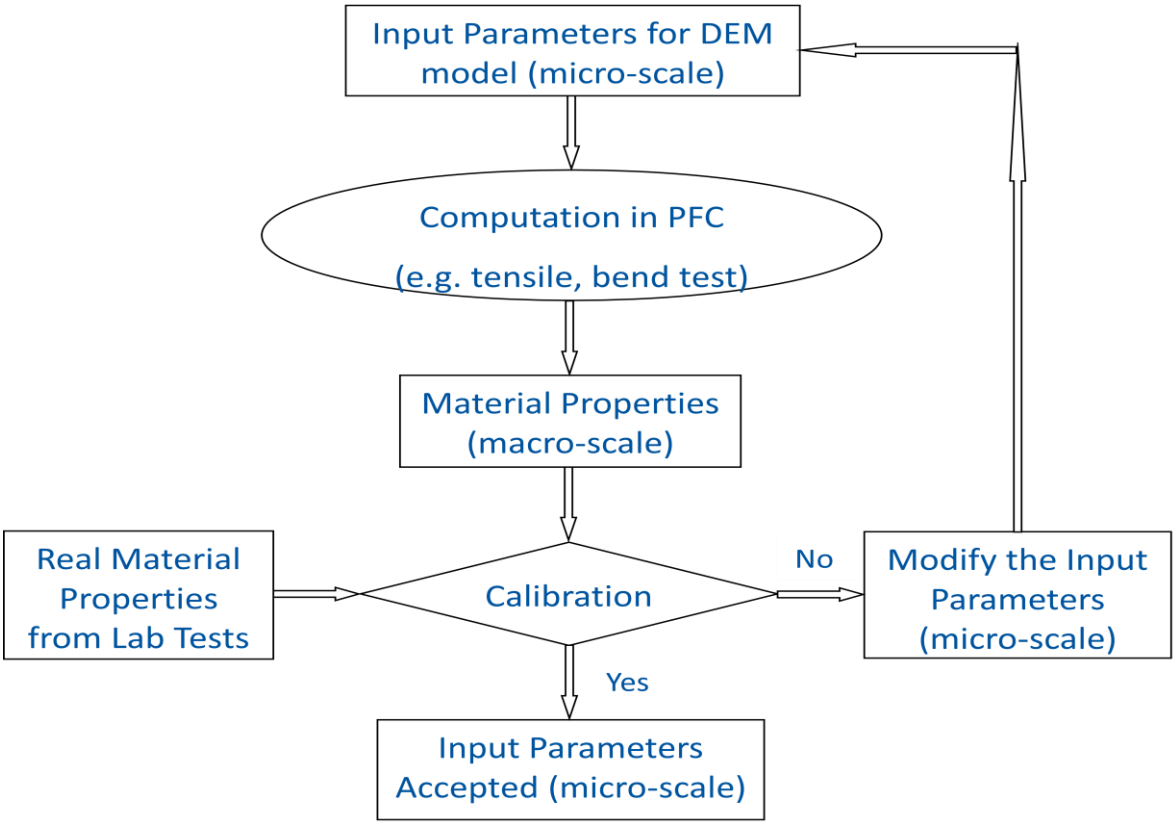


Figure 7: Calibration process.

The deformability of an isotropic linear elastic material is described by two elastic constants. These quantities are emergent properties of the BPM and cannot be specified directly. It is possible, however, to relate the grain and cement moduli, E_c and $\overline{E}_c$, respectively, to the normal stiffnesses by envisioning the material at each contact as an elastic beam with its ends at the particle centers, as shown in Fig. 6. According to McGuire and Gallagher [44], the normal and shear stiffnesses for the beam can be expressed as $k^n = AE/L$ and $k^s = 12IE/L^3$ where A, E, L and I are the cross-sectional area, modulus, length and moment of inertia, respectively, of the beam.

For the grain-based behavior:

$$k^n = \frac{k_n^{(A)} k_n^{(B)}}{k_n^{(A)} + k_n^{(B)}} = \frac{AE_c}{L} = \frac{LtE_c}{L} = E_c t \tag{16}$$

with $A = Lt$, and

$$k^s = \frac{k_s^{(A)} k_s^{(B)}}{k_s^{(A)} + k_s^{(B)}} = \frac{12IE_c}{L^3} = \frac{12E_c}{L^3} \cdot \frac{tL^3}{12} = E_c t \tag{17}$$

with $I = tL^3/12$, by assuming $k_n = k_n^{(A)} = k_n^{(B)}$ in Eq. (16), then we obtain $k_n = 2E_c t$, where $t = 1$ in PFC2D [38, 39].

For the cement-based behavior:

$$\bar{k}^n = \frac{k^n}{A} = \frac{\bar{E}_c}{L} \tag{18}$$

with $L = \left(R^{(A)} + R^{(B)}\right)$ [38, 39].

Eq. (16) indicates that, in two dimensions, the modulus at the grain contact is directly proportional to particle stiffness and independent of particle radius; the cement modulus is, however, dependent on particle size. In order to achieve a constant cement modulus, parallel-bond stiffnesses must be scaled with the particle radii [38, 40]. This analysis does not yield a relation between Poisson's ratio and particle stiffness at the microlevel; however, a macroscopic Poisson's ratio will be observed, and its value will be affected by grain shape, grain packing and the ratios (k_n/k_s) and ($\bar{k}^n/\bar{k}^s$). For a fixed grain shape and packing, increasing these ratios increases the Poisson's ratio.

1.2.2.4 Particle Size of the BPM

The particle size of the BPM determines the resolution of the model, however, Potyondy *et. al.* [40] found out that this is not a free parameter; it is related directly to the material fracture toughness. Although the behavior of bond-breaks at the contacts of particles in the BPM might be conceptually different from the propagation of real cracks in a brittle continuum, a formal equivalence between the mechanisms

and parameters of the BPM and the concepts and equations of LEFM (short for Linear Elastic Fracture Mechanics) is still possible to establish.

For an infinitely wide plate of isotropic linear elastic material subjected to an external tensile stress σ_{ex} which acting normal to the crack as shown in Figure 8. The plate is considered to be an assembly of cubically packed particles with uniformed particle size (R) and unit-thickness ($t=1$). A crack with half-width a is introduced into the plate as shown in Figure 8 by a line of unbonded contacts.

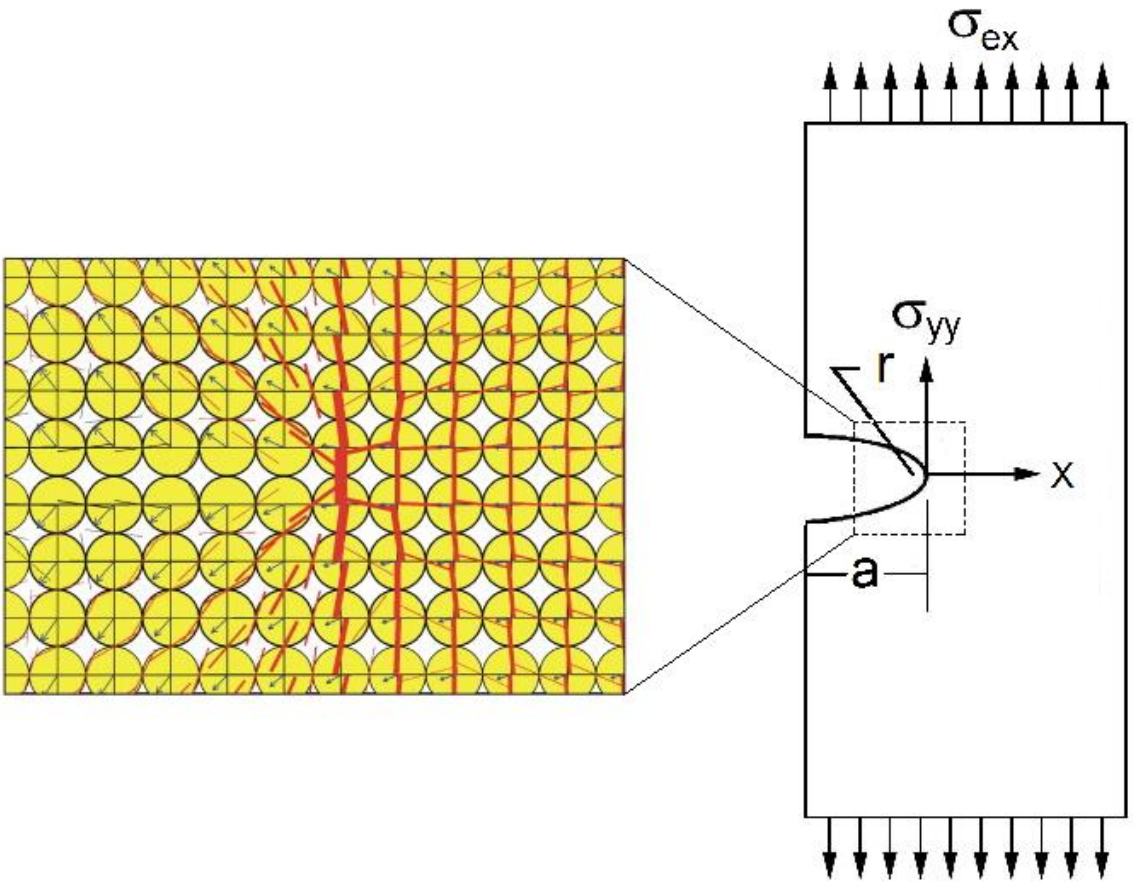


Figure 8: Magnified picture of the field near crack tip in which tensile contact forces are shown by red lines, displacements by black arrows and bonds by black lines (left); sketch for calculation of the Mode-I stress intensity factor of an infinitely wide plate in LEFM, half of the plate is shown here (right).

The induced stress σ_{yy} acting on the crack plane near the crack tip with radius r ($r << a$) is [45]

$$\sigma_{yy} = \sigma_{ex}\sqrt{\frac{a}{2x}} \tag{19}$$

where x is the distance from the crack tip. The force F_{yy} acting over a line segment equal to a particle diameter ($2R$) can be integrated between $x-R$ and $x+R$ with $x=(2m-1)R$ by

$$F_{yy}=\int_{x-R}^{x+R}\sigma_{yy}\cdot t\cdot dx=\sigma_{ex}\cdot t\cdot\sqrt{\frac{a}{2}}\cdot\int_{x-R}^{x+R}x^{-1/2}dx=2\sigma_{ex}t\sqrt{aR}\left(\sqrt{m}-\sqrt{m-1}\right) \tag{20}$$

where m ($m>0$) is an integer denoting the particle sequence number [40].

The maximum of F_{yy} will be achieved by substituting $m=1$ to Eq. (20) and obtain

$$F_{yy}^{\max}=2\sigma_{ex}t\sqrt{aR} \tag{21}$$

By noting that the stress intensity factor for mode-I is given by $K_I=\sigma_{ex}\sqrt{\pi a}$, the Eq. (21) can therefore be written as

$$F_{yy}^{\max}=2K_I t\sqrt{\frac{R}{\pi}} \tag{22}$$

If we denote the true tensile strength of the BPM by σ_t' and express the σ_t' as $\phi_n/(2Rt)$, where ϕ_n is the tensile strength for the bond (in force units) for the cubically packed BPM which is subjected to the external load as shown in Figure 8, then at the condition of incipient failure or beginning of crack extension, $F_{yy}^{\max}$ equals ϕ_n and K_I equals K_{Ic}, where K_{Ic} is the fracture toughness for mode-I. Under such a circumstance, we can obtain

$$K_{Ic}=\sigma_t'\sqrt{\pi R} \tag{23}$$

The fracture toughness is now related to the particle size which is one of the properties of BPM. It can be seen that the particle size cannot be chosen arbitrarily when certain fracture toughness is required to match the real material.

The abovementioned derivation of Eq. (23) is based on the assumption of a cubically packed BPM, in which the bonds at contacts are perfectly brittle. Potyondy and Cundall [40] have further performed a set of self-similar tests on the BPM of a plate which is loaded in the same way as shown in Figure 8. By varying the crack length a

and the width of the plate W while keeping the particle size R and the ratio a/W fixed, the results from the self-similar tests were close to those obtained for an arbitrarily packed BPM and led to the postulation of

$$K_{Ic} = \sigma_t' \sqrt{\pi \alpha R} \tag{24}$$

Eq. (24) is for the bonds with grain behavior (contact bond), where $\alpha \geq 1$ is a non-dimensional factor that increases with packing irregularity. For the bonds with cement behavior (parallel bond), another non-dimensional factor $\beta < 1$ is introduced to account for the weakening effect of the bending moment of parallel bond (*i.e.* the parallel bond is weaker than the contact bond for the same true tensile strength, as can be seen from Eq. (13)). Therefore Eq. (24) became

$$K_{Ic} = \beta \sigma_t' \sqrt{\pi \alpha R} \tag{25}$$

for the bonds with cement behavior.

The value of α and β can be obtained from the results of the self-similar tests, then a particular R value for the BPM of the synthesized material can be given by Eq. (25) with respect to the fracture toughness of the desired real material.

1.2.2.5 Application of BPM in Ceramics

Although the BPM was originally developed for rock and primarily used in geomechanics, successful applications in ceramics have also been reported. Tan *et. al.* [46, 47] employed DEM in their work to simulate the microscopic machining process of ceramics. The ceramic part was represented by a calibrated BPM, the dynamic process of initiation and propagation of the micro-cracks under various machining conditions was explicitly modeled. The numerical results agreed well with the experimental observations and theoretical predictions. Jiang *et. al.* [48, 49] studied the feasibility of pre-stressed machining on silicon carbide. They introduced "clusters" to BPM, both the DEM simulation and experimental investigation indicated that: by increasing the pre-stress, the radial cracks tend to be replaced by transverse cracks and cause the removal of material in the form of smaller fragments. Moreover, using pre-stressed machining can decrease the machining damage and improve the

surface quality. The DEM has been further proved feasible to simulate the machining process of ceramic materials.

1.3 Objectives of this work

We intend to numerically validate the process of the crack propagation in ceramic laminates, and reproduce the graceful fracture features. A better insight into the fracture behaviors as like the de-lamination and the crack deflection shall be achieved by means of the discrete element modeling. Suggestive optimization of the laminate construction shall be obtained by varying the parameters of the discrete element model of the laminate.

In the present study, calibration of BPMs for SiC ceramic and graphite will first be performed. Mechanical properties of BPMs will be quantitatively compared to the real data of materials. To establish the BPM of SiC-C laminate, two different structures of BPM for SiC-C laminate will be evaluated. The BPM of SiC-C laminate proposed in this study should be generalized for the layer-structured laminate. Parameters of the BPM should be variable in order to perform case studies for different ceramic laminates with different geometries and/or different constituent materials. With the model, fracture behavior and mechanical properties of the ceramic laminate should be predictable. Regarding the thickness of the weak interface (graphite interlayer) in the laminate, one structure including a thin weak interlayer (with thickness) and another structure excluding the thin weak interlayer (without thickness) will be compared and testified. A simpler and more explicit BPM will be chosen from those two different models to simulate the dynamic crack propagation processes in the SiC-C laminate. Fracture behaviors such as de-bonding, de-lamination and crack deflection in ceramic laminates toughened with weak interfaces will be reproduced qualitatively. Quantitative fracture behaviors, e.g. R-curve behavior will be analyzed from the results of the simulated models. At last, an investigation on the main parameter of the BPM for SiC-C laminate, i.e. the weak bond strength, will be performed.

2. Discrete Element Modeling of SiC Ceramic and Graphite

The synthesis of a particle assembly (*i.e.* BPM in PFC2D) for a particular ceramic material contains two procedures, which are the particle assembly preparation and calibration. The particle assembly preparation aims to create a dense packing of non-uniform-sized particles that are well joined at their contacts by parallel bonds. After the preparation of the particle assembly, specific particle and parallel bond properties will be determined at micro-scale by the calibration procedure and assigned to the particle assembly. In the calibration procedure [38, 39] virtual laboratory tests such as uniaxial compression, Brazilian test, and single-edge-notched bending test will be performed, whereas the real material properties at macro-scale will serve as references to calibrate the physical behaviors that the particle assembly exhibited in the virtual laboratory tests. A flow chart of the calibration procedure is shown in Fig. 7.

A properly synthesized particle assembly of the ceramic material is the key for the subsequent fracture modeling of the ceramic laminates. The procedures for the material synthesis in PFC2D are standardized and therefore independent from the types of materials. Different micro-properties for different materials can be calibrated accordingly and then assigned correspondingly to the particle assemblies.

2.1 Particle Assembly Preparation

The particle assembly to resemble any given physical material is usually been prepared with a simple form. Non-uniform-sized particles which confined by parameters $R_{\max}/R_{\min}$ and $R_{\min}$ (R is the particle radius) are generated in the defined sample geometry (i.e. particles are filled into the geometry). An equilibrium state of the particle packing is achieved by setting proper isotropic stress to the assembly; this avoids the internal stress states at the particle contacts which might have influences on the subsequent fracture modeling. To assure that each particle obtains sufficient contact with neighboring particles; particles with less than three contacts with their neighbors are eliminated. Then, parallel bonds are installed at each particle contact.

Usually, the particle size is determined by the sample size and fracture toughness of the modeled material. However, another important parameter should be taken into account in this study, which is the ratio of the thickness of the ceramic layer and

interlayer (normally between 15:1 to 30:1) [3, 23, 50, 51]. In order to ascertain that the minimum particle radius meets the thickness of the thin interlayer, taking the computational resources and efficiency into consideration too, we first determined the average particle radius as $R = 4.4\,\mu m$, the ratio $R_{\max}/R_{\min} = 1.5$ and the sample size as $0.4\,mm \times 2\,mm$. According to Eq. (25), by substituting $\alpha = 2.26$ and $\beta = 0.66$ [40, 47] we obtain

$$K_{Ic} = 0.66 \cdot \sigma_t' \cdot \sqrt{\pi \cdot 2.26 \cdot 4.4 \cdot 10^{-6}\, m} \tag{26}$$

For silicon carbide (SiC) ceramic material, depending on different sintering a wide range of K_{Ic} and strength values have been reported. Here we choose $\sigma_t' = 1200 MPa$ and apply to Eq. (26), then we get

$$K_{Ic} = 4.4\ MPa\sqrt{m} \tag{27}$$

which is a reasonable value for SiC [52, 53]. Accordingly, $R_{\min}$ is calculated as

$$R_{\min} = 2R - R_{\max} = 2R/2.5 = 3.5\ \mu m \tag{28}$$

With the same particle assembly, $K_{Ic} = 0.4\ MPa\sqrt{m}$ and $\sigma_t' = 100\ MPa$ are assumed for graphite (varied data are reported [54, 55]).

In Table 1, parameters used for the particle assembly preparation are summarized.

Table 1: Parameters for particle assemblies.

Parameters	SiC	C
Length *L* (*mm*)	2.0	2.0
Height *H* (*mm*)	0.4	0.4
Average particle radius *R* (*μm*)	4.4	4.4
Ratio of particle radius R_{max}/R_{min}	1.5	1.5
Fracture toughness K_{Ic} (*MPa* $m^{1/2}$)	4.4	0.4

2.1.1 Initial Particle Compaction

A box with 4 mutually perpendicular walls defines an area of $0.4mm \times 2mm$. Particles with non-uniform-size (bounded by $R_{\min}$ and $R_{\max}$) are filled into the box as shown in Figure 9. Command ***GENERATE*** [38, 39] is used to create particles in the defined region. In order to ensure a tight initial packing for the bonded particle assembly, the number of particles is determined by setting the gross porosity of the assembly to be 0.16, which is a default value of the program and cannot be specified by user [39, 56, 57]. An estimated particle number is calculated automatically by program with the average particle radius and porosity. Particles with artificially small radii (usually bounded by $0.5R_{\min}$ and $0.5R_{\max}$) are then been distributed randomly (no overlapping) into that specific area. Then, the particles are expanded gradually until the default porosity is achieved. At the end of this step, all four walls are set to be frictionless to allow particles to move and an initial compaction of those particles is obtained (Fig.10).

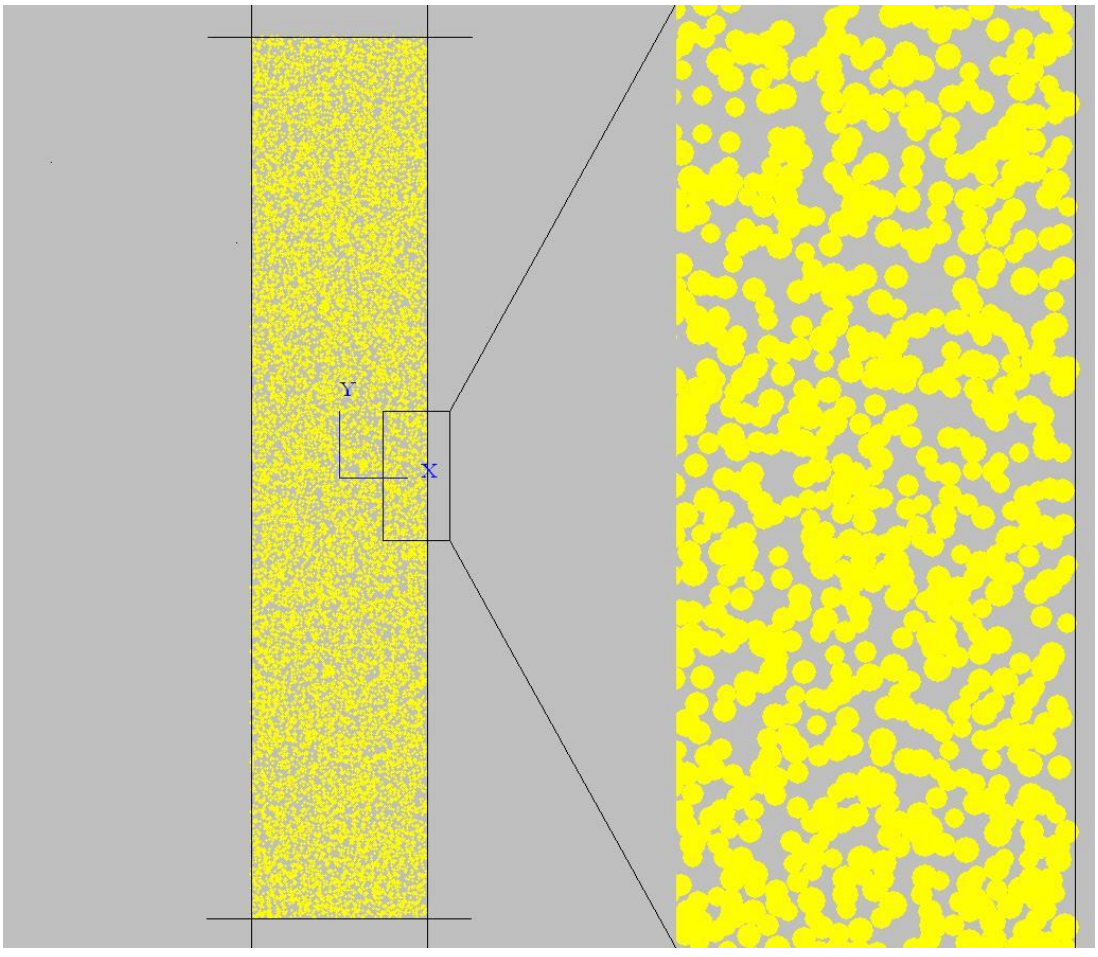


Figure 9: Initial packing of particles with artificial small radii.

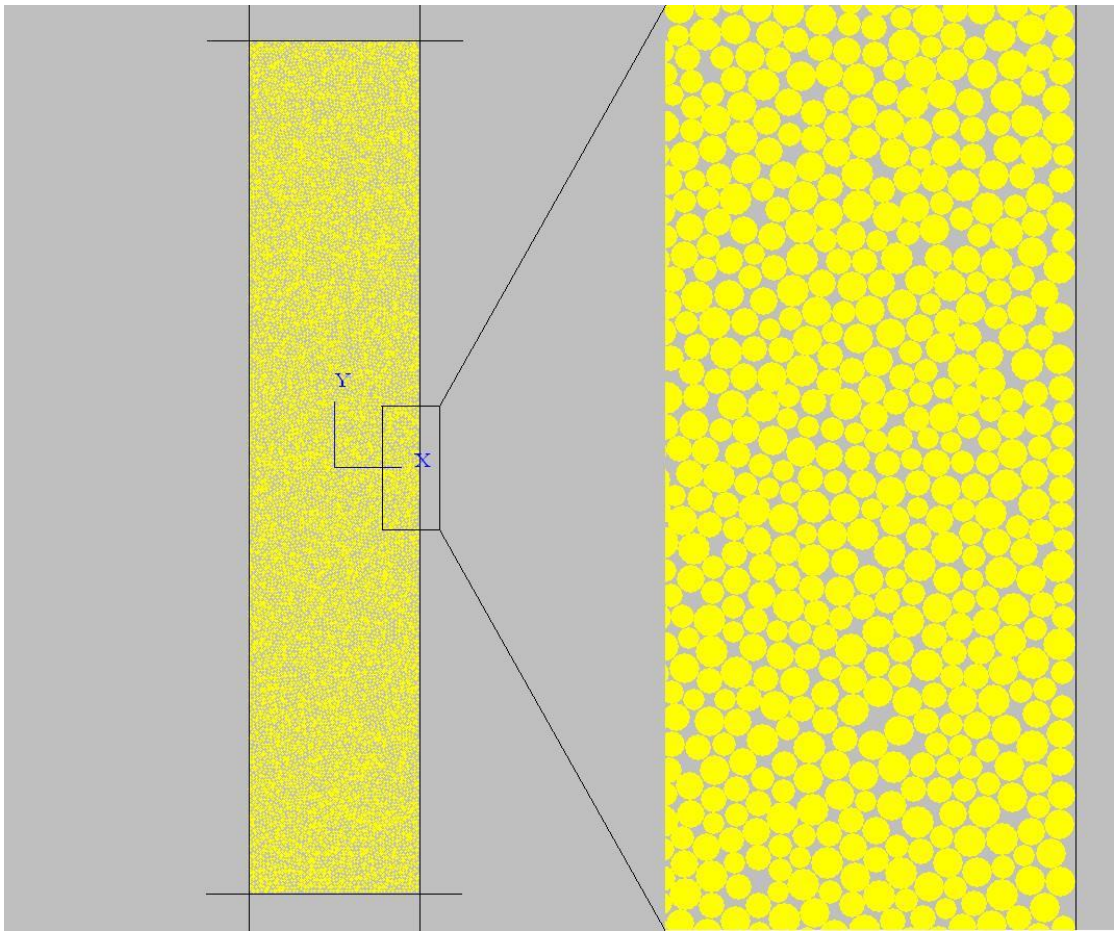


Figure 10: Initial compaction of particles with their final radii.

2.1.2 Installation of Specific Isotropic Stress

Before the parallel bonds are installed, particles are allowed to slide and rotate freely. This helps the particle assembly to achieve the equilibrium state (statistically isotropic) to avoid undesired internal stress distributions. Figure 11 shown the internal stress state at the particle contacts before and after this step has been executed. After sufficient iterations, the particle assembly achieved the desired isotropic stress state, *i.e.* the 1.0 MPa (less than 0.1% of the strength of parallel bond) as required isotropic stress has been set to the program at the beginning of the particle generation.

The isotropic stress is defined as the mean value of the two direct stresses σ_x and σ_y, which are the stresses on the confining walls of the particle assembly. The mechanism of this step is to modify the radius of all particles (uniformly) repeatedly in order to achieve the defined isotropic stress. This step is the most time consuming process among the whole synthesis of particle assembly as can be seen from the evolution diagram of the isotropic stress (Figure 12).

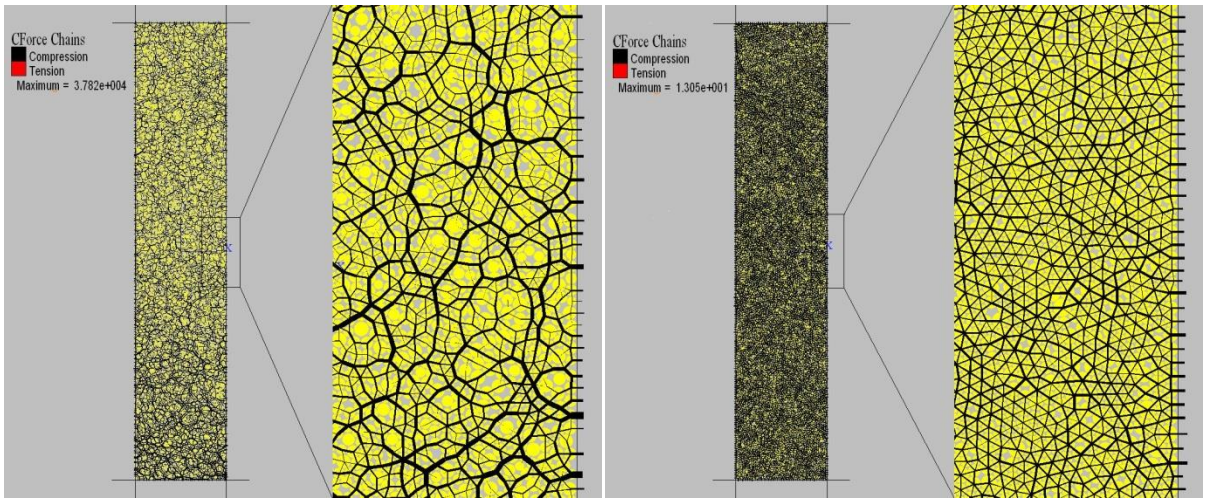


Figure 11: Contact forces before (left) and after (right) the installation of iso-stress.

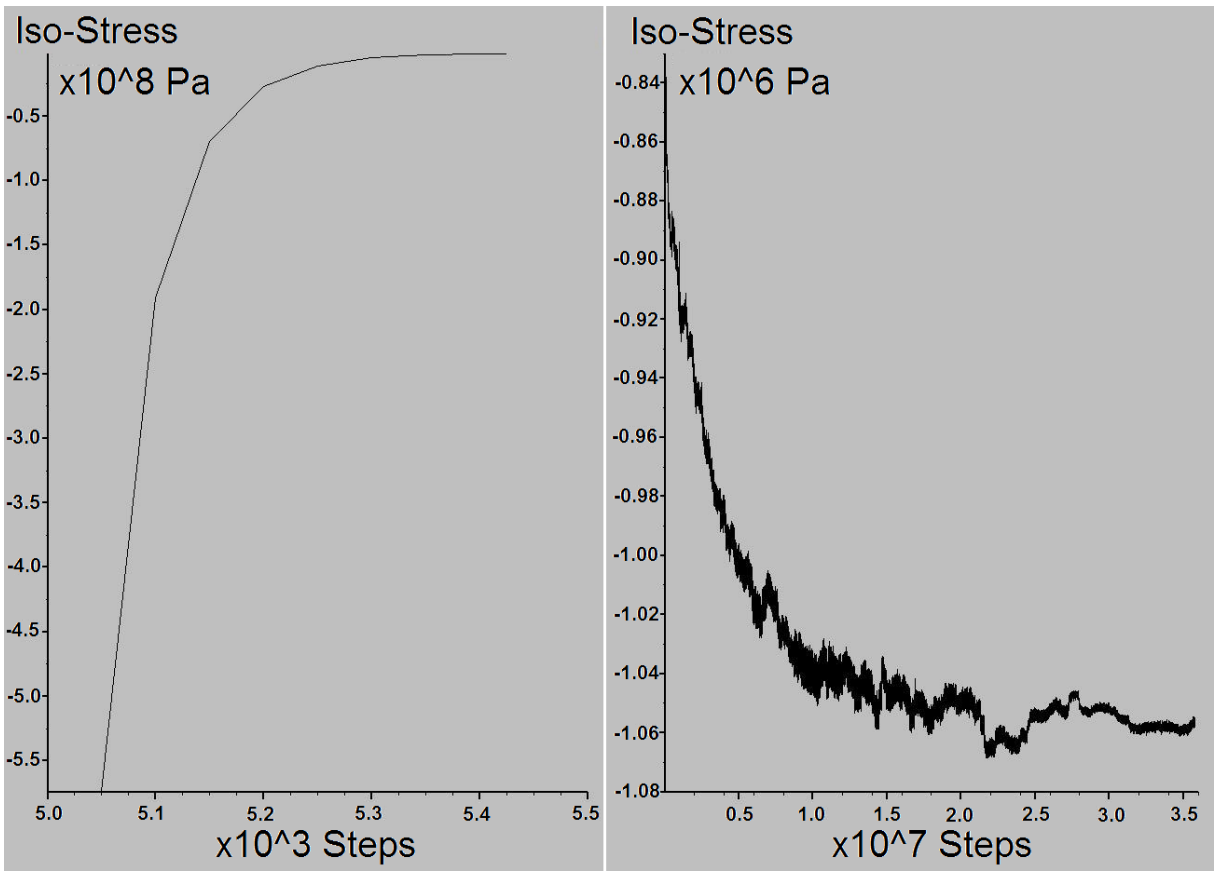


Figure 12: Evolution of the isotropic stress of the particle compaction, the first 500 cycles (left) and the rest cycles (right).

2.1.3 Elimination of the "Floating" Particles

It is inevitable to have voids in the particle assembly, as well as the so-called "floating" particles [38, 39], which have less than a certain number of contacts (in this study 3 is defined) with their neighboring particles. The achieved equilibrium state of the densely packed particle assembly should not be disturbed when the "floating" particles are eliminated or reduced. The mechanism to eliminate/reduce the "floating" particles is continuously adjust the particle radii of those floating particles till they have enough contacts meanwhile does not alternate the equilibrium of the whole particle assembly. Figure 13 and Figure 14 have shown the particle assembly before and after this elimination process. After all "floating" particles have been eliminated; the assembly is ready for installing the parallel bonds at contacts.

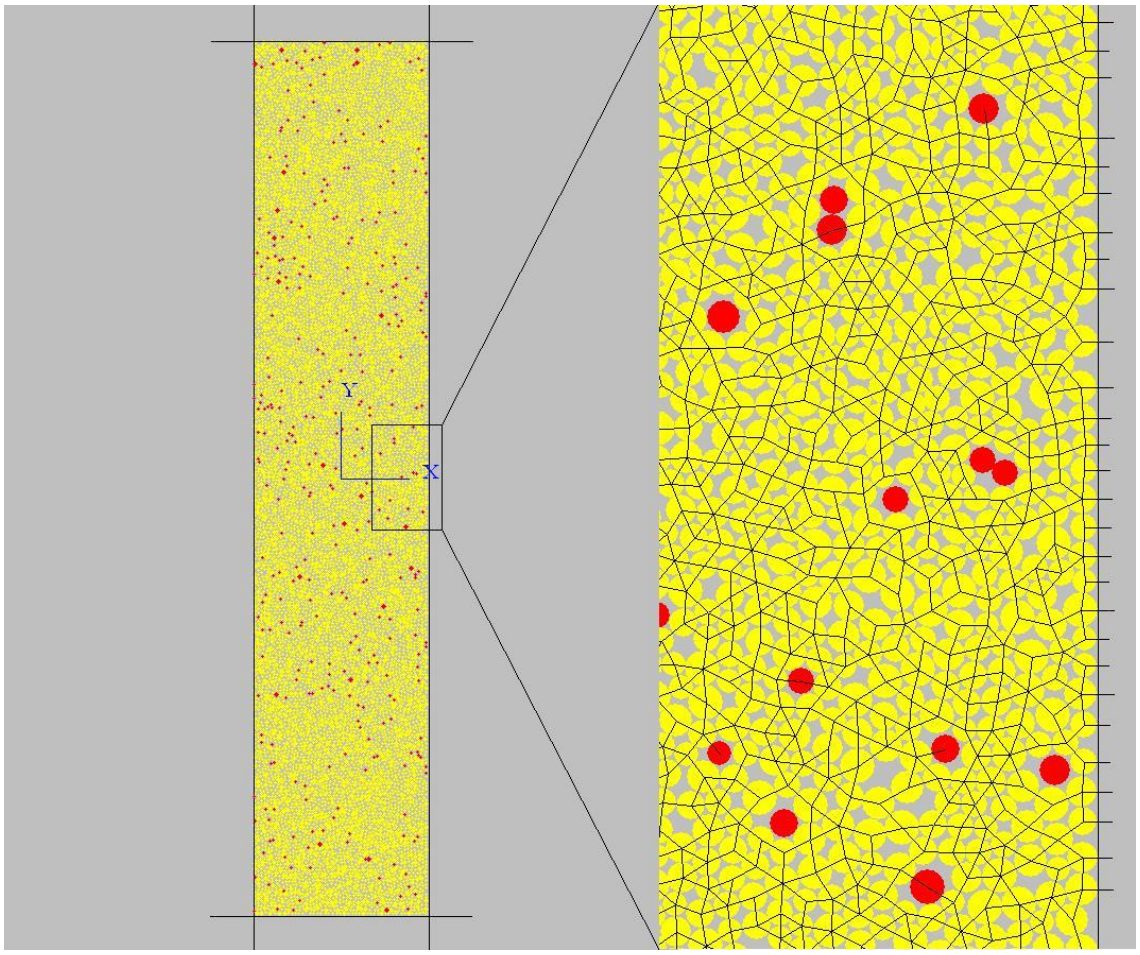


Figure 13: "Floating" particles (red) have less than three contacts (black lines).

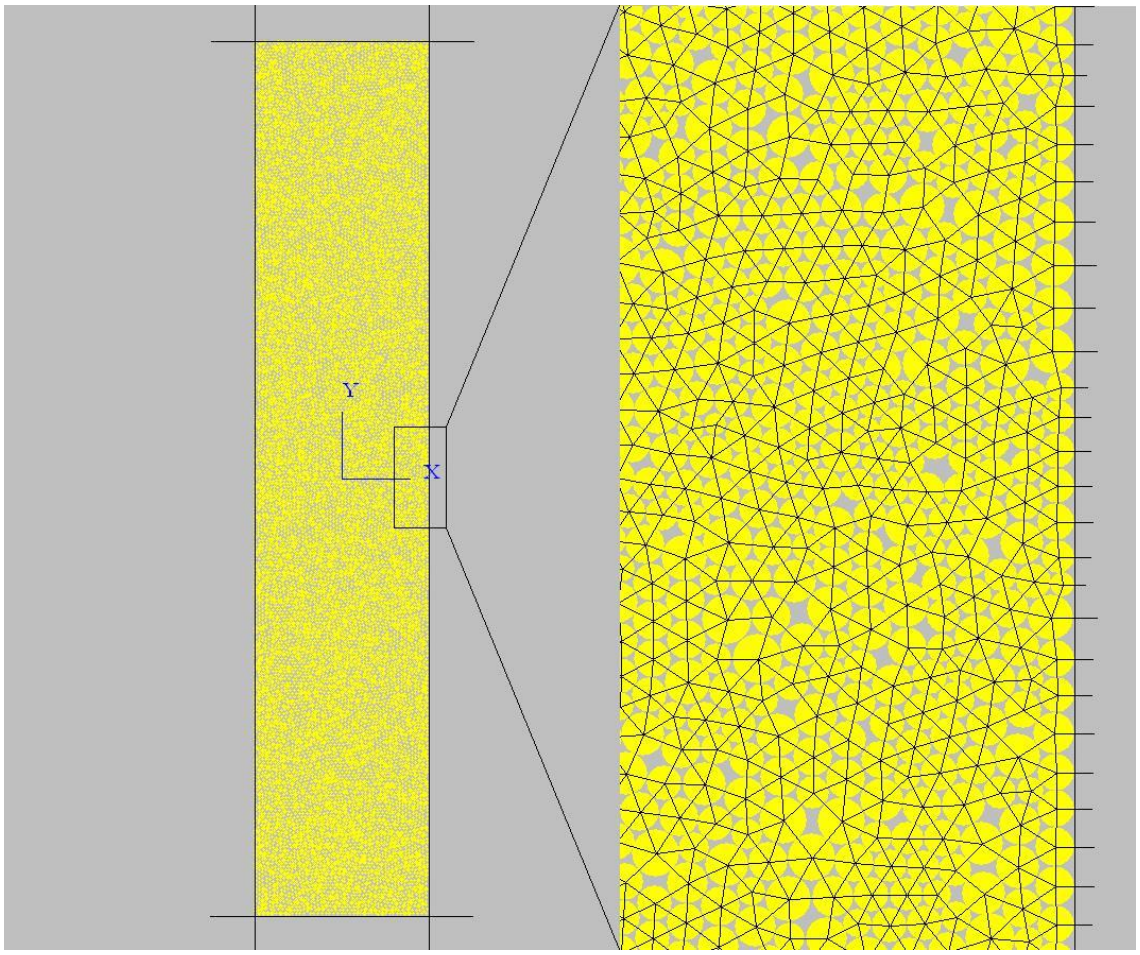


Figure 14: After elimination of "floating" particles, no particle has less than three contacts with their neighbors.

2.1.4 Installation of the Parallel Bond

Depending on different material properties, parallel bonds are necessary for particle assemblies prepared to model solid ceramic components. The micro-properties for parallel bonds installed in this step can be easily modified after individual calibration procedures have been performed for specific materials. In Table 5 and 6 (see 2.2.2) the micro-properties applied to parallel bonds in this study are listed. After this final step of the particle synthesis, the particle assembly can be removed from the box; therefore, different virtual tests can be performed on the synthesized material. Figure 15 shows the installed parallel bonds.

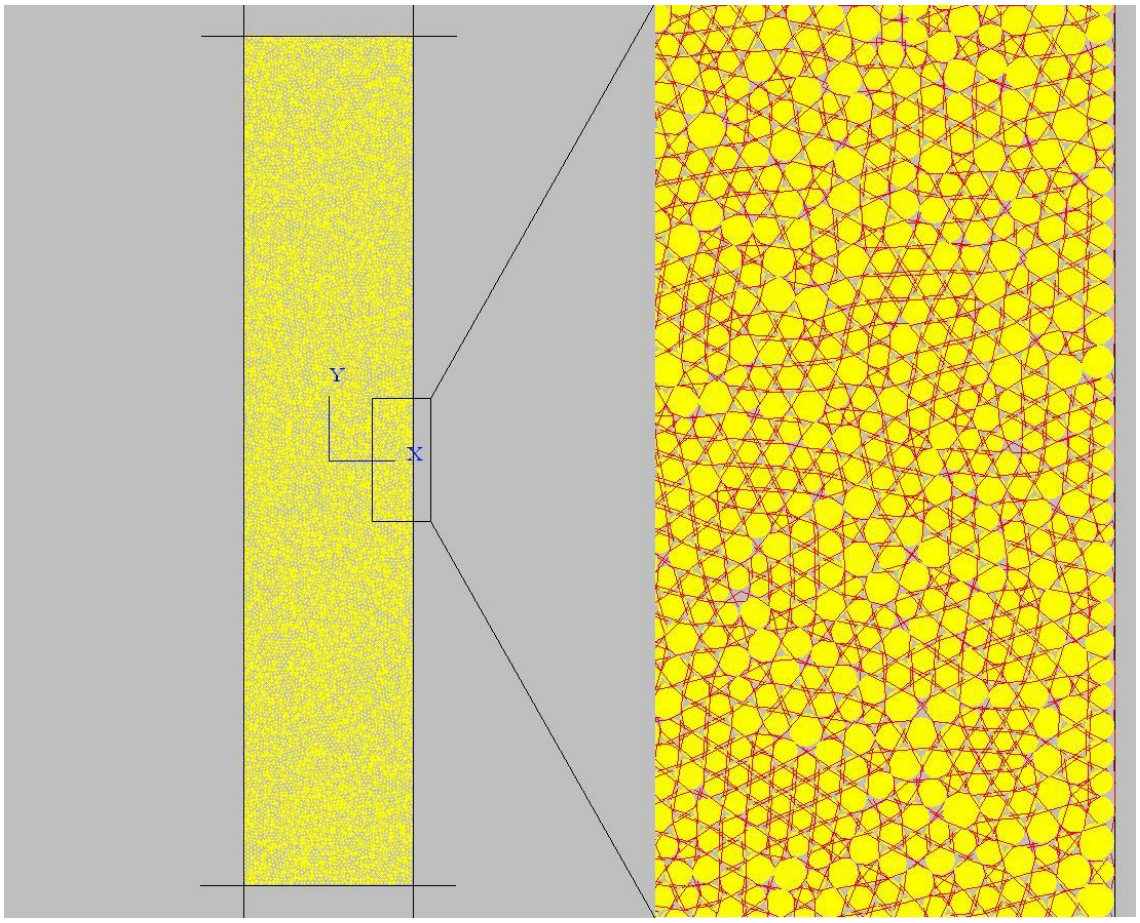


Figure 15: The installed parallel-bonds at each contact between particles (red lines).

2.2 Calibration

In general, a material is described at macro-scale by its elastic modulus, strengths, *etc*; these values can be directly assigned to the model when using continuous method as finite element method [58, 59]. However, DEM specifies properties for both particles and the contacts between them at a micro-scale by *e.g.* contact stiffness, bond strengths, friction coefficient between particles, *etc*. The correspondence between the in PFC synthesized material and the particular physical material must be established by simulated material testing, which is called the calibration process as shown in Figure 7. Since there is no complete theory to predict the macro-scale material properties from the micro-scale or vice versa, to establish the relationship between material properties at the micro- and macro-scale becomes the first prerequisite for any applications of DEM to any engineering problem [38-42]. Details of the material tests will be explained in the chapter 2.2.1, where the results of the material tests with the valid micro-properties of the BPMs are presented

individually. The calibrated macro- and micro-properties of the BPMs will be summarized in the chapter 2.2.2.

Commonly, any model of a synthetic material can be characterized by the parameters of deformability and strength. In order to have confidence that a particular model is reproducing the desired physical behavior, it is necessary to relate each model parameter to a set of relevant material properties. However, the relation between PFC model parameters and usually measured material properties is only known *a priori* for certain simple packing arrangements [38]. For an arbitrary packing of arbitrarily-sized particles, the relation can be found by means of a calibration process in which a particular instance of the synthesized material (with a particular packing arrangement and set of model parameters) is tested in the simulated set of material tests (*e.g.* unconfined compression test, three-point bend test, Brazilian test). The micro-parameters for the BPM are then chosen to reproduce the relevant material properties as measured in such tests. It is notable, however, that the particles in BPM cannot be related directly to the microstructure of the modeled material as also underlined in the PFC2D tutorial [38]: ''Although the behavior of the PFC model is found to resemble that of rock, in general, we do not associate a PFC particle with a rock grain. The assembly of bonded particles is a valid micro-structural model in its own right and should not be confused with the microstructure of rock. If it is required to model the microstructure of rock in detail, then is may be possible to use clusters of PFC particles to represent individual grains...''.

2.2.1 Material Tests /Virtual Tests

In this study, virtual tests of the BPM (the oval part in Figure 7) are performed to calibrate the SiC ceramic material and the graphite. The virtual tests included the unconfined compression test, the Brazilian test, the three-point-bending test and the single-edge-notch bending test (SENB). Once the initial set of parameters of the BPM (Table 4) have been assigned, the Elastic modulus (E), Poisson's ratio (v), unconfined compression strength (σ_c), bending strength (σ_b), fracture toughness (K_{Ic}) and Brazilian bending strength (σ_t) of the BPM will be obtained from the virtual tests for this set of parameters. These values will then be compared to the real material properties, necessary modifications upon the initial parameters will be made and iterations of the virtual tests will be performed until those values approached the real material properties. However, it has to be noted that the real material properties of

the SiC and graphite in this study are not related to a specific kind of SiC or graphite, *i.e.* neither SiC nor graphite are synthesized and tested experimentally in this study. Since the iteration of the virtual tests is a time consuming procedure in the calibration process, here we only present the results of virtual tests for the BPMs with their valid micro-parameters.

2.2.1.1 Unconfined Compression

For the sake of saving the computation time, a 0.8 *mm* x 0.4 *mm* test specimen, which contains 4470 particles is synthesized for the test. The ratio of the largest particle size to the smallest is set to 1.5 [40, 47, 57]. The movement of the vertical walls is 0.05 *m/s* [40, 47, 57]. Figure 16 (left) shows the result of the unconfined compression test of the specimen. The test results (unconfined compression strength and elastic modulus) are listed in Table 2 and 3.

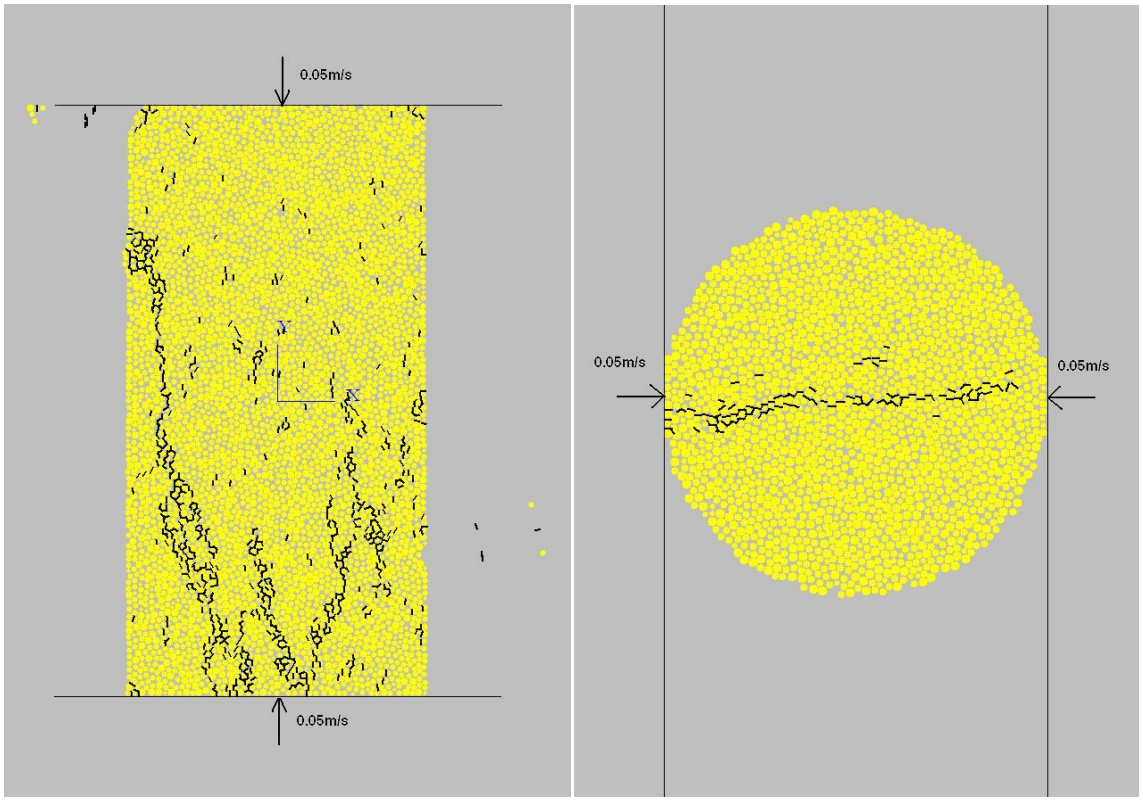


Figure 16: The unconfined compression test (left) and the Brazilian test (black lines depict the bonds which failed by tensile) [57].

2.2.1.2 Brazilian Test

The Brazilian test disk is 0.2 *mm* in radius and contains 1773 particles. Figure 16 (right) illustrated the crack in the specimen during the test [57]. The test result is

listed in Table 2. The calibrated Brazilian tensile strength is higher than experimental measured value; this is due to the size effect of the Brazilian test [40, 60, 61]. Although the Brazilian test is not commonly applied in ceramic material and infrequent test result has been reported for SiC material and graphite, it is a standard part of the virtual tests that defined in *PFC2D.* For the completeness we have conducted this test and listed the result in this study.

2.2.1.3 Three-Point Bending Test

The specimens for the three-point-bending test and the single-edge-notch bending test are 1 *mm* in length and 0.2 *mm* in width as shown in Figure 17 [57]. The distance between the two supports is 0.85 *mm*. The loading wall is moving at 0.05 *m/s* [40, 47, 57] in negative x-direction. The bending strength is calculated as $\sigma_b = 787\ MPa$ by setting the maximum load of $P = 2.468 \times 10^4\ N$ into Eq. (29) [62]:

$$\sigma_b = \frac{3PL}{2BW^2} \tag{29}$$

where P is the applied load, B is the thickness of the specimen (unit thickness in PFC2D), L is the distance between the supporting balls and W is the width of the specimen.

2.2.1.4 Single-Edge-Notched Bending Test

A notch in 0.1 *mm* length (half of the specimen width) is introduced to the bending specimen by deleting the particles along the notch line (Figure 17). Equal loading conditions as described in 2.2.1.3 were applied. The fracture toughness is calculated according to Eq. (30) [63],

$$K_{Ic} = \frac{4P}{B}\sqrt{\frac{\pi}{W}}\left[1.6\left(\frac{a}{W}\right)^{1/2} - 2.6\left(\frac{a}{W}\right)^{3/2} + 12.3\left(\frac{a}{W}\right)^{5/2} - 21.2\left(\frac{a}{W}\right)^{7/2} + 21.8\left(\frac{a}{W}\right)^{9/2}\right] = 4.8\ MPa\sqrt{m} \tag{30}$$

where $P = 6543\ N$ is the applied load, B is the thickness of the specimen (unit thickness in PFC2D), a is the crack length, and W is the width of the specimen. The fracture toughness of BPM agreed well with the reported experimental results (Table 2).

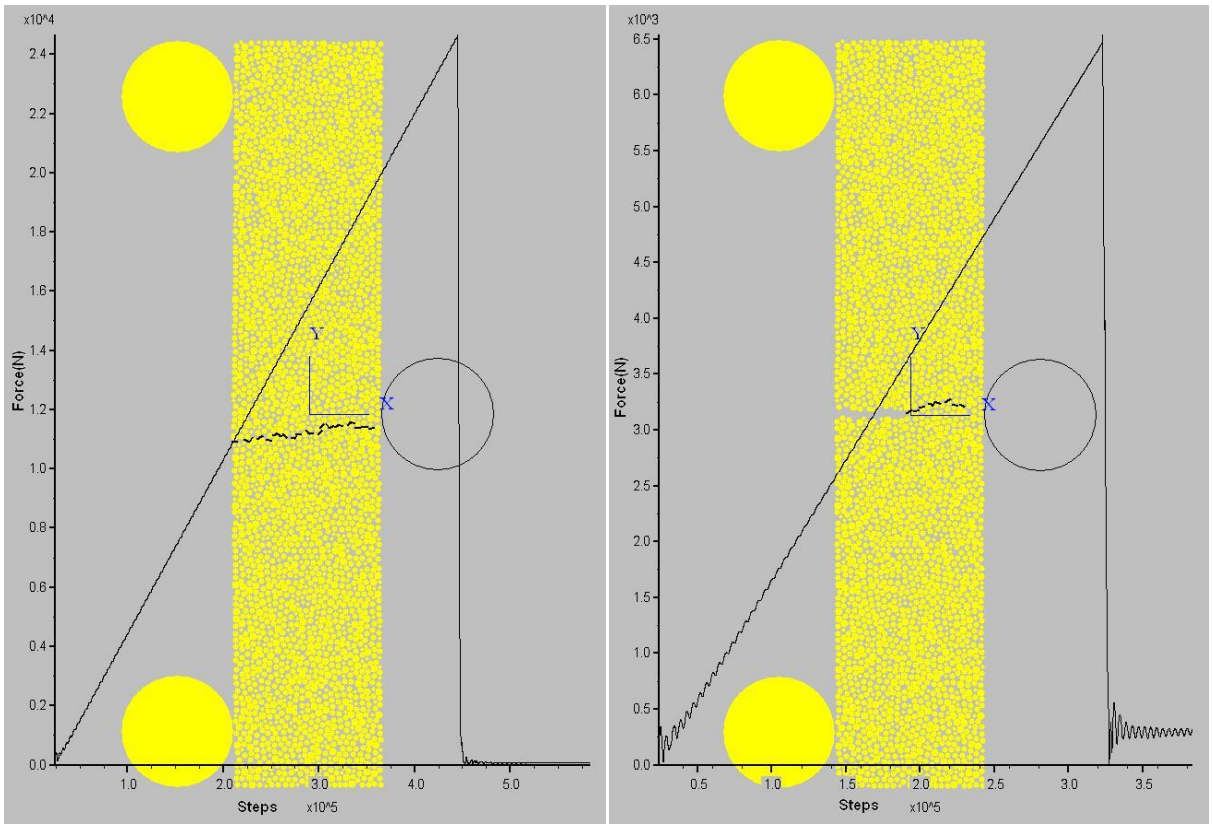


Figure 17: The three-point-bending test (left) and the SENB test (right) both with force vs. step diagram [57].

2.2.2 Macro- and Micro-Properties of the BPM

By repeatedly calibrating the macro-properties of the BPM with reported experimental values, appropriate micro-properties of the BPM (for particles and parallel-bonds) can be determined. Compared to the experimental values, macro-properties and micro-properties of calibrated BPMs (SiC and graphite) are summarized below.

In Table 2 and 3, mechanical properties and results of calibrated BPMs for SiC and graphite are listed, respectively [57]. A list of nomenclature for micro-properties which are presented in Table 5 and 6 is summarized in Table 4 [57]. The micro-properties for both the particles and parallel-bonds in the BPMs are summarized in Table 5 and 6 for SiC and graphite, respectively [57].

Table 2: Calibrated mechanical properties of SiC [57].

Mechanical Properties	Ref. [52, 53, 60,64]	BPM SiC
Elastic modulus *E* (*GPa*)	420[60]	428
Poisson's ratio *v*	0.14	0.14
Unconfined Compression Strength σ_c (*MPa*)	2000	1985
Bending Strength σ_b (*MPa*)	550-835[64]	787
Fracture toughness K_{Ic} (*MPa* $m^{1/2}$)	4.4	4.8
Brazilian tensile strength σ_t (*MPa*)	214[60]	414

Table 3: Calibrated mechanical properties of graphite.

Mechanical Properties	Ref. [54 , 55]	BPM C
Elastic modulus *E* (*GPa*)	9.8-12	11.5
Poisson's ratio *v*	0.17-0.23	0.18
Unconfined Compression Strength σ_c (*MPa*)	69-180	162.7
Fracture toughness K_{Ic} (*MPa* $m^{1/2}$)	0.4-2.4	0.4
Bending Strength σ_b (*MPa*)	4.8-92	15

Table 4: Nomenclature for micro-properties of BPMs [57].

E_c	Young's modulus of the particle
$\overline{E}_c$	Young's modulus of the parallel-bond
$\overline{\sigma}_n$	Tensile strength of the parallel-bond
$\overline{\sigma}_s$	Shear strength of the parallel-bond
k_n / k_s	Ratio of normal to shear stiffness of the particle
$\overline{k}_n / \overline{k}_s$	Ratio of normal to shear stiffness of the parallel-bond
μ	Friction coefficient
$\overline{\lambda}$	Radius multiplier of the parallel-bond
R_{max}/R_{min}	Ratio of particle's maximum radius to minimum radius
ρ	Density of the particle

Table 5: Micro-properties for particles and parallel-bonds in BPM of SiC [57].

Particles	Parallel-bonds
E_c = 275 *GPa*	$\overline{E}_c$ = 275 *GPa*
μ = 0.5	$\overline{\lambda}$ = 1
ρ = 3100 *kg/m*^{3}	$\overline{\sigma}_n$ = 1.2 ± 0.12 *GPa*
R_{max}/R_{min} = 1.5, R_{min} = 3.5 *μm*	$\overline{\sigma}_s$ = 9.6 ± 0.96 *GPa*
k_n / k_s = 1.1	$\overline{k}_n / \overline{k}_s$ = 1.1

Table 6: Micro-properties for particles and parallel-bonds in BPM of graphite.

Particles	Parallel-bonds
E_c = 8 *GPa*	$\overline{E}_c$ = 8 *GPa*
μ = 0.5	$\overline{\lambda}$ = 1
ρ = 1730 *kg/m*^{3}	$\overline{\sigma}_n$ = 100 ± 1.0 *MPa*
R_{max}/R_{min} = 1.5, R_{min} = 3.5 *μm*	$\overline{\sigma}_s$ = 100 ± 1.0 *MPa*
k_n / k_s = 1.6	$\overline{k}_n / \overline{k}_s$ = 1.6

2.3 BPM of SiC-C Laminates

The BPM of SiC-C laminates is based on the SiC matrix and weak interfaces (graphite interlayers). In practice, different thickness of graphite interlayer can be manufactured, from 5 *μm* to 10 *μm* [50]. The ratio of the thickness of SiC lamella to the graphite layer ranges between 15 to 30 [3, 23, 50, 51]. To model the weak interfaces, two different ideas about the model construction are considered. One idea was to include the physical thickness of the weak interlayer into the BPM and two different thicknesses (30 *μm* and 10 *μm*) of the weak interlayer were compared. The other idea was to employ "Joint-Plane" [38] from PFC2D to represent the weak interfaces and ignore the physical thickness of the weak interlayer.

2.3.1 BPM with Graphite Layer

Unlike the method to apply Joint-Plane, the physical thickness of the graphite layer is considered in the BPM of SiC-C laminate (Fig.18).

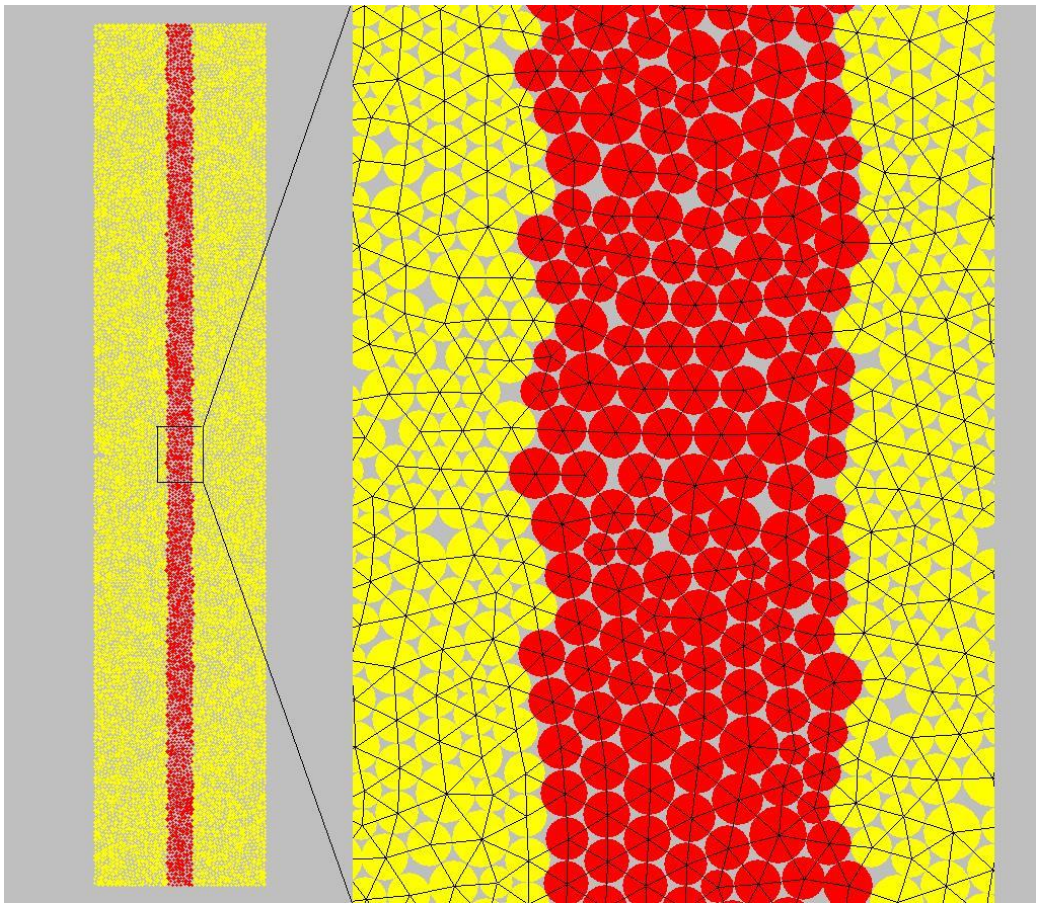


Figure 18: The particle assembly with the interlayer thickness of 60 *μm*, the magnified picture is on the right (60 *μm* was presented here to shown clearly the interlayer).

2.3.2 BPM without Graphite Layer

The "Joint-Plane" in PFC2D is designated to model the surfaces/lines along which sliding and separation may take place in geological simulations [38]. Since weak interfaces are thinner than the SiC-lamella [3, 50], the thickness of the weak interface itself may be ignored in the BPM for simplification reasons. The weak bonding feature of the interface is integrated into the BPM by setting a lower bond strength value for the bonds which are located at the weak interfaces (Joint-Plane) in the SiC-C laminate. Figure 19 illustrated the presence of weak bonds which are used to mimic the weak interfaces without considering their thickness [57]. The bond strength is assumed to be 100 *MPa* (the same value as the bond strength calibrated for graphite, discussions about this value is presented in 4.2.3). Although the accurate value of this bonding strength is important for the BPM of SiC-C laminate, the experimental value is not yet available. From another point of view, with the help of the DEM modeling an accurate value might be evaluated reversely. Bending bars with size 0.4

mm x 2 *mm* are prepared to model SiC-C laminates. In order to examine the dynamic crack propagation process in the laminate, an initial crack in 0.02 *mm* length is introduced to the specimen (Fig.20).

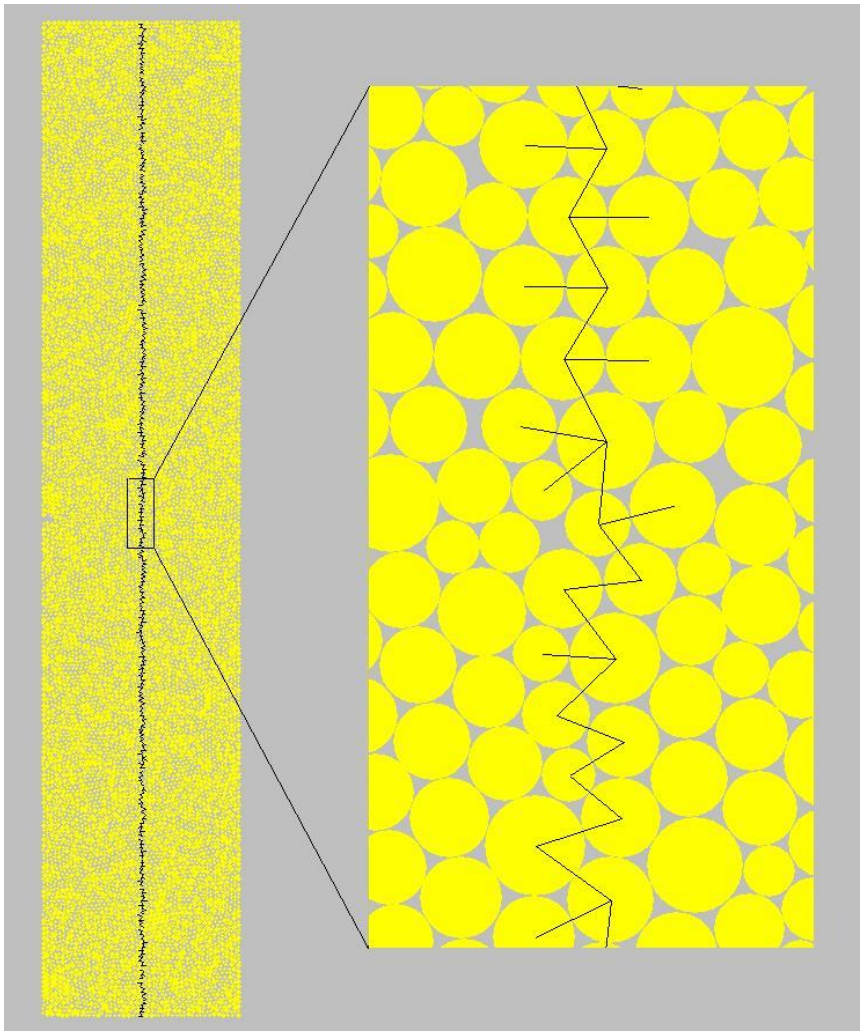


Figure 19: Overview of the BPM of SiC-C laminate (left) and weak bonds which assigned lower strength values at the weak interface (right) [57].

2.4 Load and Boundary Conditions

2.4.1 Loading

The load is applied to the test specimens through the loading wall, although forces can be applied directly to the particles. Evolution of the loading force is plotted by recording the response force on the loading wall with cycling steps. The loading wall is moved in negative x-direction at a constant speed of 0.05 *m/s* [40, 47, 57]. In order to minimize the oscillation of the particle system, the loading speed is achieved by

"Servo-Wall" mechanism [39], which gradually accelerates the wall to the aimed speed in 20 stages (each stage contains 25 steps).

2.4.2 Boundary Conditions

Two supports (particle 1&2 in Fig. 20, 0.3 *mm* in diameter) are fixed both in rotation and transition. The friction coefficient between the supporting particles and the particle assembly is assumed as 0.89 [56, 57]. The distance between them is 1.7 *mm*.

2.4.3 Time Step

Generally, the time-step for a calculation cycle is determined automatically by the program itself. However, the scale of the time-step influences the accuracy and efficiency of the calculation. Since all the BPMs are based on the same particle assembly, the starting time-step of the mechanical test is the same for all BPMs. It is convenient for the tested BPM to convert the time-steps to the displacement by multiplying the time-step with the loading speed.

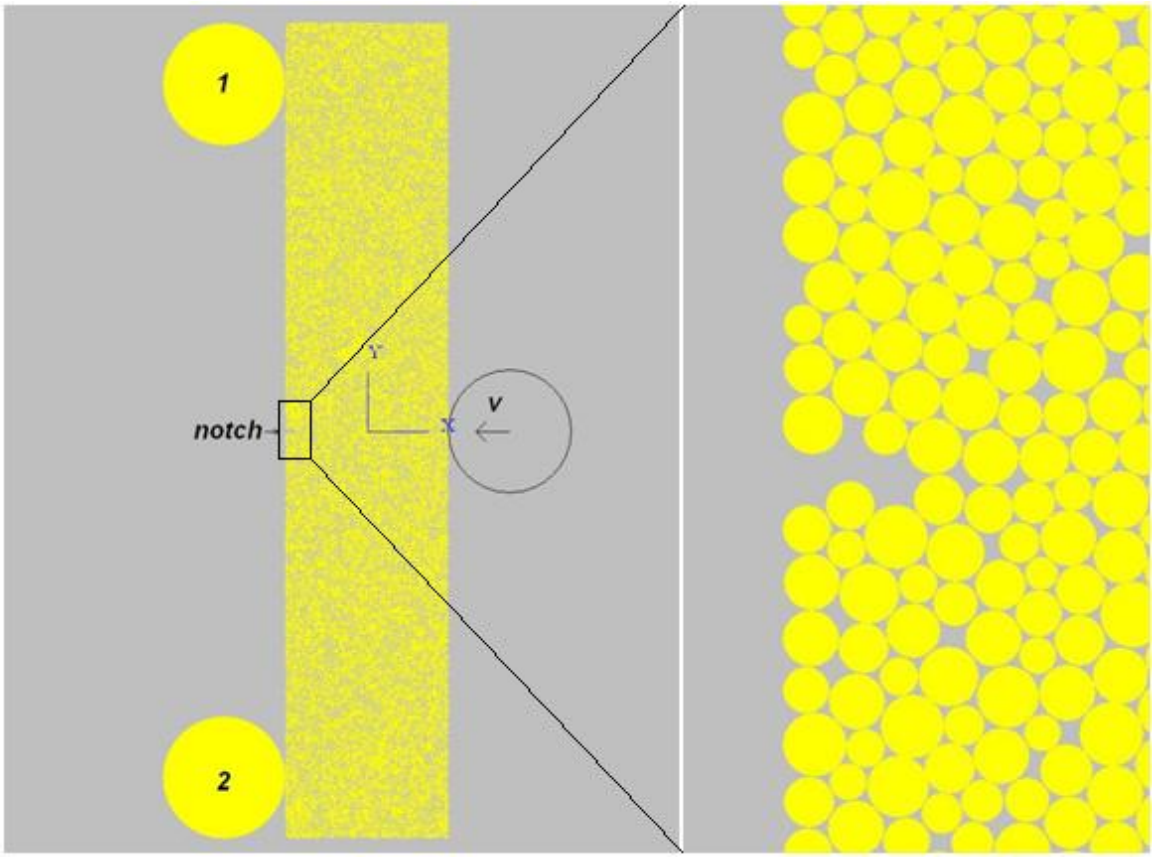


Figure 20: Configuration of the three-point-bending test (particles are in yellow, wall is the black circle) and the magnified view of the notch (right).

3. Fracture Modeling of SiC Bulk Material and SiC-C Laminates

3.1 Fracture Modeling of SiC Bulk Material

A monolithic SiC bending bar with the same geometry (0.4 *mm* x 2 *mm*, 0.02 *mm* notch) is also synthesized to compare with laminate specimens. Same loading conditions as three-point-bending test in the calibration process are applied. The maximum loading force of 3.324×10^{4} *N* and displacement of 1.6065×10^{-3} *mm* are obtained from Figure 21 [57]. According to Eq. (29) [62] and Eq. (30) [63], the bending strength and the fracture toughness of this notched bulk sample are calculated as 530 *MPa* and 3.9 *MPa* $m^{1/2}$, respectively. As expected, the sample deformed elastically first, when achieved the maximum load the crack initiated from the notch propagated simultaneously through the thickness of the sample. The failure of the sample is catastrophic as expected from brittle materials. The phenomenon observed at B (Fig.21), i.e. the load plateau occurred around B, will be discussed in 4.2.1.

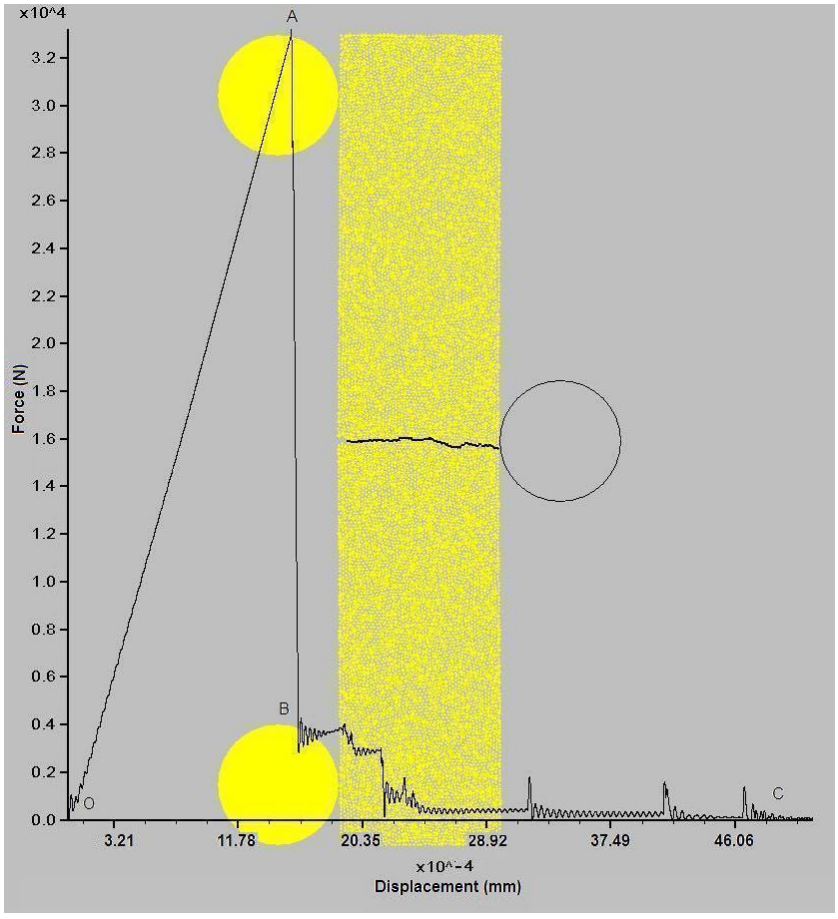


Figure 21: The load-displacement diagram for notched bulk SiC sample [57].

3.2 Fracture Modeling of SiC-C Laminates

In this chapter, results of the BPMs included/excluded the thickness of the graphite interlayer are presented. Same loading conditions as in 3.1 are applied. In 3.2.1, two different interlayer thicknesses, i.e. 30 *μm* and 10 *μm* are considered. Micro-properties of the calibrated graphite (Table 6 in 2.2.2) are applied to particles and parallel-bonds of the interlayer. In 3.2.2, up to 9 weak interfaces represented by "Joint-Plane" were introduced into the BPM of SiC (excluding the weak interlayer thickness).

3.2.1 BPM Including the Thickness of Graphite Interlayer

In order to find out whether the thickness of the thin graphite interlayer can be simplified in the BPM of SiC-C laminate, results of BPMs with two different thickness (30 *μm* and 10 *μm*) were examined. The dynamic crack propagation in each laminate tested in three-points-bending will be presented graphically. To describe the process of the crack propagation in the laminate, the force-steps (displacement) diagrams will be marked by O, A, B, C, D... at the characteristic points. The fracture behavior of each tested laminate will be described qualitatively according to different stages, which are characterized by the characteristic points in the force-steps diagram. Stages or periods in the crack propagation process will be expressed by using two characteristic points, e.g. O-A means the stage from O to A. For each stage, at least two snapshots will be presented to illustrate the dynamic progress of the crack growth in the stage. According to the load and crack length (or notch length) at the moment of the crack initiation, the resistance of crack growth of the laminate during the dynamic crack propagation will be calculated by using Eq. (30) [63].

3.2.1.1 Interlayer Thickness of 30 μm

The overview of the force-steps diagram of the sample tested in three-point-bending is shown in Fig.22. The dynamic crack propagation is depicted in Fig.23.

O-A: Elastic deformation of the sample.

A-B: De-bonding and de-lamination occurred at the interface prior the crack growth. The loading force increased further after point A. Rupture of the graphite interlayer occurred, while the cracks at the interlayer started from the end of the sample and propagated to the center approaching each other.

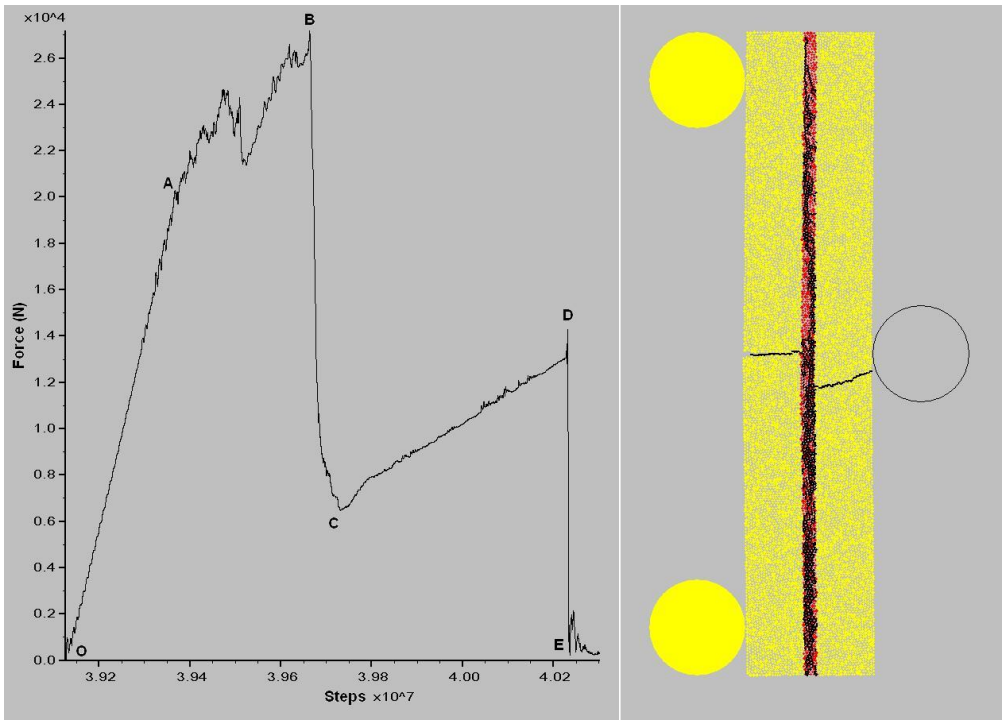
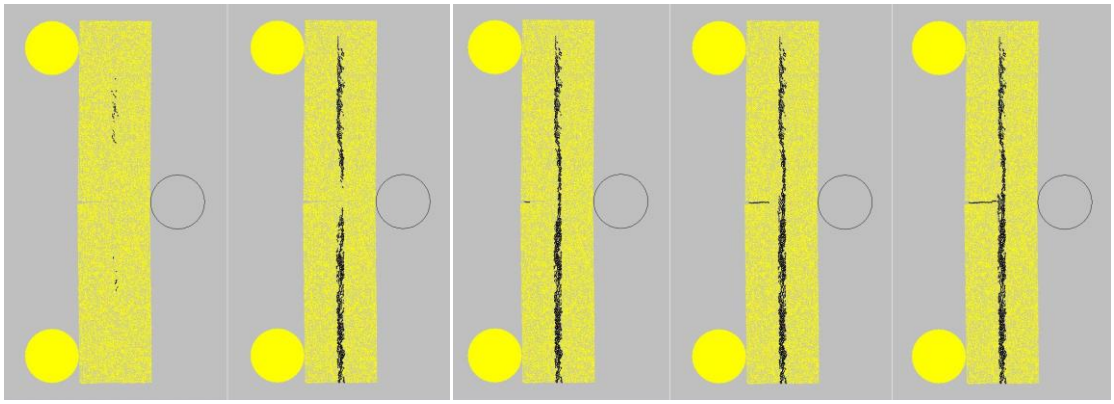
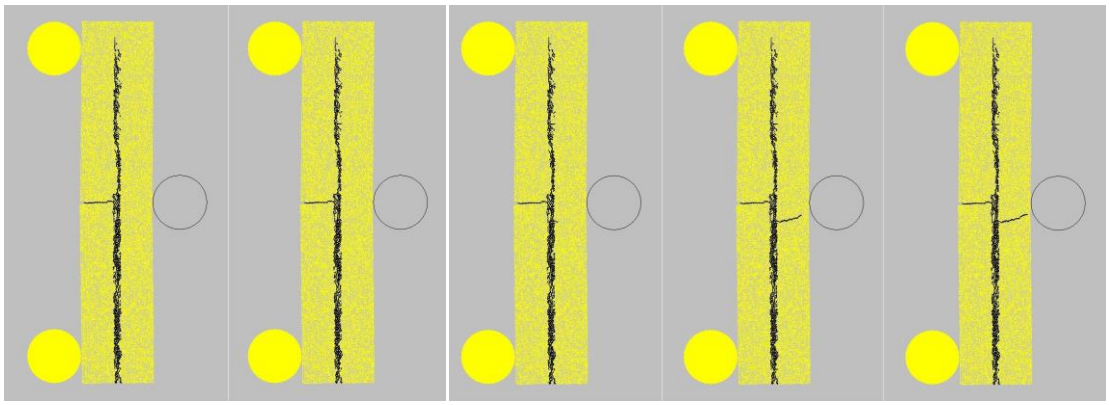


Figure 22: Load-steps diagram for SiC-C laminate with interlayer thickness of 30 *μm*.



A-B B-C



C-D D-E

Figure 23: Propagation of the crack in the laminate with a 30 *μm*-thick interlayer.

B-C: Cracks at the interlayer converged at the middle of the interlayer. The crack initiated from the notch started to travel across the sample and has been arrested at the first interlayer. The resistance of crack growth at point B was 3.2 *MPa* $m^{1/2}$.

C-D: Further de-bonding and de-lamination at the interlayer, increase of the load.

D-E: The crack has been deflected from the interlayer and extended across the residual thickness of the sample. The resistance of crack growth at point D was 6.6 *MPa* $m^{1/2}$.

3.2.1.2 Interlayer Thickness of 10 µm

The overview of the force-steps diagram of the sample tested in three-point-bending is shown in Fig.24. The dynamic crack propagation are depicted in Fig.25.

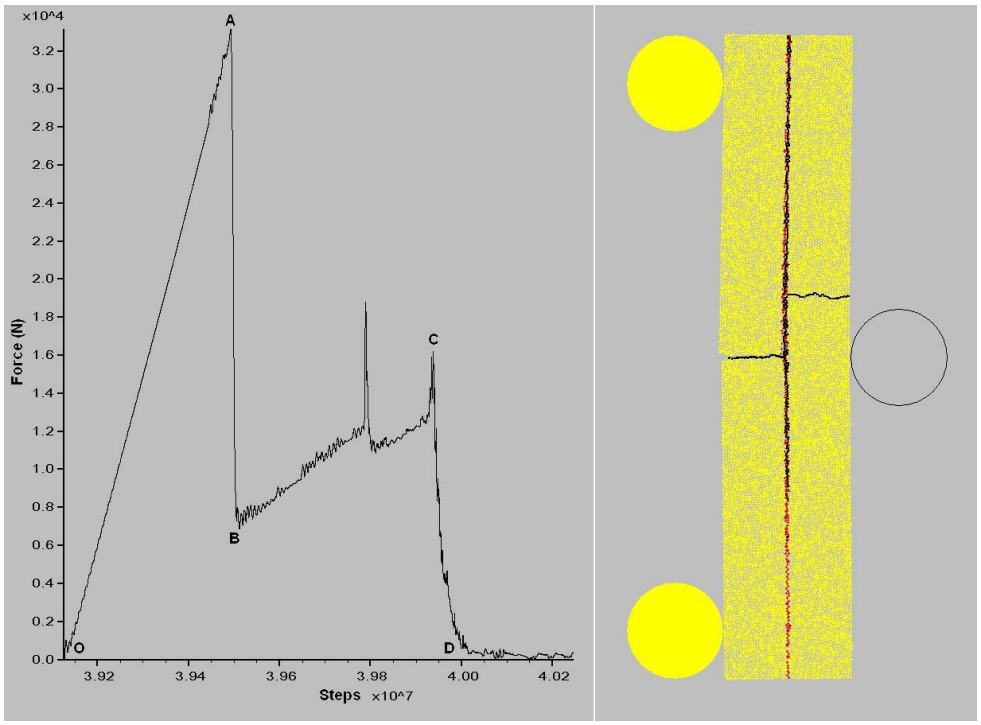
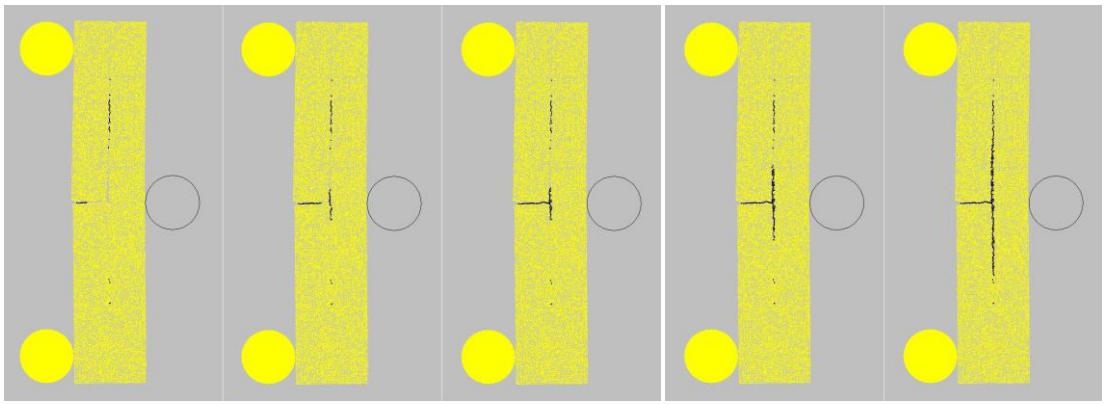


Figure 24: Load-steps diagram for SiC-C laminate with interlayer thickness of 10 *µm*.

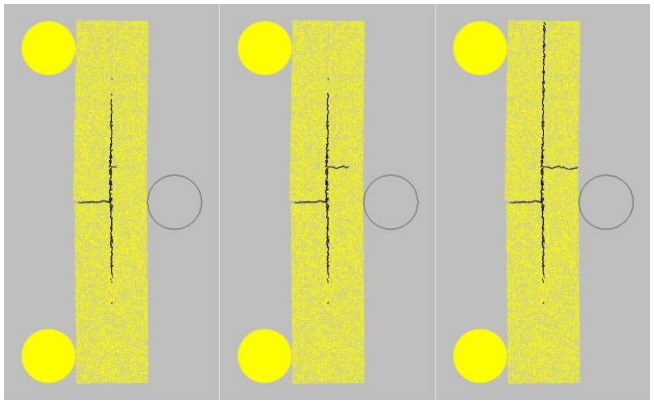
O-A: Elastic deformation of the sample. Few de-bonding occurred prior the crack growth.

A-B: The crack initiated from the notch and extended to the interlayer. The resistance of crack growth at point A was 3.9 *MPa* $m^{1/2}$.

B-C: De-lamination at the interlayer. The load increased in this stage.



A-B B-C



C-D

Figure 25: Propagation of the crack in the laminate with a 10 *μm*-thick interlayer.

C-D: The crack has been deflected from the interlayer and extended across the rest thickness of the sample. The resistance of crack growth at point C was 8.2 *MPa* $m^{1/2}$.

3.2.2 BPM Excluding the Thickness of Graphite Interlayer

The BPMs of SiC-C laminate in this section (chapter 3.2.2) are without considering the thickness of the thin graphite interlayer. In order to investigate the mechanical properties of the laminates with different number of weak interfaces, up to nine weak interfaces will be introduced to the BPM of SiC. The dynamic crack propagation and the resistance of crack growth of the laminate will be presented as the same as in chapter 3.2.1. Moreover, R-Curve behavior will be determined for each laminate by plotting the resistance of crack growth at the crack initiation points with the crack length. The results of the laminates with the weak bond strength of 100 *MPa* are chosen to be presented in this section.

3.2.2.1 One Interface

In Figure 26 the overview of the cracked laminate with single weak interface and the load vs. deformation (steps) diagram are presented. Details about crack growth are illustrated in Figure 27 and the crack growths according to the characteristic points are described as following.

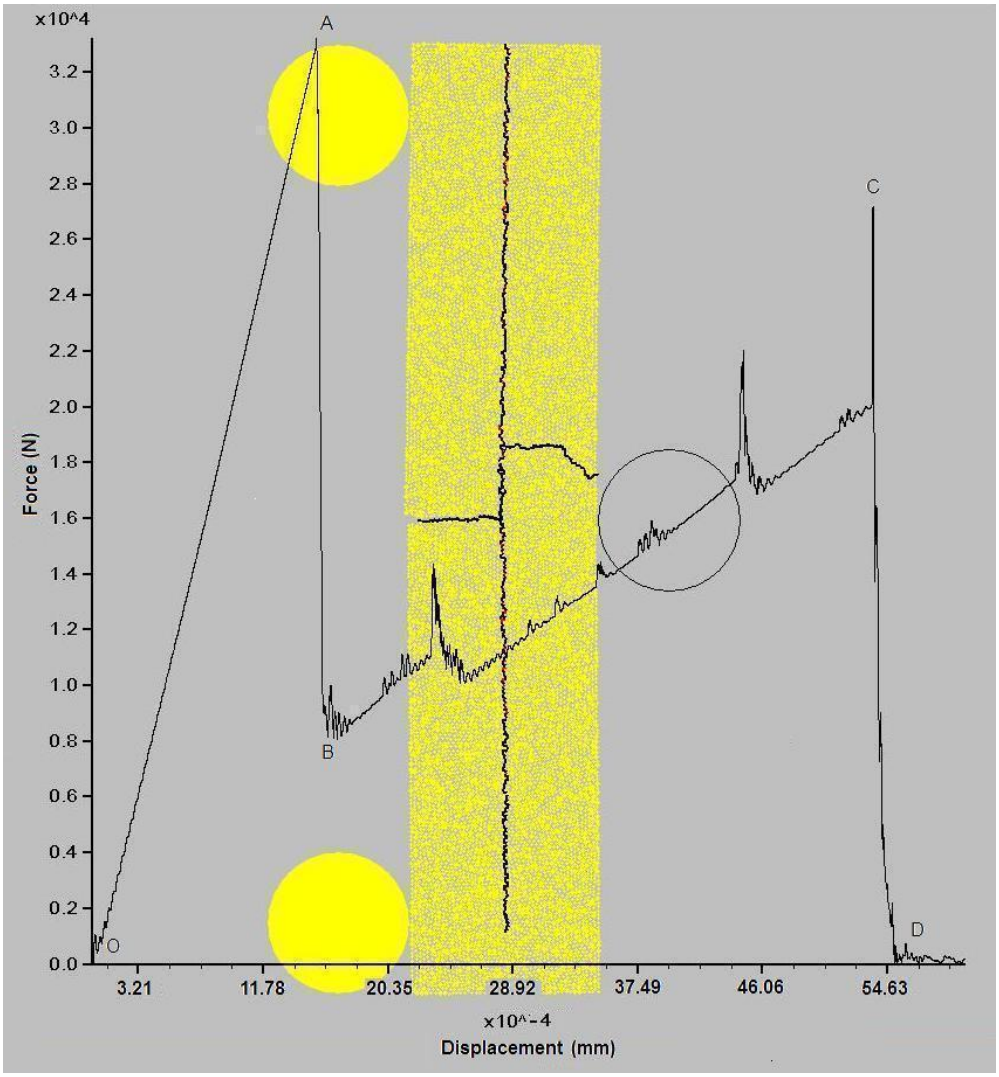
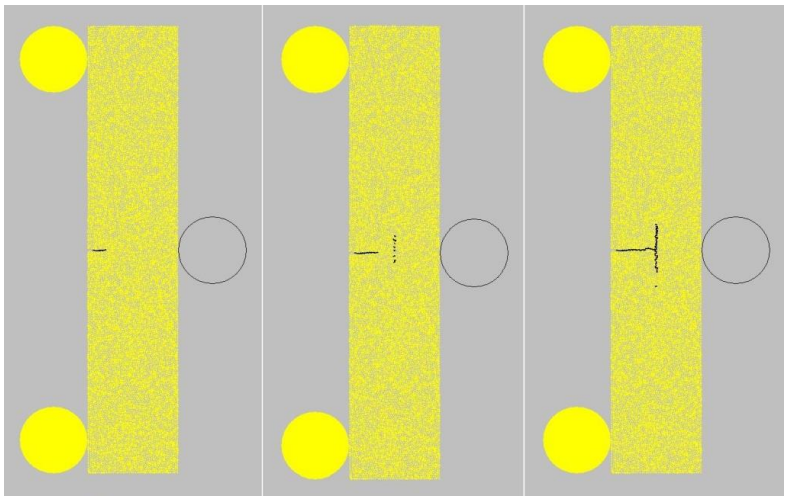
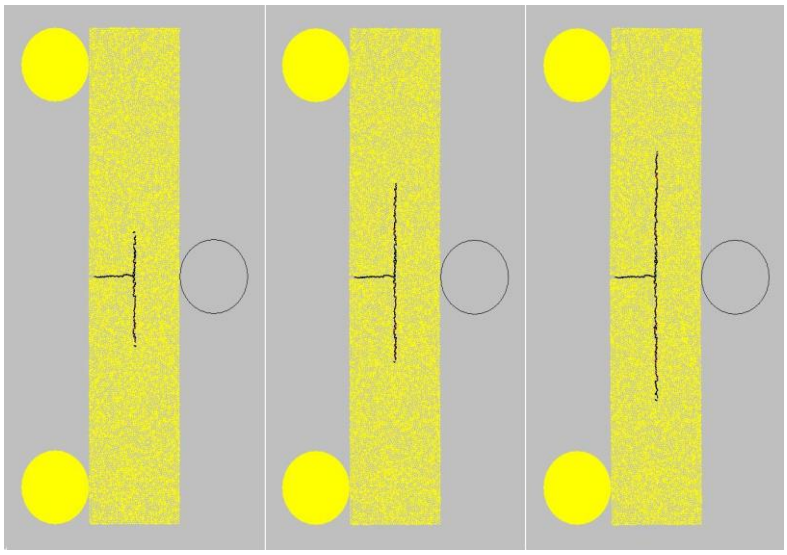


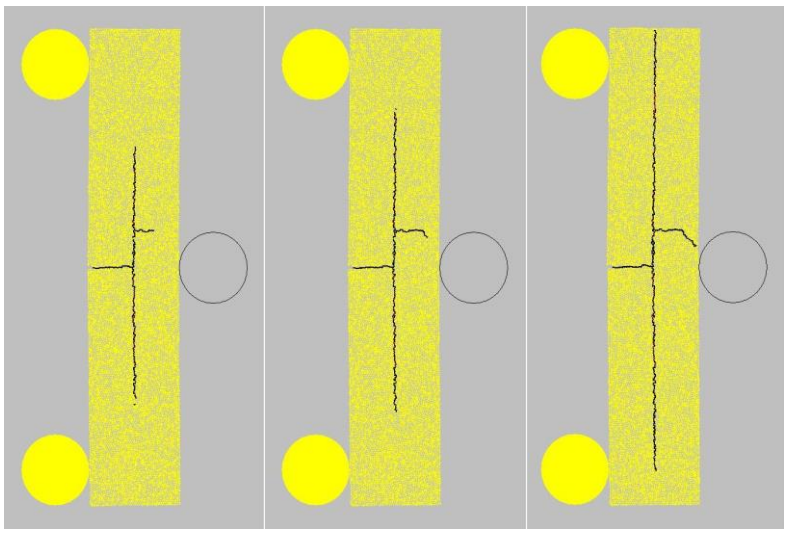
Figure 26: Force-displacement diagram of notched sample with single weak interface.



A-B



B-C



C-D

Figure 27: Propagation of the crack in the laminate with single weak interface.

O-A: Stage of the elastic deformation, no crack growth.

A-B: After achieving the strength of the SiC ceramic material (the lamella), the initial crack started to grow across the sample, which is related to the first drop in the load/deformation diagram (Fig.26). Till to a certain level of the growth, de-bonding of the weak interface in front of the main crack commenced. When the main crack arrived at the interface, it has been arrested immediately. According to Eq.(30) [63], the resistance of crack growth at point A was 3.9 $MPa\ m^{1/2}$.

B-C: During this period, the only phenomenon taken place was the de-lamination of the weak interface, which also can be counted as a toughening mechanism. This can be proven by the increase of the load in Figure 26 after the first drop in the stage A-B. As the de-lamination at the interface was insufficient to withstand the further increasing load, the second drop of the load occurred.

C-D: The main crack arrested at half of the thickness of the sample during the period B to C, has been deflected from the weak interface and preceded across the rest half of the sample till the final failure of the whole sample. According to Eq.(30) [63], the resistance of crack growth at point C was 14.9 $MPa\ m^{1/2}$.

3.2.2.2 Two Interfaces

The overview of the failed sample and force-steps diagram are shown in Figure 28 for the laminate with two weak interfaces. Crack growths in the stages from A to D are presented in Figure 29. Details about the stages are depicted below.

O-A: It is notable that the end part of the elastic deformation (Fig.28) is not linear as shown in Fig.26 for the sample with single weak interface. De-bonding of the first weak interface began prior to crack growth, since the first weak interface is closer to the notch.

A-B: The growth of the crack initiated from the notch corresponds to the first drop in Fig.28. The crack has been arrested when it arrived at the first weak interface. The resistance of crack growth at point A was 4.0 $MPa\ m^{1/2}$.

B-C: De-lamination continued at the first interface and started at the second interface until the force achieved a second maximum (at point C).

C-D: A second drop of the loading curve occurred. The deflected main crack started from the first interface and arrived at the second interface, meanwhile a new crack was initiated at the first interface. The new crack finally converged with the main crack before it meets the second interface; the main crack has been deflected again from the second interface and propagated through the thickness till the final failure of the sample. The resistance of crack growth at point C was 10.7 *MPa* $m^{1/2}$.

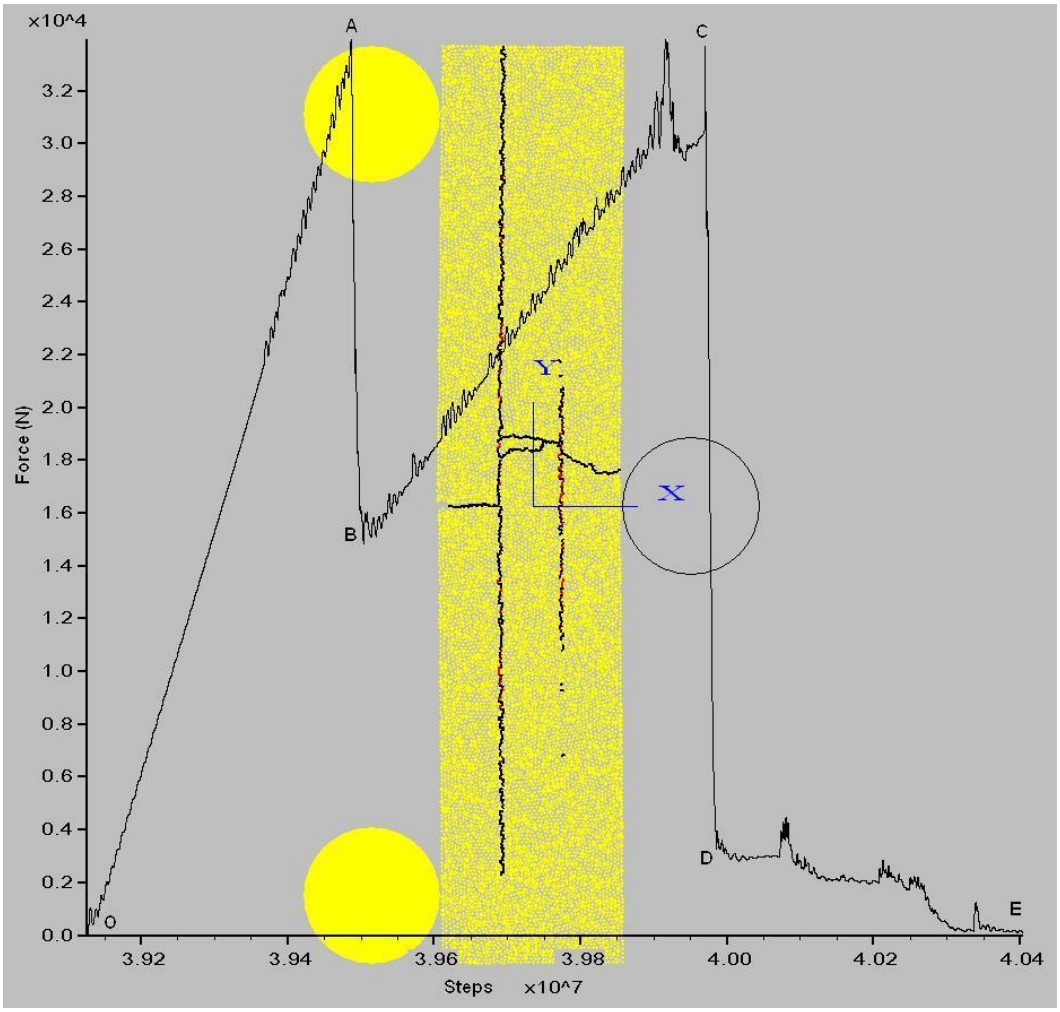
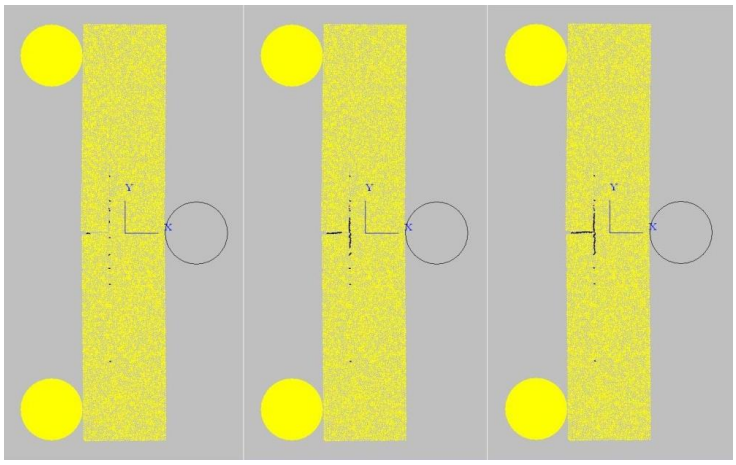
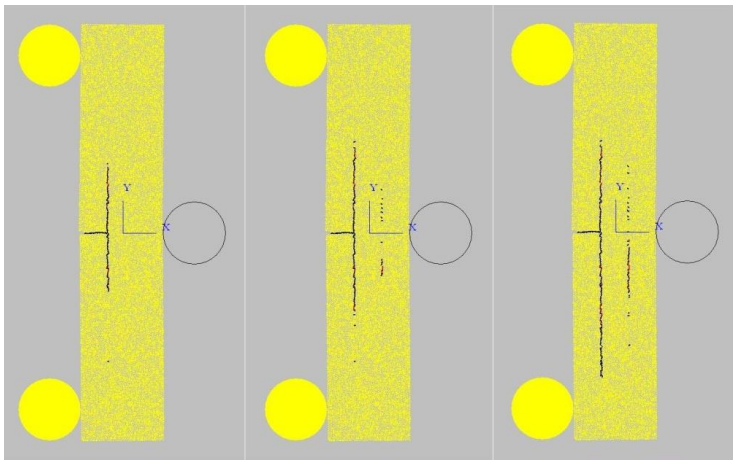


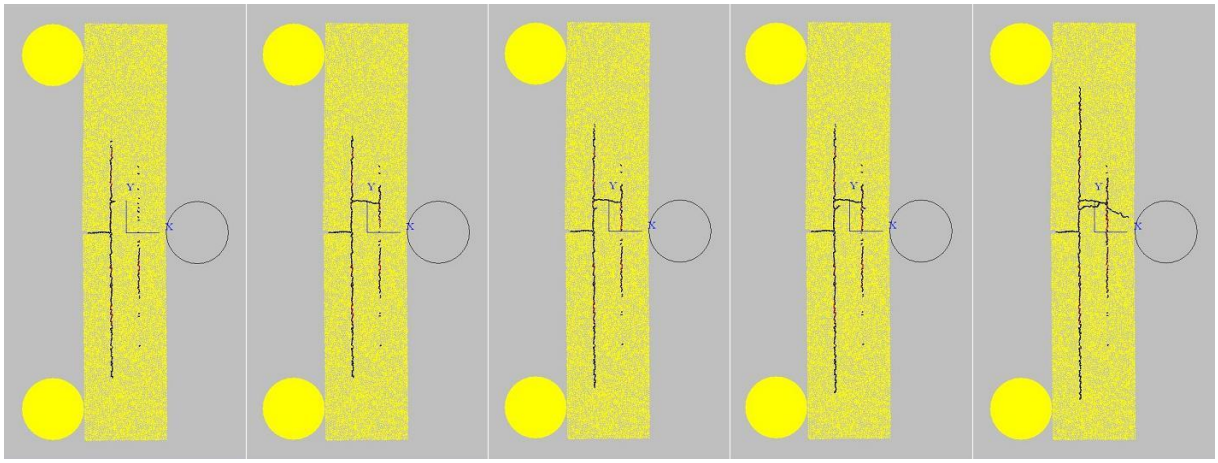
Figure 28: Force-steps diagram of notched sample with two weak interfaces.



A-B



B-C



C-D

Figure 29: Propagation of the crack in the laminate with two weak interfaces.

3.2.2.3 Three Interfaces

The overview of the failed sample and force-steps diagram are shown in Figure 30 for the laminate with three weak interfaces. Details about the stages which presented in Figure 31 are described as following.

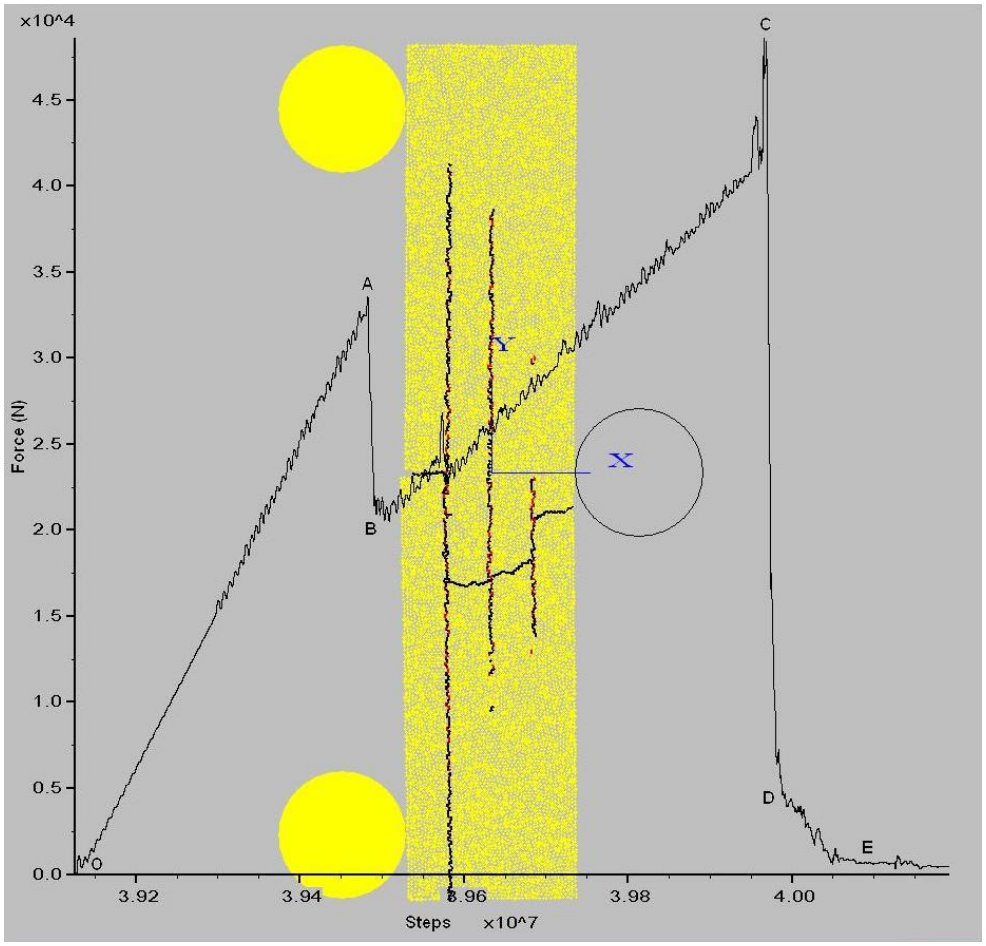
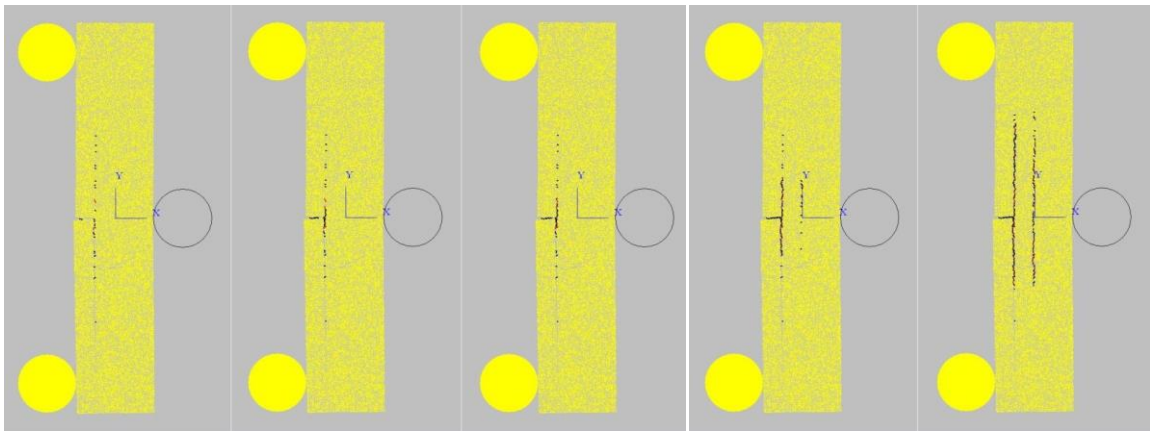


Figure 30: Force-steps diagram of notched sample with three weak interfaces.

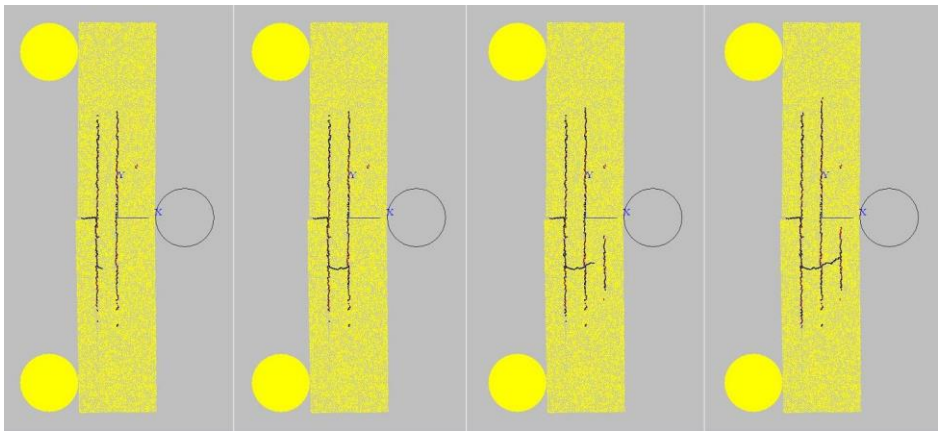
A-B: First drop of the loading curve, the crack initiated from the notch began to grow after certain amount of de-bonding occurred at the first interface. The resistance of crack growth at point A was 4.0 *MPa* $m^{1/2}$.

B-C: De-lamination continued at the first interface and started at the second interface till the force achieved a higher limit than in the stage A-B.

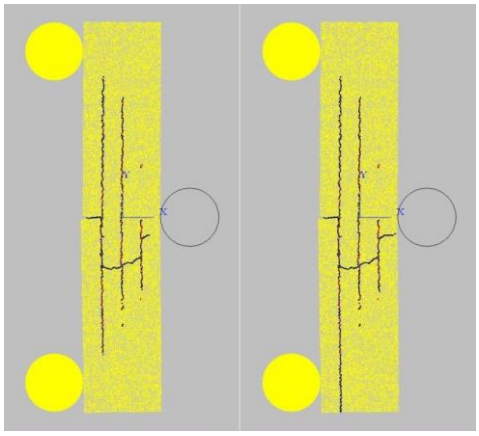
C-D: Second drop of the loading curve. Crack deflected from the first interface grown through the second interface (has not been arrested) till it met the third interface and has been arrested. The resistance of crack growth at point C increased to 12.7 *MPa* $m^{1/2}$.



A-B B-C



C-D



D-E

Figure 31: Propagation of the crack in the laminate with three weak interfaces.

D-E: Significant de-lamination of the first interface occurred; meanwhile, the main crack has been deflected from the last interface and grown through the rest of the sample to end failure.

3.2.2.4 Four Interfaces

In Figure 32, the overview of the failed sample and force-steps diagram are presented [57]. Figure 33 and Figure 34 depicted the details about stages from A to F and from F to I, separately [57].

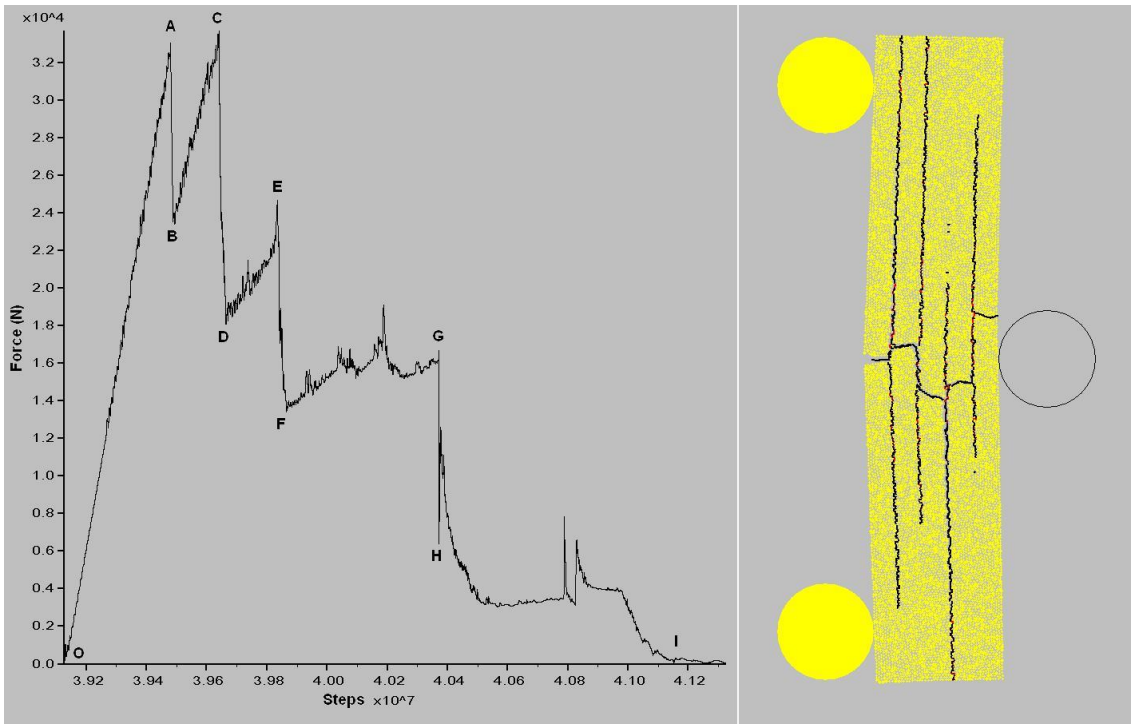


Figure 32: Force-steps diagram of notched sample with four weak interfaces [57].

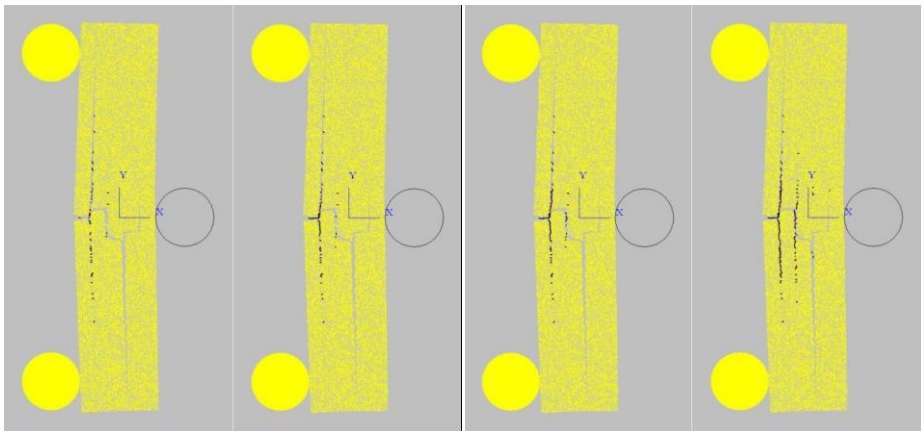
A-B: De-bonding mainly taken place at the first interface prior the crack growth. The resistance of crack growth at point A was 3.9 *MPa* $m^{1/2}$.

B-C: De-lamination at the first and second interfaces toughened the specimen, this led to reach the maximum load in the loading curve (load at C is higher than at A). De-bonding at the third interface started.

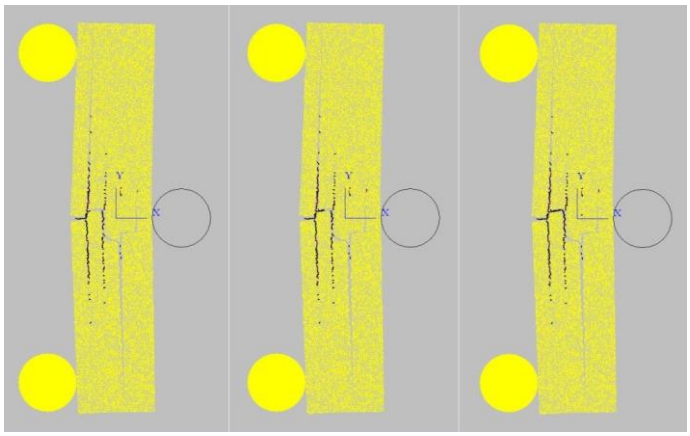
C-D: Crack deflected from the first interface extended and has been arrested at the second interface. The resistance of crack growth at point C was 7.7 *MPa* $m^{1/2}$.

D-E: De-lamination continued at the first and second interfaces.

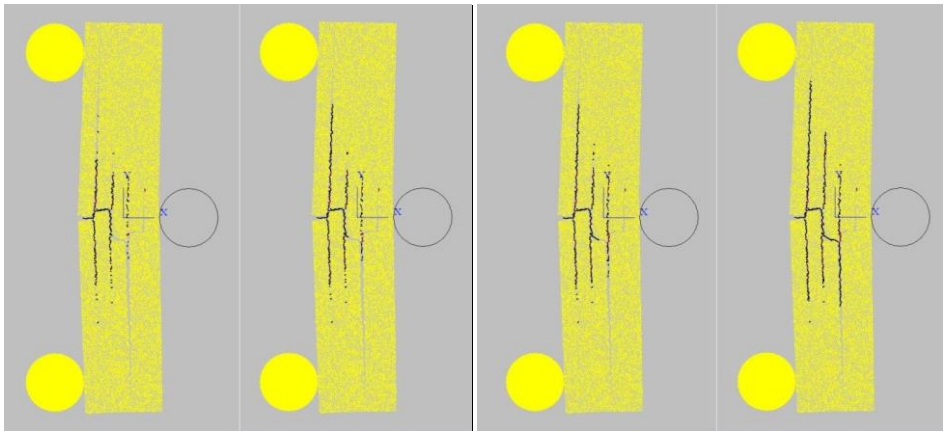
E-F: Deflected crack from the second interface grown and arrested at the third interface. The resistance of crack growth at point E was 9.4 *MPa* $m^{1/2}$.



A-B B-C



C-D



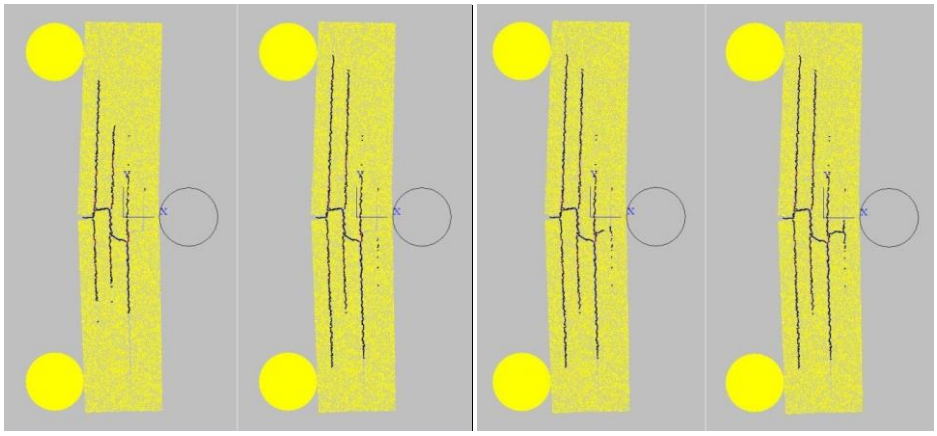
D-E E-F

Figure 33: Propagation of the crack in the laminate with four weak interfaces (stages from A to F) [57].

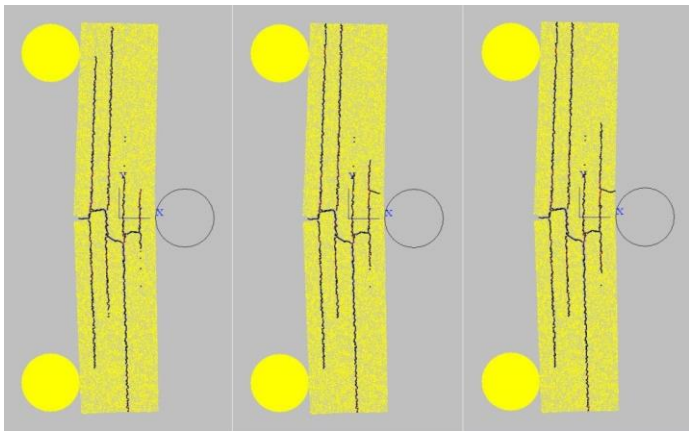
F-G: Significant de-lamination at the first three interfaces resulted the increase of loading force.

G-H: The third interface deflected the crack which grown to the last interface. The resistance of crack growth at point G increased to 12.3 *MPa* $m^{1/2}$.

H-I: Crack deflected from the fourth interface, accompanied with de-lamination at all interfaces, in which the first three interfaces have delaminated to the end of the sample.



F-G G-H



H-I

Figure 34: Propagation of the crack in the laminate with four weak interfaces (stages from F to I) [57].

3.2.2.5 Five Interfaces

Overview of the force-steps diagram of the laminate with five weak interfaces is shown in Figure 35. Details about the dynamic crack growth are illustrated in Figure 36 and Figure 37, respectively.

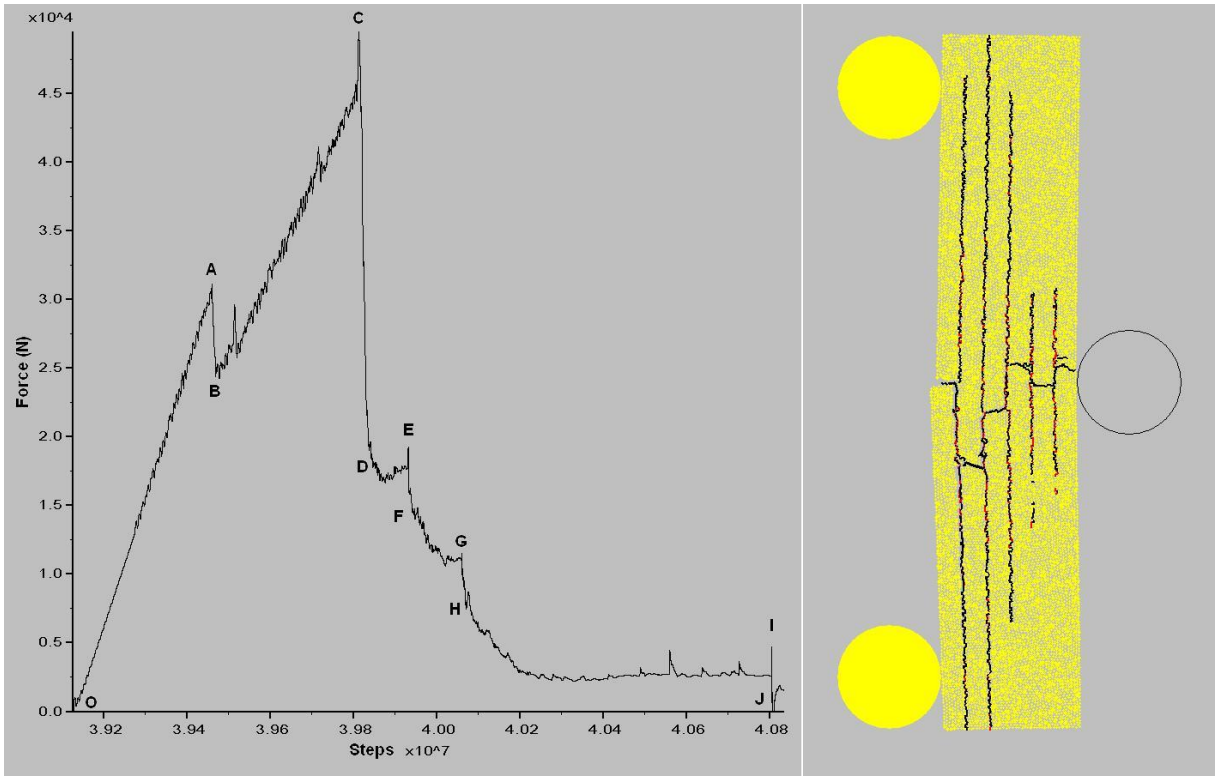


Figure 35: Force-steps diagram of notched sample with five weak interfaces.

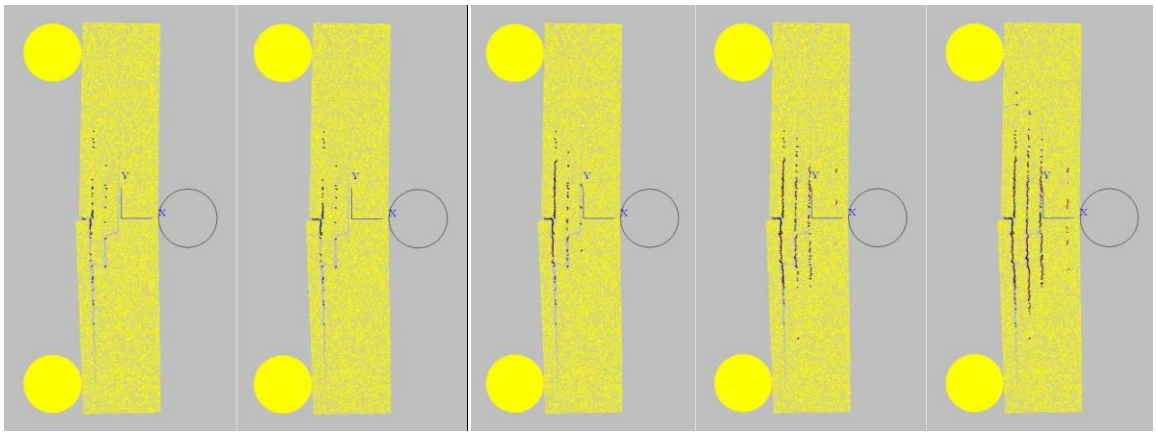
A-B: De-bonding mainly taken place at the first interface prior the crack growth. The resistance of crack growth at point A was 3.7 *MPa* $m^{1/2}$.

B-C: Intensive de-lamination at the first three interfaces toughened the specimen, which resulted the remarkable increase of the force in the force-steps diagram. De-bonding at the last interface started.

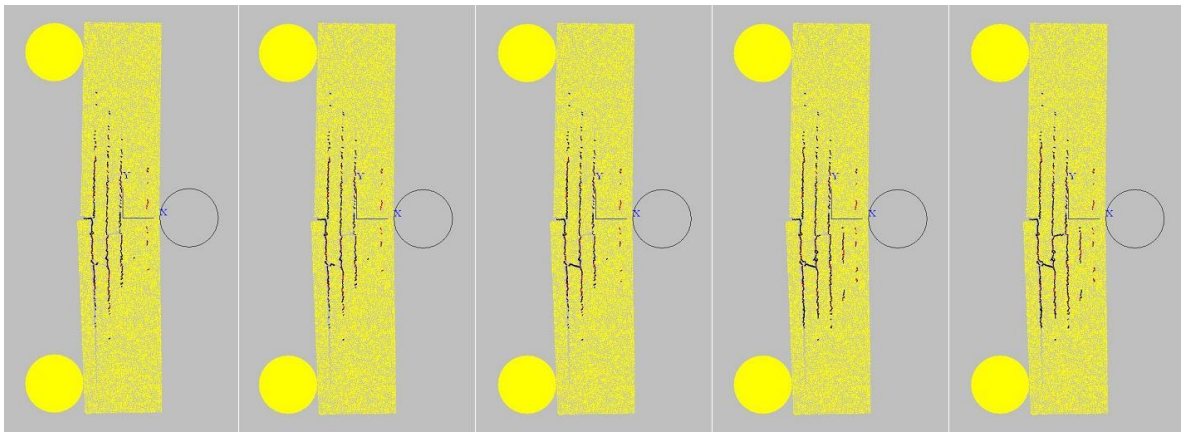
C-D: Crack deflected from the first interface extended and has been arrested at the second interface, from where the second deflection occurred sequentially. During the period of crack arrestment at the second interface, slight de-lamination at the first three interfaces was observed. The resistance of crack growth at point C was 9.5 *MPa* $m^{1/2}$.

D-E: Notable de-lamination at the first two interfaces led to the small load increase.

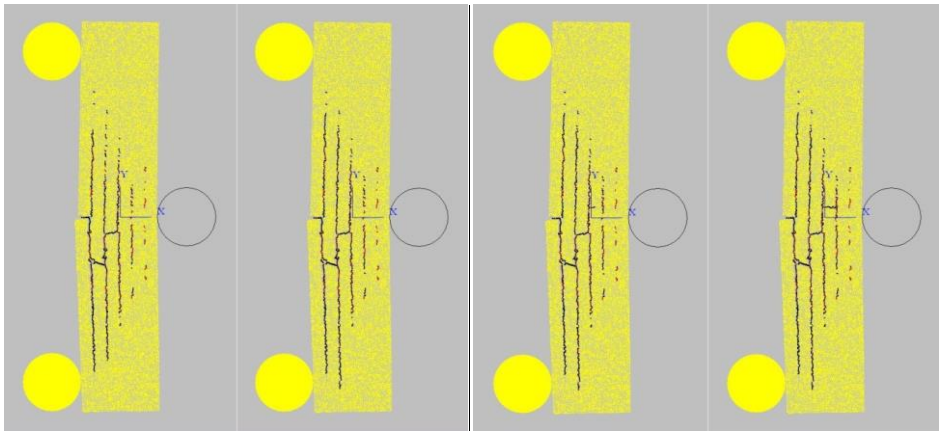
E-F: Deflected crack extended and has been arrested at the fourth interface. The resistance of crack growth at point E was 10.0 *MPa* $m^{1/2}$.



A-B B-C



C-D



D-E E-F

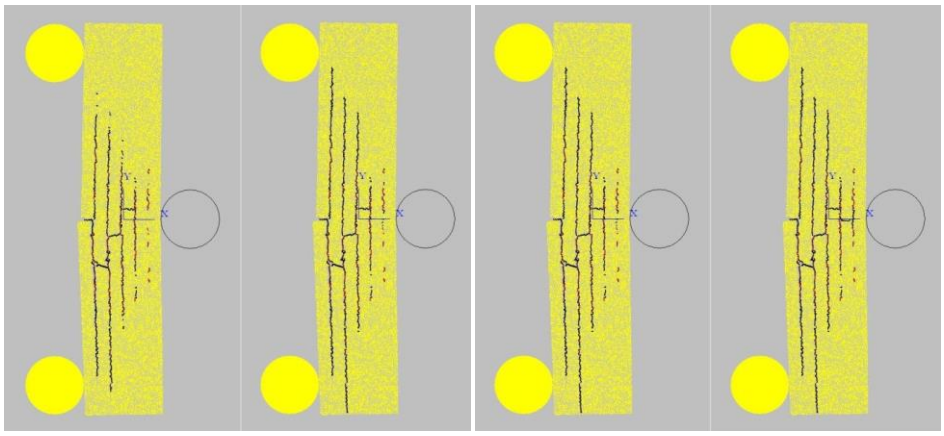
Figure 36: Propagation of the crack in the laminate with five weak interfaces (stages from A to F).

F-G: Significant de-lamination at the first three interfaces resulted the mild decrease of the loading force. The second interface has delaminated to the end of the sample (lower side).

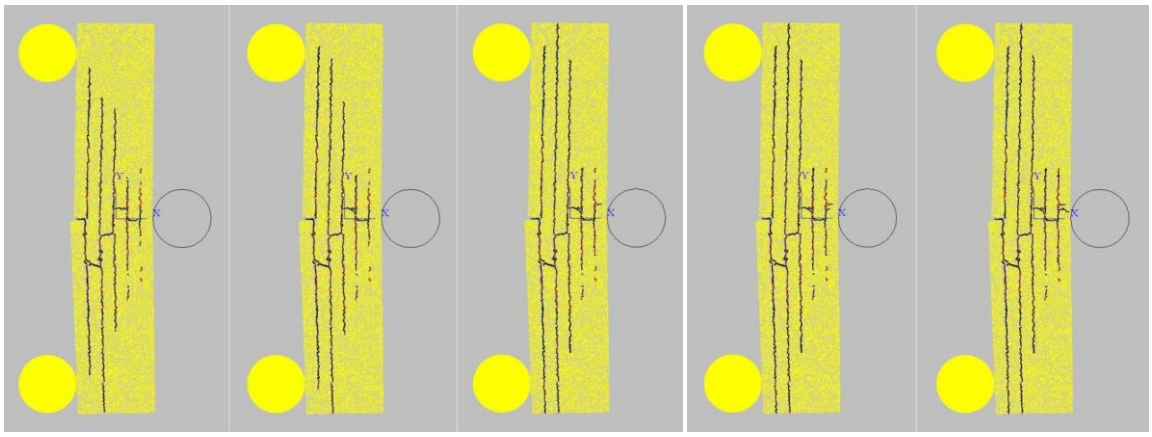
G-H: The fourth interface deflected the crack which grown to the last interface. The resistance of crack growth at point G increased to 11.2 *MPa* $m^{1/2}$.

H-I: Further intensive de-lamination at the first three interfaces assured the gradual decrease of the loading curve. The first two interfaces delaminated to the end of the sample.

I-J: Crack deflected from the fifth interface extended the whole thickness of the sample and the sample failed. The resistance of crack growth at point I was 9.0 *MPa* $m^{1/2}$.



F-G G-H



H-I I-J

Figure 37: Propagation of the crack in the laminate with five weak interfaces (stages from F to J).

3.2.2.6 Six Interfaces

Overview of the force-steps diagram of the laminate with six weak interfaces is shown in Figure 38. Details about the dynamic crack growth are illustrated in Figure 39 and Figure 40.

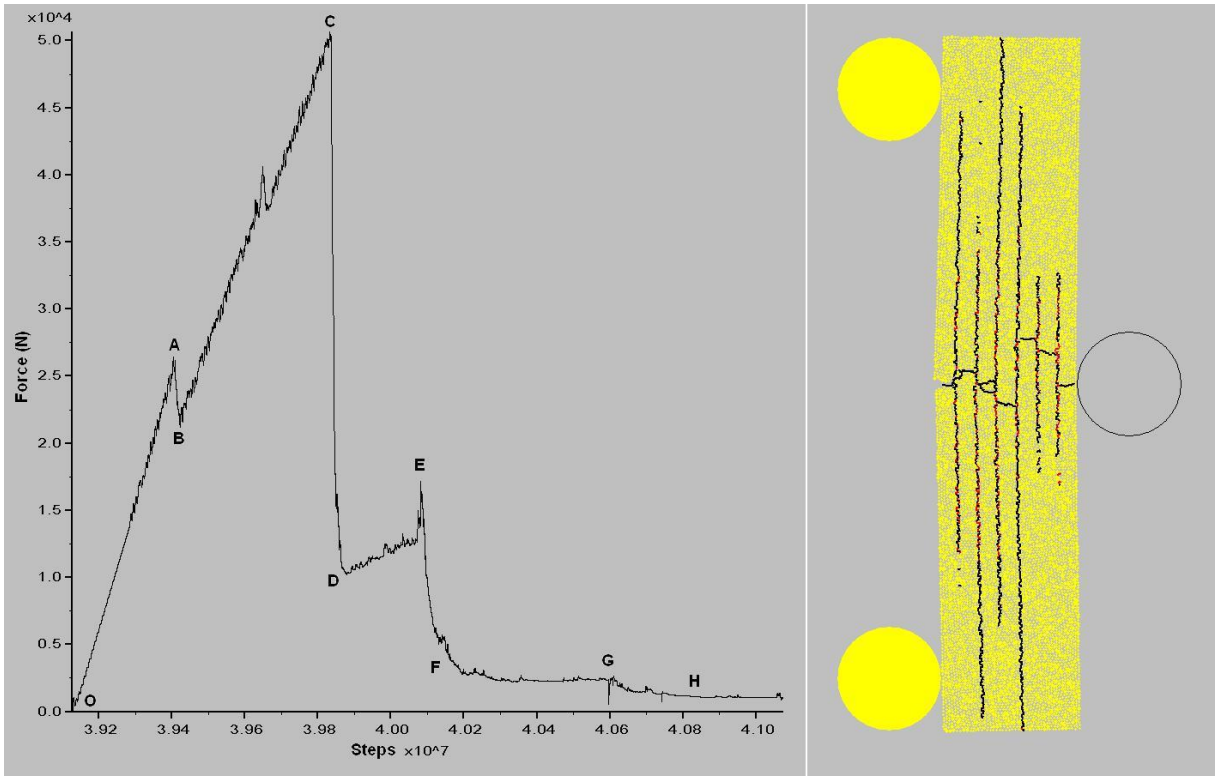


Figure 38: Force-steps diagram of notched sample with six weak interfaces.

A-B: De-bonding at the first and second interfaces occurred prior the crack growth. The resistance of crack growth at point A was 3.1 *MPa* $m^{1/2}$.

B-C: Significant de-lamination at the first four interfaces toughened the specimen, which resulted in a strong increase of the loading force. De-bonding at the last interface started.

C-D: After deflection from the first interface the crack extended to the second interface, where the second deflection occurred successively. Slight de-lamination at first two interfaces taken place before the crack has been deflected from the third interface. Crack grown further to the fourth interface. At the end of this stage, a new crack initiated from the third interface extended in the negative x-direction to the second interface. The resistance of crack growth at point C was 9.7 *MPa* $m^{1/2}$.

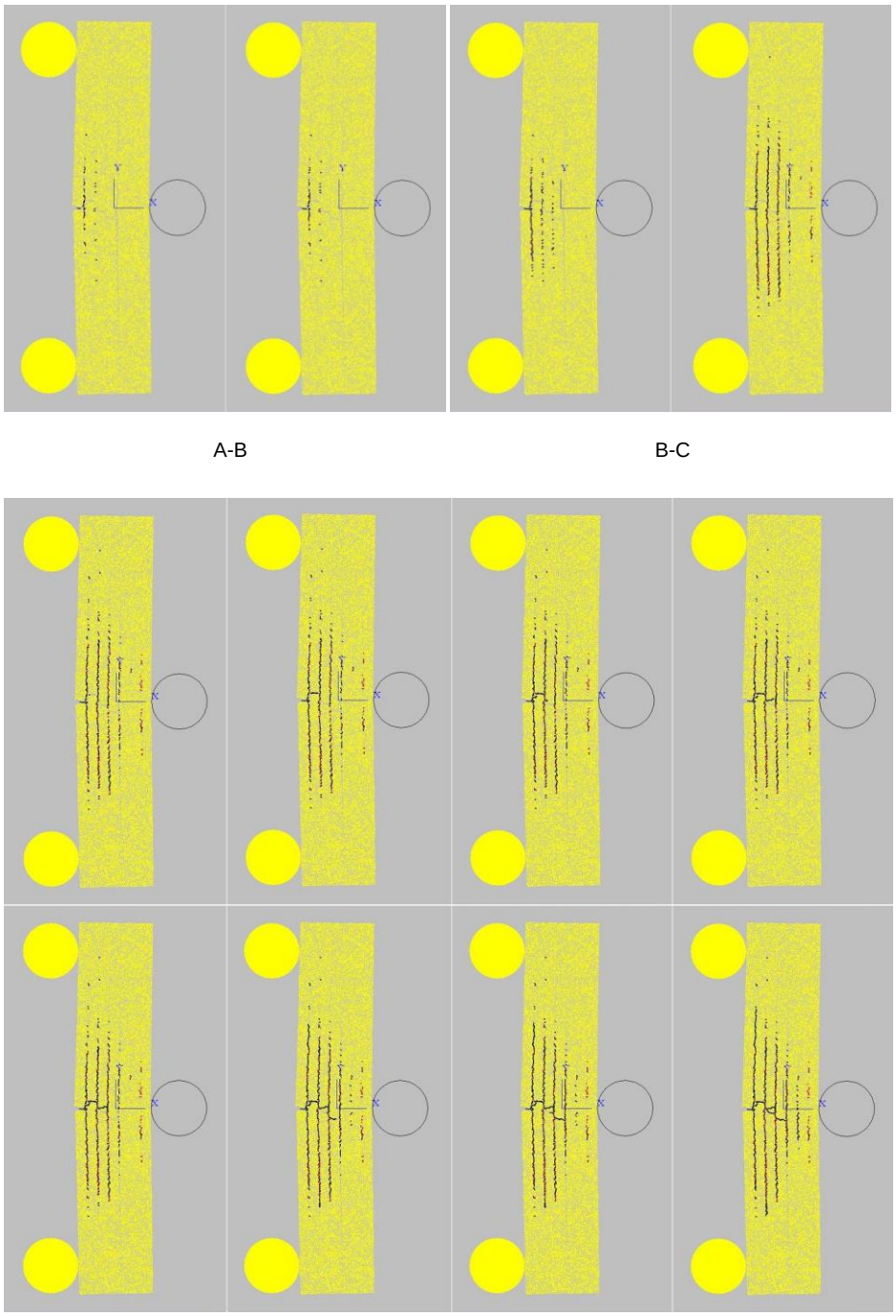


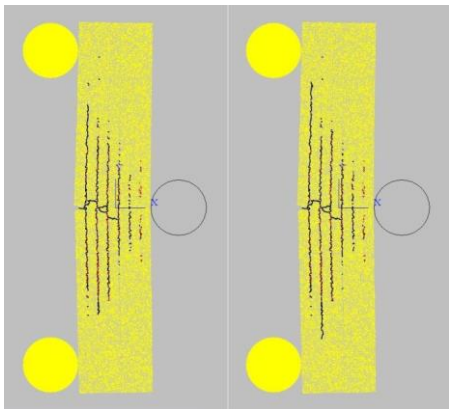
Figure 39: Propagation of the crack in the laminate with six weak interfaces (stages from A to D).

D-E: Intensive de-lamination at the first three interfaces led to the mild load increse.

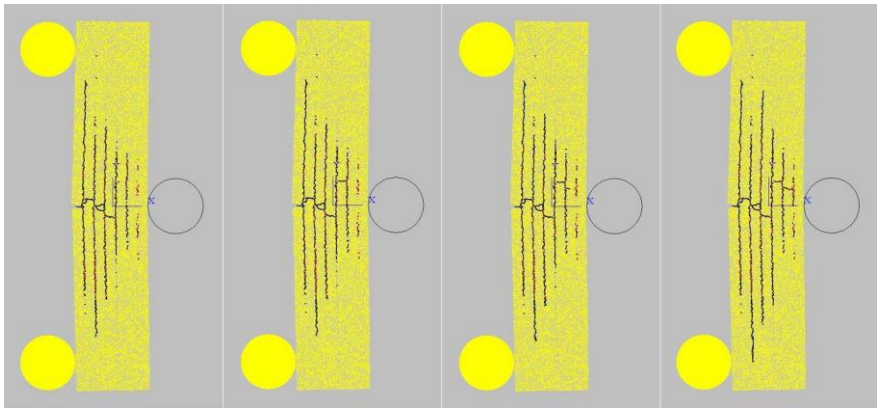
E-F: Crack deflected both at the fourth and fifth interfaces. The drop of the loading curve were gradually due to the notable de-lamination at the second, third and fourth interfaces. The resistance of crack growth at point E increased to 11.6 $MPa\ m^{1/2}$.

F-G: The second, third and fourth interfaces have delaminated to the sample's end.

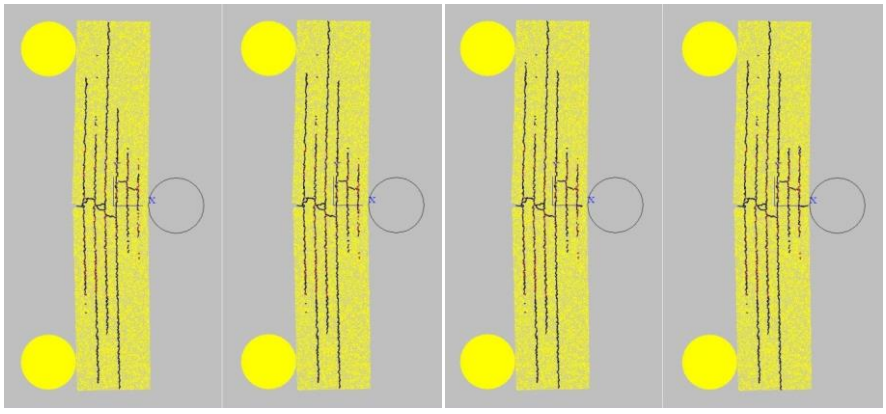
G-H: The crack has been deflected and extended through the thickness of the sample. The resistance of crack growth at point G decreased to 5.6 *MPa* $m^{1/2}$.



D-E



E-F



F-G G-H

Figure 40: Propagation of the crack in the laminate with six weak interfaces (stages from D to H).

3.2.2.7 Seven Interfaces

In Figure 41, overview of the force-steps diagram of the laminate with seven weak interfaces is shown. Details about the crack growth are illustrated in Figure 42, Figure 43 and Figure 44, respectively.

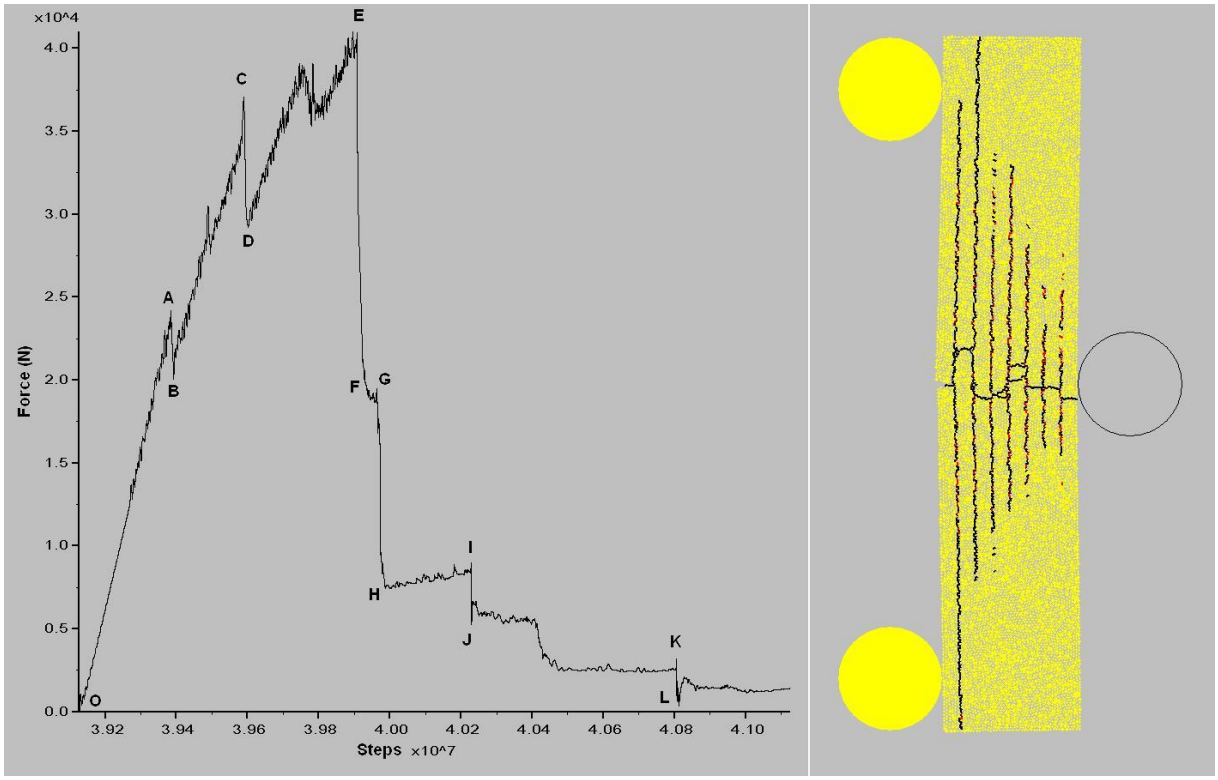


Figure 41: Force-steps diagram of notched sample with seven weak interfaces.

A-B: De-bonding occurred at the first interface prior the crack growth. The first drop of the loading curve. The resistance of crack growth at point A was 2.9 *MPa* $m^{1/2}$.

B-C: Significant de-lamination at the first three interfaces toughened the specimen, which resulted the increase of the load after the first drop. De-bonding started at the last interface.

C-D: Crack deflected from the first interface extended to the second interface and has been arrested there. The resistance of crack growth at point C was 6.6 *MPa* $m^{1/2}$.

D-E: Intensive de-lamination at the second, third and fourth interfaces. Notable de-laminations at fifth and seventh interfaces were also observed. These resulted the further increase of the loading force.

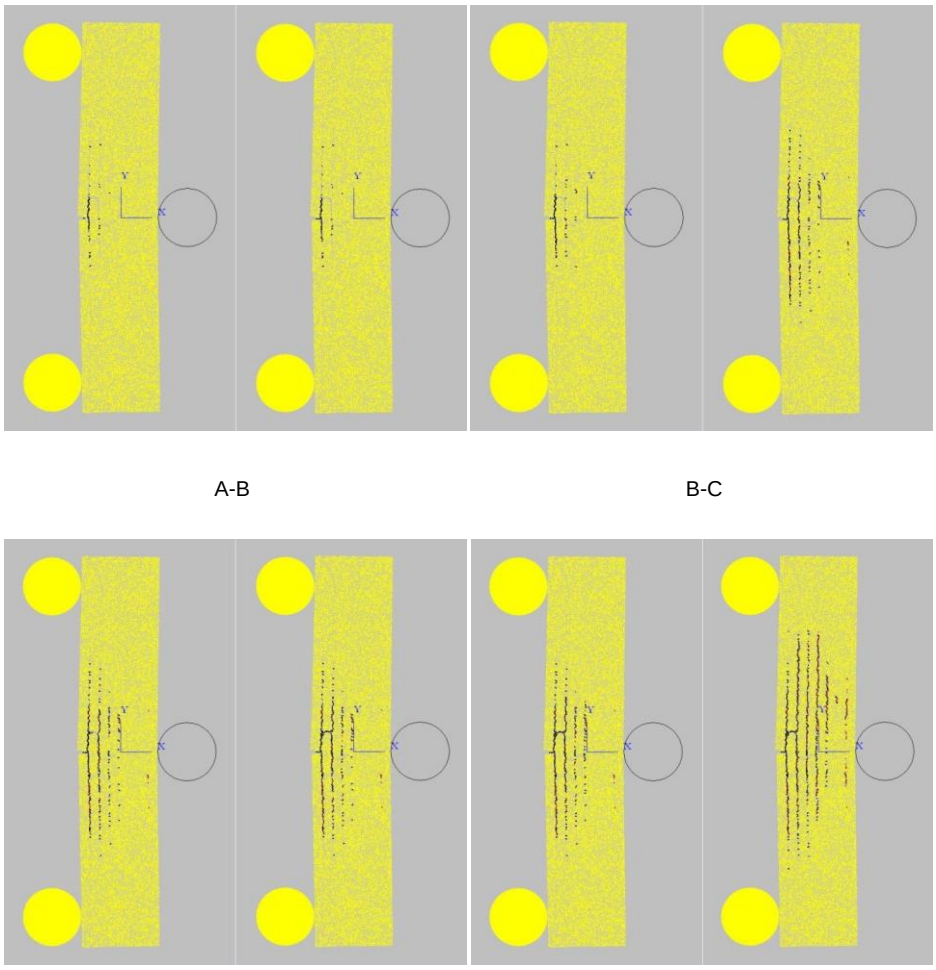
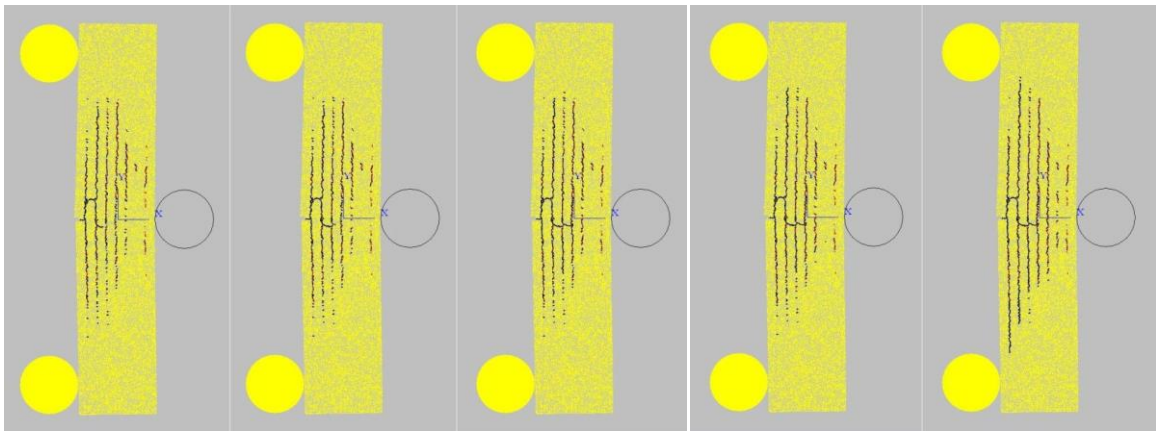


Figure 42: Propagation of the crack in the laminate with seven weak interfaces (stages from A to E).

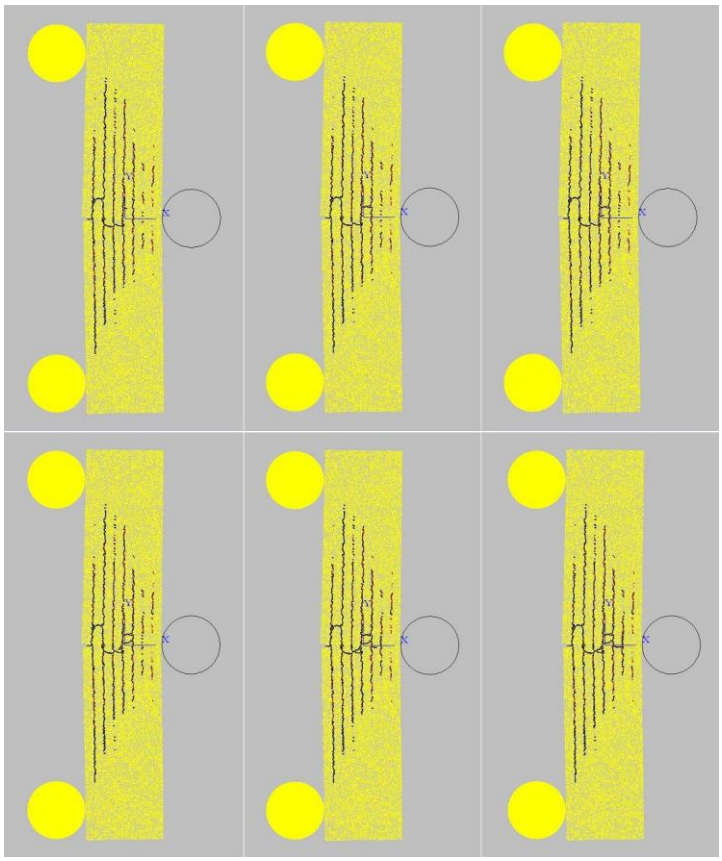
E-F: Crack deflected from the second interface extended through the third interface and has been arrested at the fourth interface. The resistance of crack growth at point E increased to 10.7 *MPa* $m^{1/2}$.

F-G: Notable de-lamination at the first two interfaces.

G-H: The crack has been first deflected from the fourth interface and arrested at the fifth interface. Then two new cracks were initiated at the fourth interface and extended in both positive and negative x-direction, ended at the third and fifth interfaces, respectively. Moreover, the main crack has been deflected once more from the fifth interface and extended to the sixth interface. The resistance of crack growth at point G was 10.0 *MPa* $m^{1/2}$.



E-F F-G



G-H

Figure 43: Propagation of the crack in the laminate with seven weak interfaces (stages from E to H).

H-I: De-lamination at the first interface.

I-J: Crack growths through the sixth interface to the last interface. The resistance of crack growth at point I increased to 12.6 *MPa* $m^{1/2}$.

J-K: Remarkable de-lamination at the first two interfaces corresponding to the gradual decrease of the loading force.

K-L: Deflected crack growth through the thickness of the sample, ultimate failure of the sample.

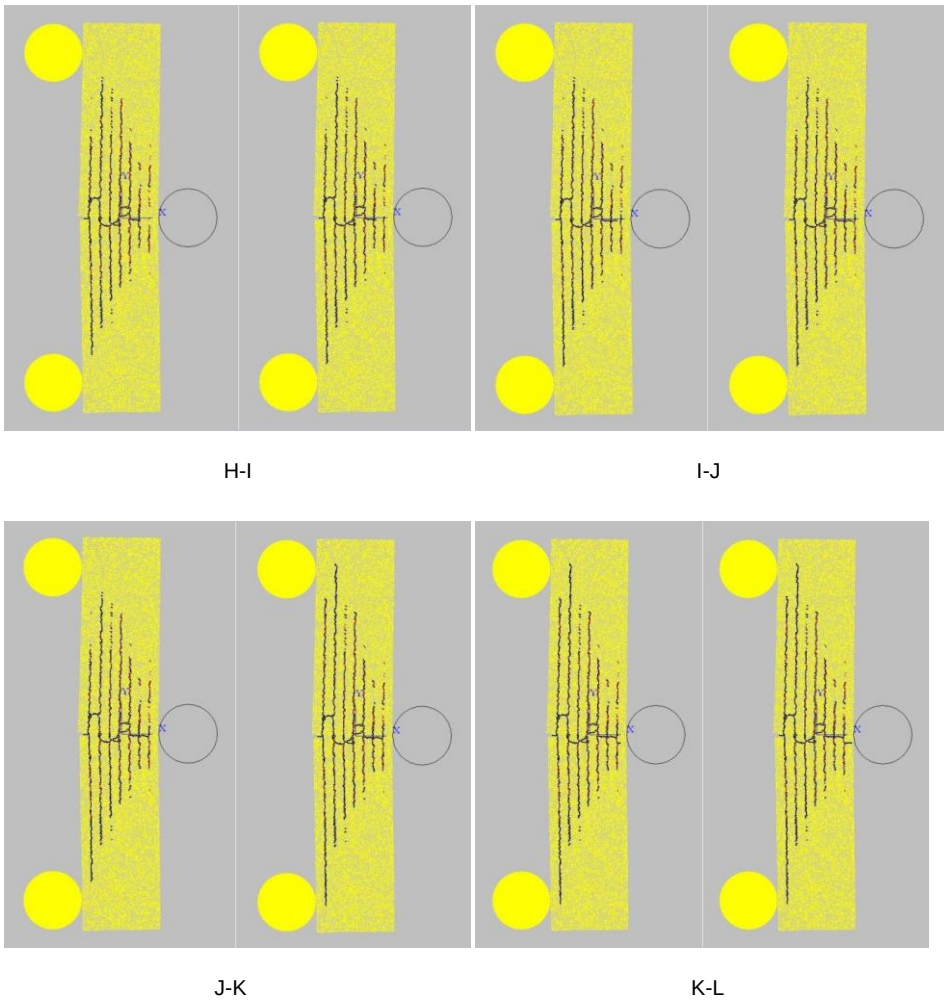


Figure 44: Propagation of the crack in the laminate with seven weak interfaces (stages from H to L).

3.2.2.8 Eight Interfaces

In Figure 45, overview of the force-steps diagram of the laminate with eight weak interfaces is shown. Details about the crack growth are illustrated in Figure 46, Figure 47 and Figure 48, respectively.

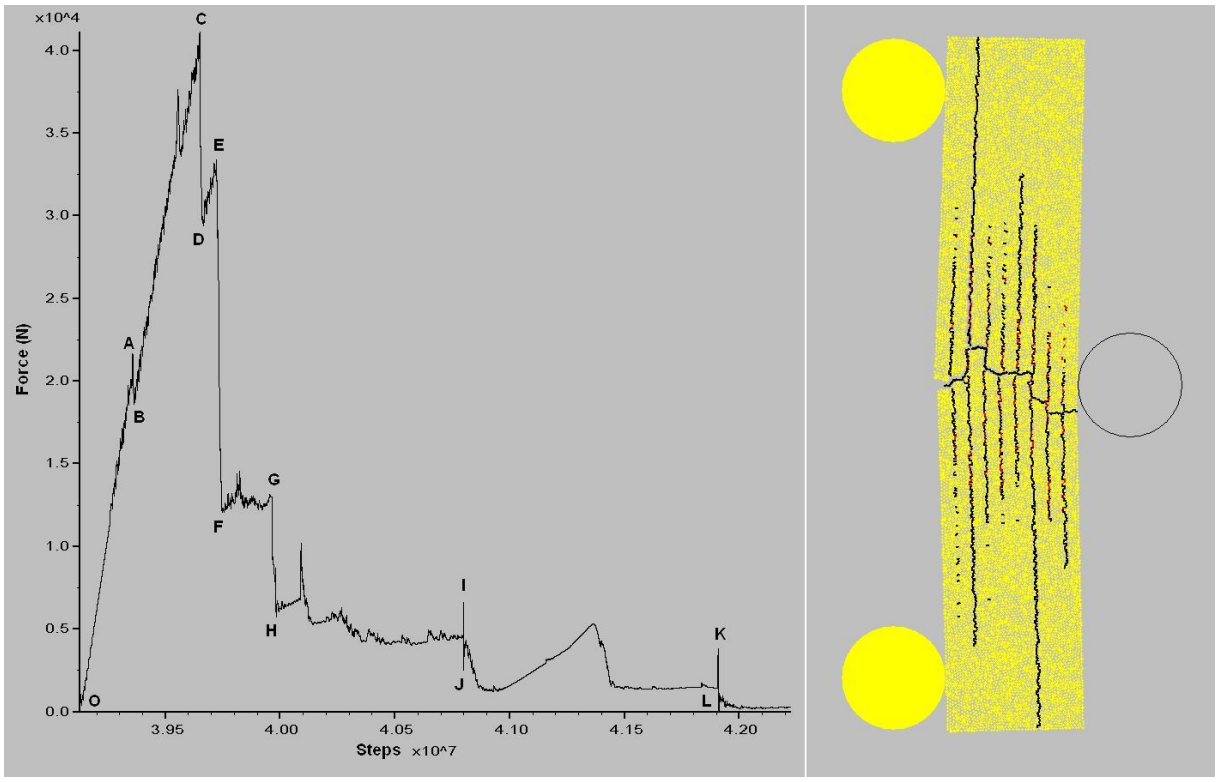
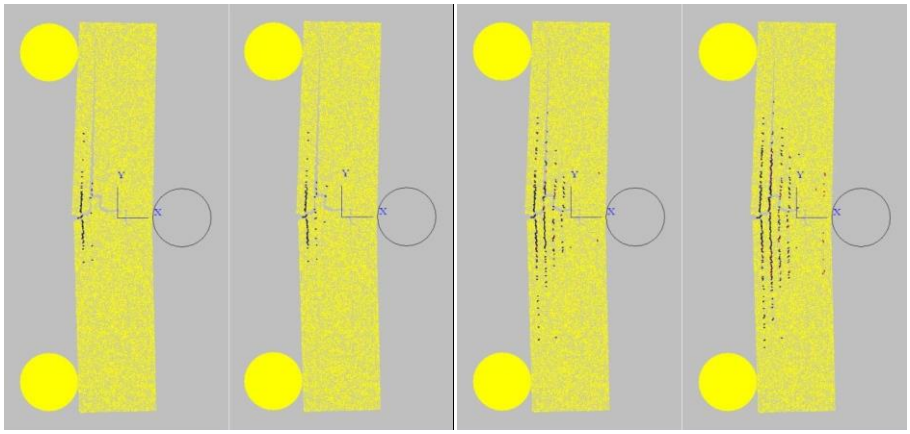


Figure 45: Force-steps diagram of notched sample with eight weak interfaces.



A-B B-C

Figure 46: Propagation of the crack in the laminate with eight weak interfaces (stage A to C).

A-B: De-bonding occurred at the first interface prior to the crack growth which resulted in the first drop of the loading force. The resistance of crack growth at point A was 2.6 *MPa* $m^{1/2}$.

B to C: Significant de-lamination at the first four interfaces toughened the specimen, which resulted the remarkable increase of the load after the first drop of the loading curve. De-bonding at the last interface started.

C to D: The crack deflected from the first interface extended to the second interface and has been arrested there. The resistance of crack growth at point C was 7.0 *MPa* $m^{1/2}$.

D to E: De-lamination occurred at the third and fourth interfaces and led to the increase of the loading force.

E to F: The crack deflected from the second and third interfaces has grown through the fourth interface and has been arrested at the fifth interface. The crack resistance at point E was 8.1 *MPa* $m^{1/2}$.

F to G: Significant de-lamination at the second and third interfaces. Notable de-lamination at the fourth, fifth and sixth interfaces were also observed. This prevented further extension of the crack which has been arrested in the stage E-F.

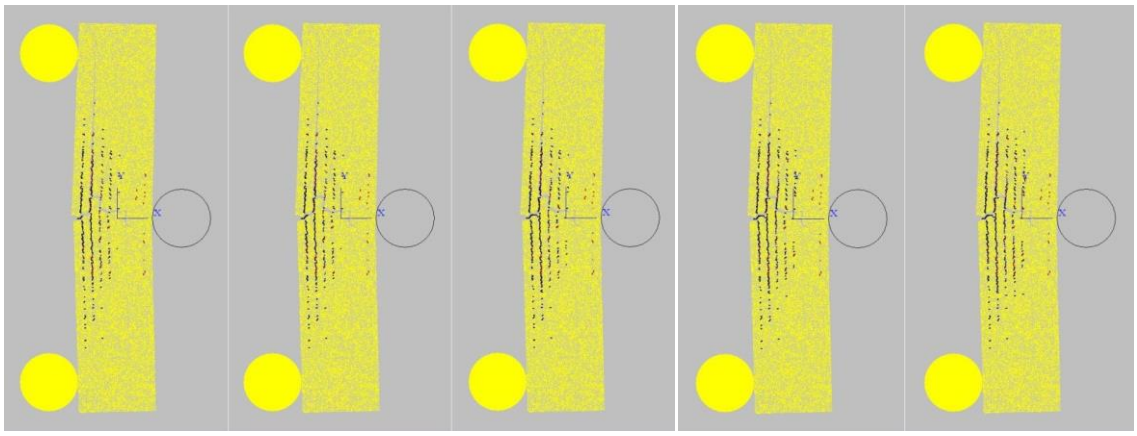
G to H: The crack grown through the fifth interface and has been arrested at the sixth interface. Then the crack has been deflected and extended to the seventh interface. The resistance of crack growth at point G was 8.2 *MPa* $m^{1/2}$.

H to I: Intensive de-lamination at the second, fifth, sixth and seventh interfaces which led to the constant evolution of the loading force. The second interface delaminated to the end of the sample.

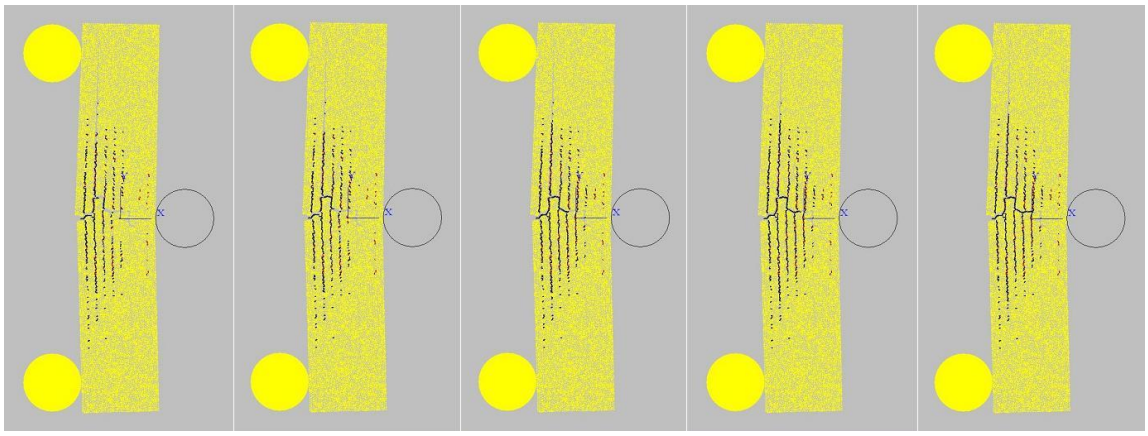
I to J: The crack deflected from the seventh interface has been arrested at the last interface. The resistance of crack growth at point I increased to 10.2 *MPa* $m^{1/2}$.

J to K: Notable de-lamination took place at the sixth, seventh and eighth interfaces.

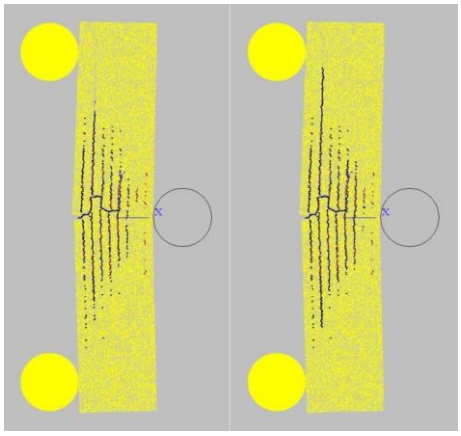
K to L: Further de-lamination at the eighth interface. The crack deflected from the last interface extended through the thickness of the sample.



C-D D-E

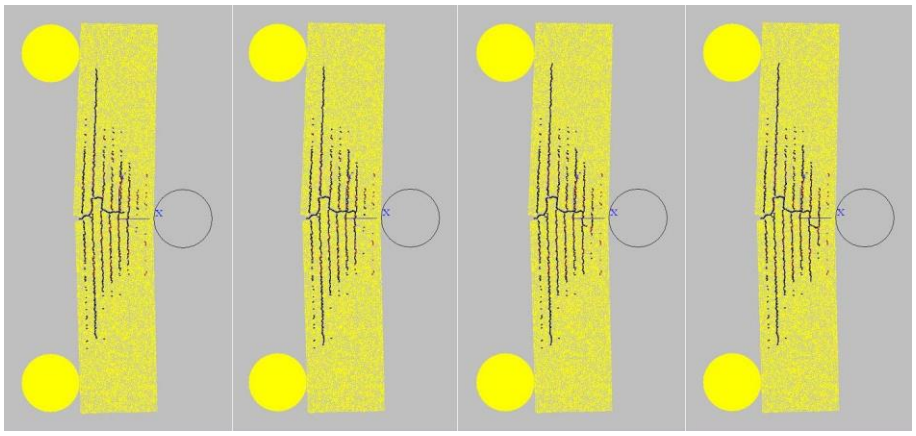


E-F

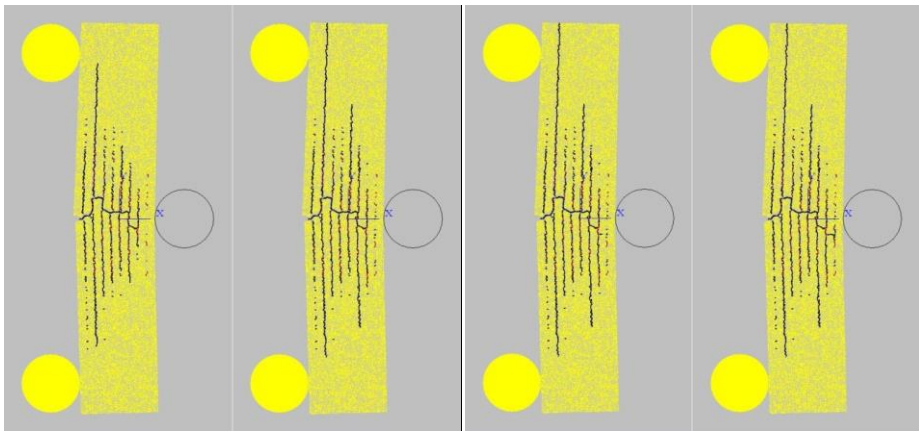


F-G

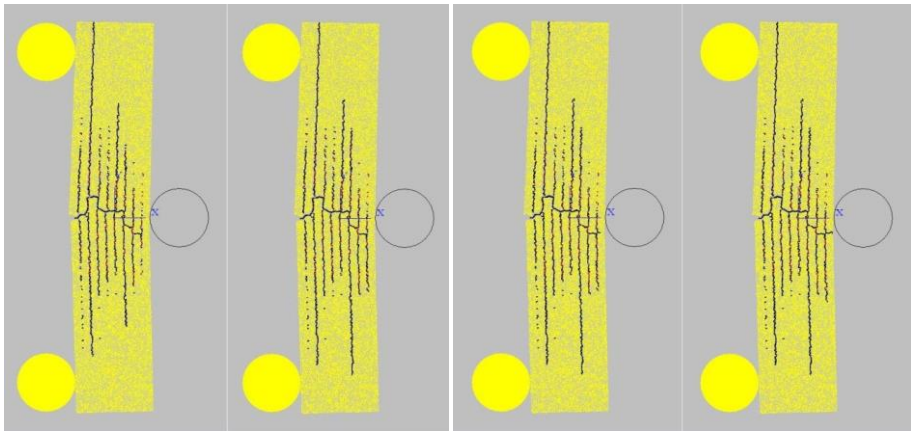
Figure 47: Propagation of the crack in the laminate with eight weak interfaces (stages from C to G).



G-H



H-I I-J



J-K K-L

Figure 48: Propagation of the crack in the laminate with eight weak interfaces (stages from G to L).

3.2.2.9 Nine Interfaces

In Figure 49, overview of the force-steps diagram of the laminate with nine weak interfaces is shown. Details about the crack growth are illustrated in Figure 50, Figure 51 and Figure 52, respectively.

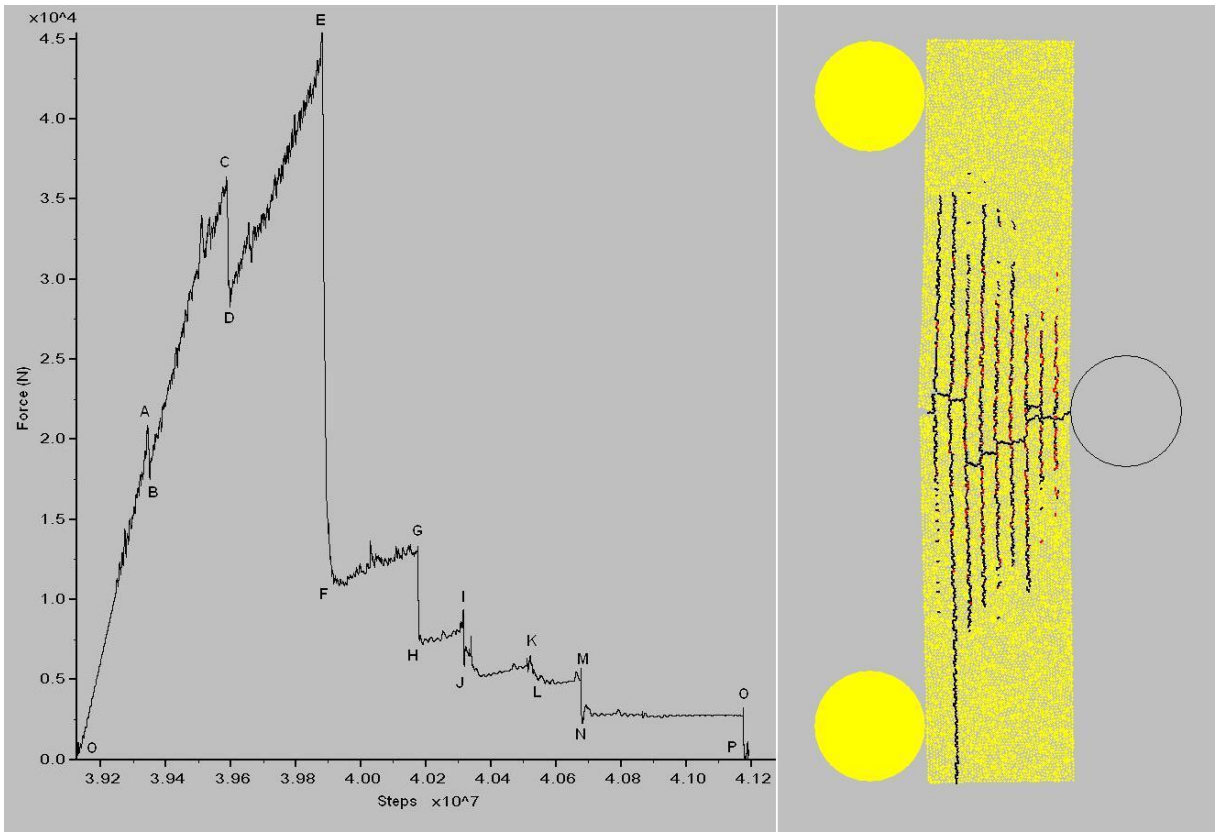
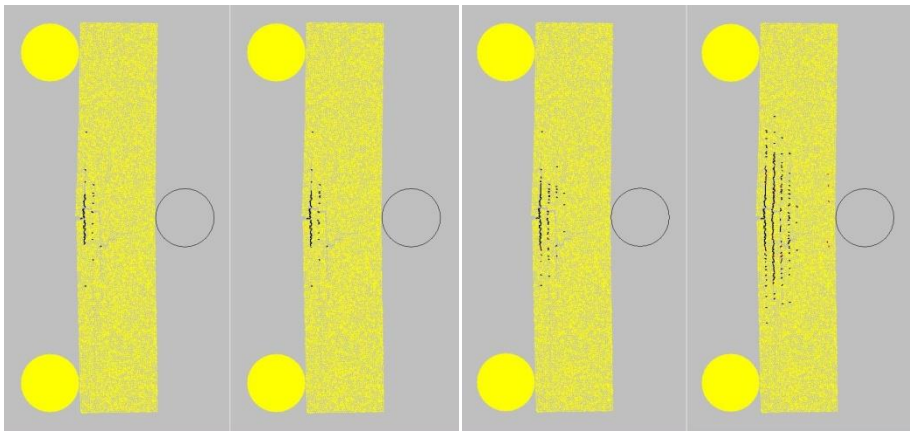


Figure 49: Force-steps diagram of notched sample with nine weak interfaces.

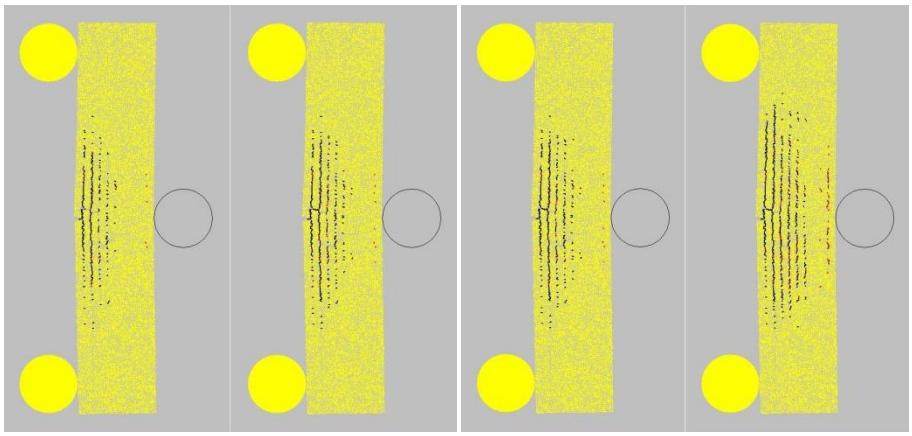
A-B: De-bonding occurred at the first interface prior the crack growth. The first drop of the loading force. The crack initiated at the notch and extended to the first weak interface. The resistance of crack growth at point A was 2.5 *MPa* $m^{1/2}$.

B-C: Significant de-lamination at the first four interfaces toughened the specimen, which resulted the remarkable increase of the load after the first drop of the loading curve. De-bonding at the last interface started.

C-D: The crack deflected from the first interface extended to the second interface and has been arrested there. The resistance of crack growth at point C was 5.9 *MPa* $m^{1/2}$.



A-B B-C



C-D D-E



E-F

Figure 50: Propagation of the crack in the laminate with nine weak interfaces (stages from A to F).

D-E: De-lamination occurred at the first four interfaces and led to the increase of the load.

E-F: The crack has been deflected at the second, third, fourth and fifth interfaces, sequentially. The crack has been arrested at the sixth interface. This stage corresponded to the significant drop of the loading curve. The resistance of crack growth at point E increased to 10.3 $MPa\ m^{1/2}$.

F-G: Significant de-lamination at the interfaces which deflected the crack in the stage E-F.

G-H: The crack has grown through the sixth interface and has been arrested at the seventh interface. The resistance of crack growth at point G was 10.0 $MPa\ m^{1/2}$.

H-I: De-lamination at the last three interfaces which led to the nearly constant evolution of the loading force.

I-J: The crack has been deflected from the seventh interface and has been arrested at the eighth interface. The resistance of crack growth at point I increased to 10.5 $MPa\ m^{1/2}$.

J-K: De-lamination has taken place at the second interface.

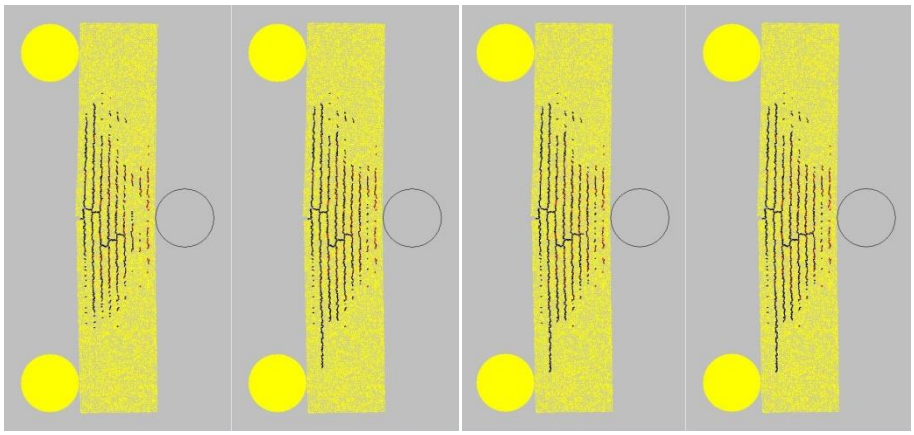
K-L: The crack has been deflected at the eighth interface and extended to the last interface.

L-M: Further de-lamination at the second interface.

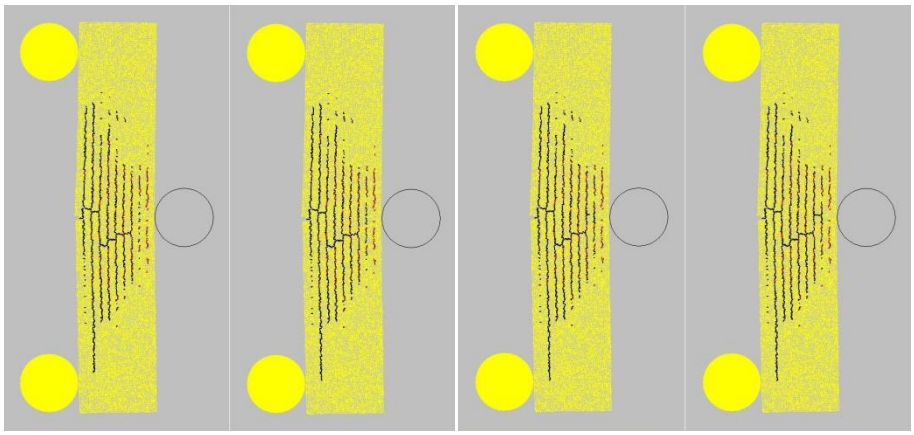
M-N: A second crack initiated at the seventh interface and extended to the eighth interface.

N-O: De-lamination at the second interface reached the end of the sample.

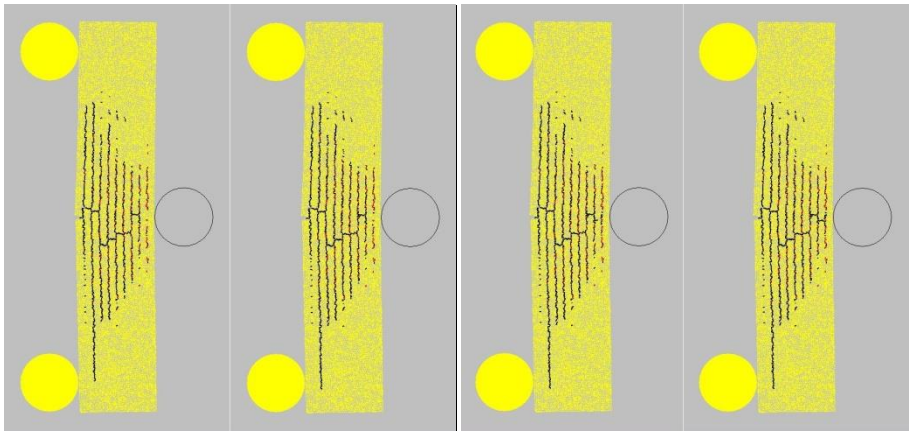
O-P: The last extension of the crack and the sample failed.



F-G G-H



H-I I-J



J-K K-L

Figure 51: Propagation of the crack in the laminate with nine weak interfaces (stages from F to L).

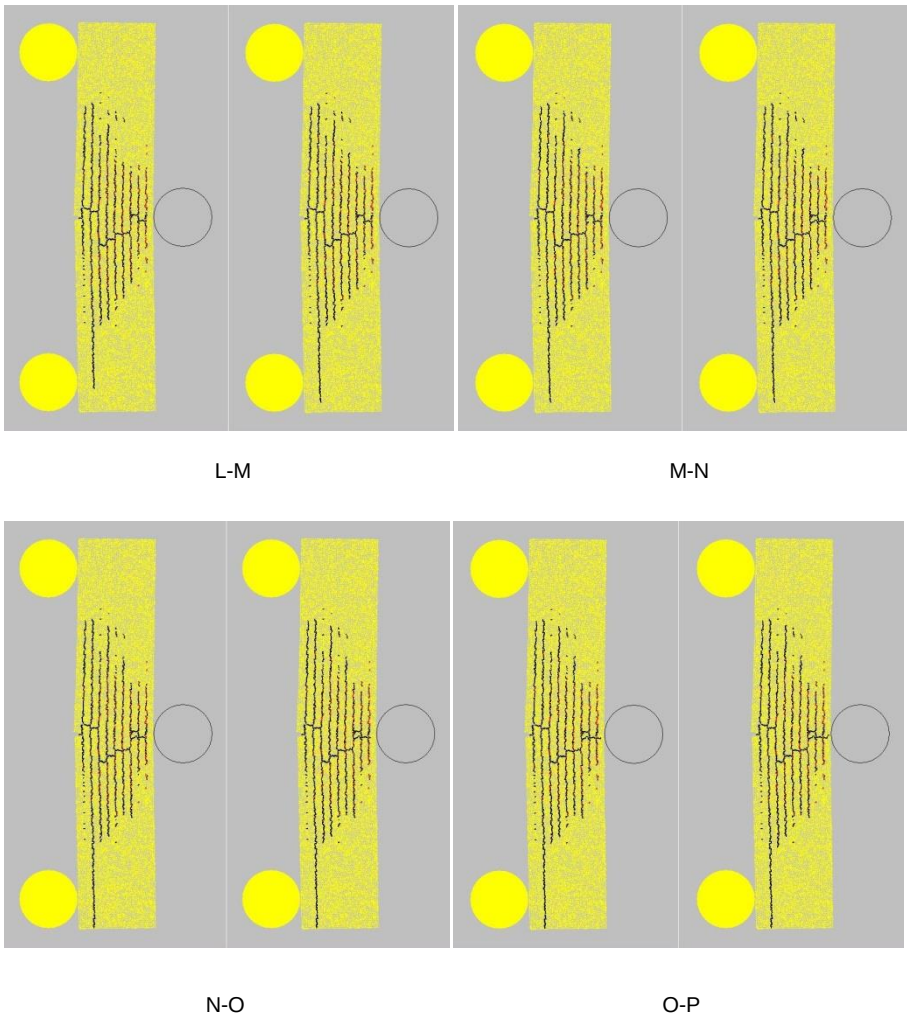


Figure 52: Propagation of the crack in the laminate with nine weak interfaces (stage from L to P).

3.3 R-Curve Behavior of SiC-C Laminates

R-curve behavior was found in the laminates with seven different weak bond strengths (30 *MPa*, 70 *MPa*, 100 *MPa*, 200 *MPa*, 230 *MPa*, 250 *MPa* and 300 *MPa*), however, the R-curve behavior of the laminates with weak bond strength of 100 *MPa* are chosen to present in this section [57]. Based on the results of the dynamic modeling of the crack propagation presented in 3.2.2, the resistance of crack growth at characteristic points for all the laminates are calculated according to Eq. (30) [63] and summarized in Table 7. The evolution of the crack length during the three-point-bending test is obtained from figures in which the stages of the crack propagation are captured. The crack length parallel to the interface, *i.e.* the length that the crack travelled along the interface was not counted as the crack length and was, thus not used to be inserted into the Eq. (30). In Figure 53, the resistance of crack growth is plotted against the crack length. For the convenience, samples are named by the

number of weak interfaces, as 0# for the bulk material, 9# for the sample which contains nine weak interfaces. The maximum value of the resistance was evaluated as 14.9 *MPa* $m^{1/2}$ in the 1# sample, whereas the maximum increase of the resistance was found to be 4.3-fold in the 7# sample.

Table 7: Resistance of the crack growth for all laminates (bond strength of 100 *MPa*) at characteristic points (the unit of the resistance is *MPa* $m^{1/2}$, "-" means no data is available).

Resis. at / Sample	A	C	E	G	I
1#	3.9	14.9	-	-	-
2#	4.0	10.7	-	-	-
3#	4.0	12.7	-	-	-
4#	3.9	7.7	9.4	12.3	-
5#	3.7	9.5	10.0	11.2	9.0
6#	3.1	9.7	11.6	5.6	-
7#	2.9	6.6	10.7	10.0	12.6
8#	2.6	7.0	8.1	8.2	10.2
9#	2.5	5.9	10.3	10.0	10.5

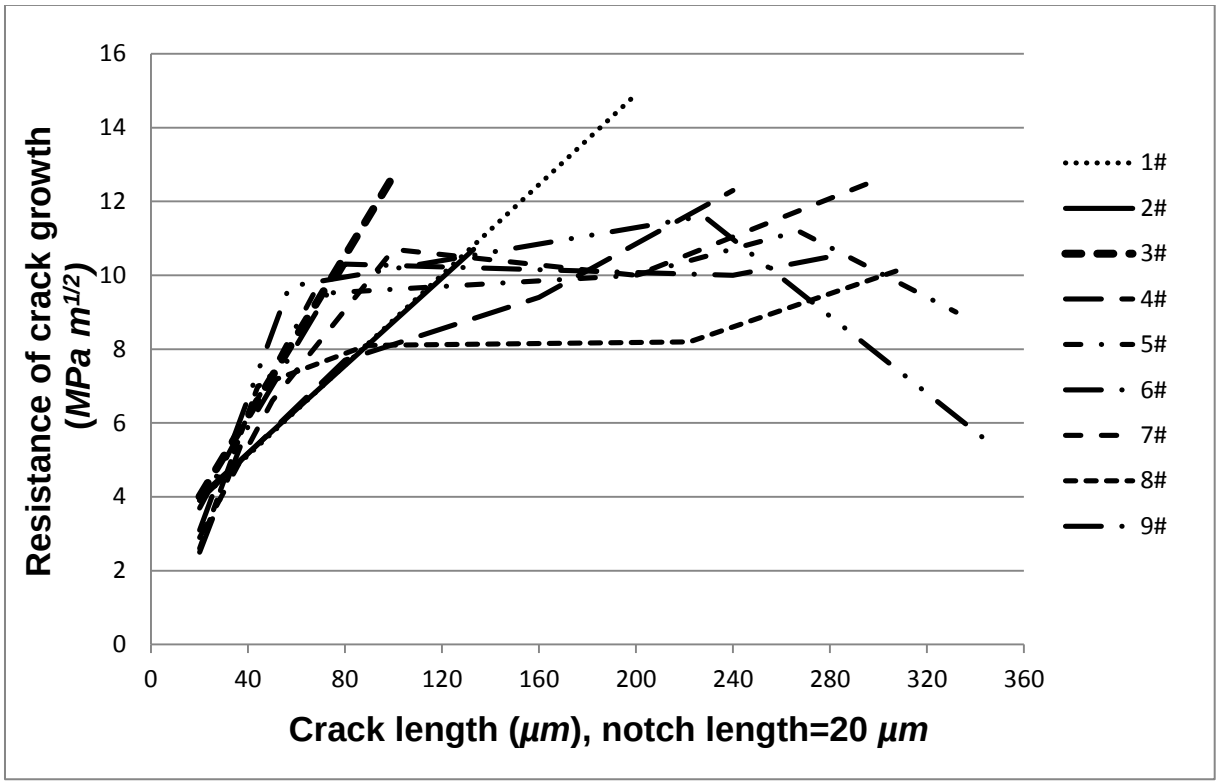


Figure 53: Plot of the resistance of crack growth against the crack length in all SiC-C laminates (weak bond strength of 100 *MPa*).

The distribution of the introduced weak interfaces in the laminate is axial-symmetric along the direction of the length of the laminate. In order to investigate the influence of the number of introduced weak interfaces on the resistance of crack growth, the resistance of crack growth at point A was plotted against the thickness ratio of the lamella and the laminate ($t_{lamella}/t_{laminate}$) in Fig.54. As the resistance of crack growth approaches to 4.4 *MPa* $m^{1/2}$ which is the fracture toughness of the monolithic SiC material, the $t_{lamella}/t_{laminate}$ increases to 0.5 which is the maximum value of $t_{lamella}/t_{laminate}$ for the laminates (corresponded to the laminate with one introduced weak interface). The difference of the resistance between the laminates and the monolithic SiC decreases as the weak bond strength increases.

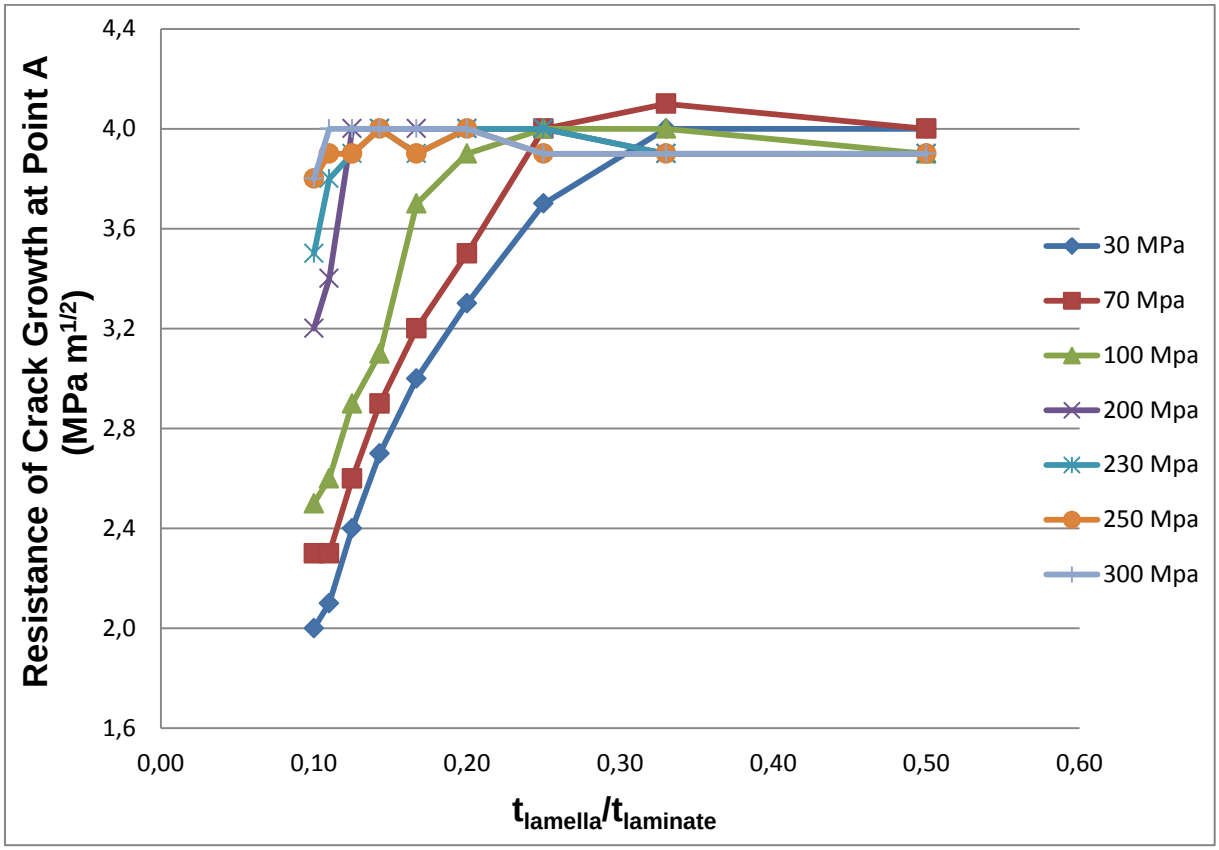


Figure 54: Plot of the resistance of crack growth at point A against the thickness ratio $t_{lamella}/t_{laminate}$ in all SiC-C laminates.

3.4 Bending Strength of SiC-C Laminates

According to Eq. (29) [62], the bending strength is related to the maximum load in the loading diagram. The laminates were in the same geometry and tested under the same condition, therefore the comparison of the bending strength were replaced by the maximum load. By varying the values of different weak bond strengths, the

maximum loads in each laminate were summarized in Table 8. In Fig.55, the normalized maximum load (normalized to the 0# sample) in laminates of seven different weak bond strengths were plotted against the number of weak interfaces. The curves in Fig.55 were shown a periodic pattern and the values of most of the curves were above 1.

Table 8: Maximum load in the laminates with seven different weak bond strengths.

Max. Load in (*N*) / Sample	300 *MPa*	250 *MPa*	230 *MPa*	200 *MPa*	100 *MPa*	70 *MPa*	30 *MPa*
1#	33250	33250	33250	33250	33250	33690	33760
2#	33240	33240	33730	33650	33970	34190	33710
3#	33250	46240	46580	50670	48620	46030	44440
4#	33340	35670	35640	34760	33720	32200	31110
5#	34990	37900	58970	58310	49500	48710	30820
6#	38470	55090	55350	51000	50700	49660	49980
7#	43840	43900	44320	44000	41020	39880	38550
8#	54420	59100	62020	62070	41160	39150	45980
9#	48980	52350	48280	46220	45420	40830	39950

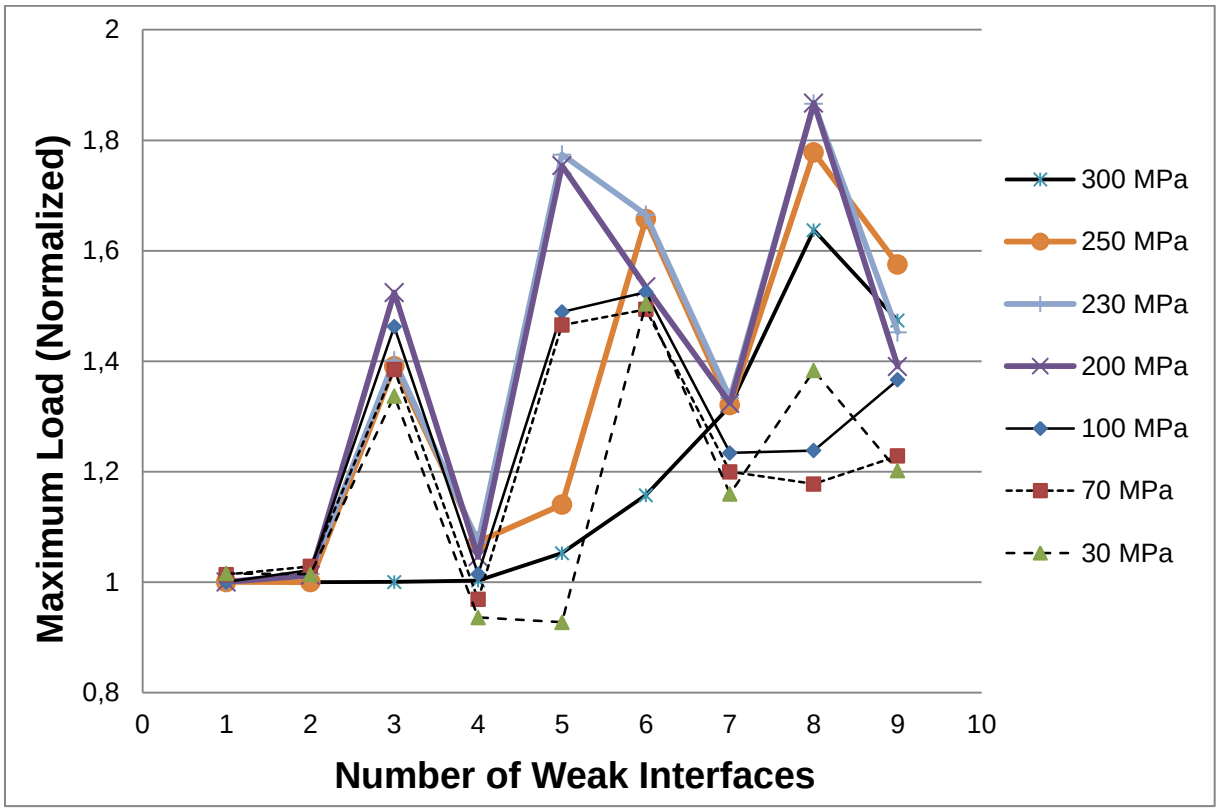


Figure 55: Normalized maximum load of all SiC-C laminates with seven different weak bond strengths.

3.5 Fracture Energy of SiC-C Laminates

For the brittle materials, the theoretical lower bound for the fracture energy is the energy of the new generated surfaces (2γ, γ is the surface energy) [1]. Since all the modeling was carried out in two dimensions, assume the SiC material and the weak interface has the same surface energy, then the length of the main crack (transversal crack propagated in SiC-lamella) and the deflected crack along the weak interfaces can be added and used to represent the apparent fracture energy. The relative change of the fracture energy (normalized to the 0# sample) instead of the absolute value of the apparent fracture energy was first compared in this section for the laminates with the weak bond strength of 100 *MPa*. In Figure 56 the diagram of the normalized fracture energy was presented for the SiC-C laminates with the weak bond strength of 100 *MPa*. The normalized fracture energy increases monotonically from 6-fold to 20-fold in the 1# and 6# sample, respectively. After a slightly decreasing, the maximum value of the 22-fold was achieved in the 9# sample.

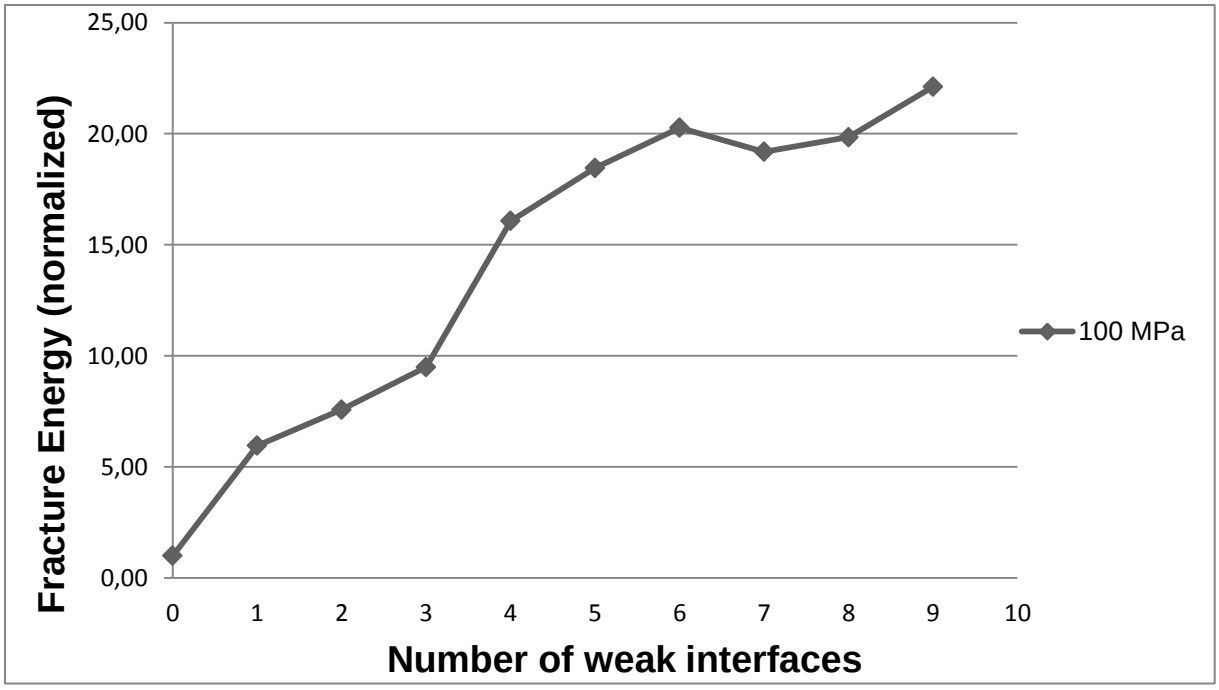


Figure 56: Normalized fracture energy of all SiC-C laminates (with the weak bond strength of 100 *MPa*).

Although the abovementioned comparison is simple, this comparison may be inaccurate due to the fact that the surface energy of SiC and the weak interface are unequal. Therefore, a more accurate estimation of the fracture energy could be conducted by calculating the area under the load-deformation curve, assuming that

all the external work are dissipated by the new surface creation during crack propagation. According to Fig.21 the external work done by the bending test can be obtained by integrating the load with the deformation which for the monolithic SiC material is 0.0285 *J*. Considering the transversal crack length is 392 *μm* and the particles in the BPM have the unit thickness, i.e. the new generated surface area is 2 x 392 *μm* x 1 *m*, therefore the fracture energy of monolithic SiC material (0#) is 36 J/m^2. In the same way, the fracture energy of monolithic graphite is 12 J/m^2. By integrating the load-deformation curves for each laminate, the normalized fracture energy (external work) of the laminates are summarized in Table 9.

Table 9: Normalized fracture energy of all laminates.

	30 MPa	70 MPa	100 MPa	150 MPa	200 MPa	230 MPa	250 MPa	300 MPa
1#	2,7	2,7	2,8	2,8	2,9	1,5	1,6	1,7
2#	2,6	2,7	2,7	3,1	3,1	2,3	2,6	2,4
3#	4,0	4,5	3,6	3,8	3,4	4,9	4,9	3,0
4#	3,3	3,8	3,8	4,5	3,7	3,7	3,9	3,1
5#	2,6	4,0	3,9	4,2	4,5	4,9	4,4	3,1
6#	3,8	4,2	4,1	4,6	4,2	4,9	3,9	3,6
7#	4,7	3,8	4,4	4,7	4,9	5,1	5,4	5,1
8#	3,7	3,9	4,1	4,3	6,2	5,9	4,9	4,2
9#	4,3	4,7	4,9	4,2	4,6	4,2	4,2	4,4

In Fig.57 the normalized fracture energy was plotted against the thickness ratio $t_{lamella}/t_{laminate}$ in order to investigate the influence of the number of the weak interfaces on the fracture energy. For each row in Table 9, the minimum, maximum and average value were chosen to be plotted in Fig.57 and exponential regression lines were fit (with the coefficient of determination R^2 [65, 66]). The fracture energy increases by tendency with the increased number of introduced weak interfaces.

The influence of the weak bond strength on the fracture energy was presented in Fig.58. For each column in Table 9, the minimum, maximum and average value were chosen to be plotted in Fig.58 and polynomial regression lines were fit (with the coefficient of determination R^2 [65, 66]). The maximum of the trend lines were in the range between 100 *MPa* and 200 *MPa*. The trend lines indicated that as the weak bond strength increases the normalized fracture energy diverges.

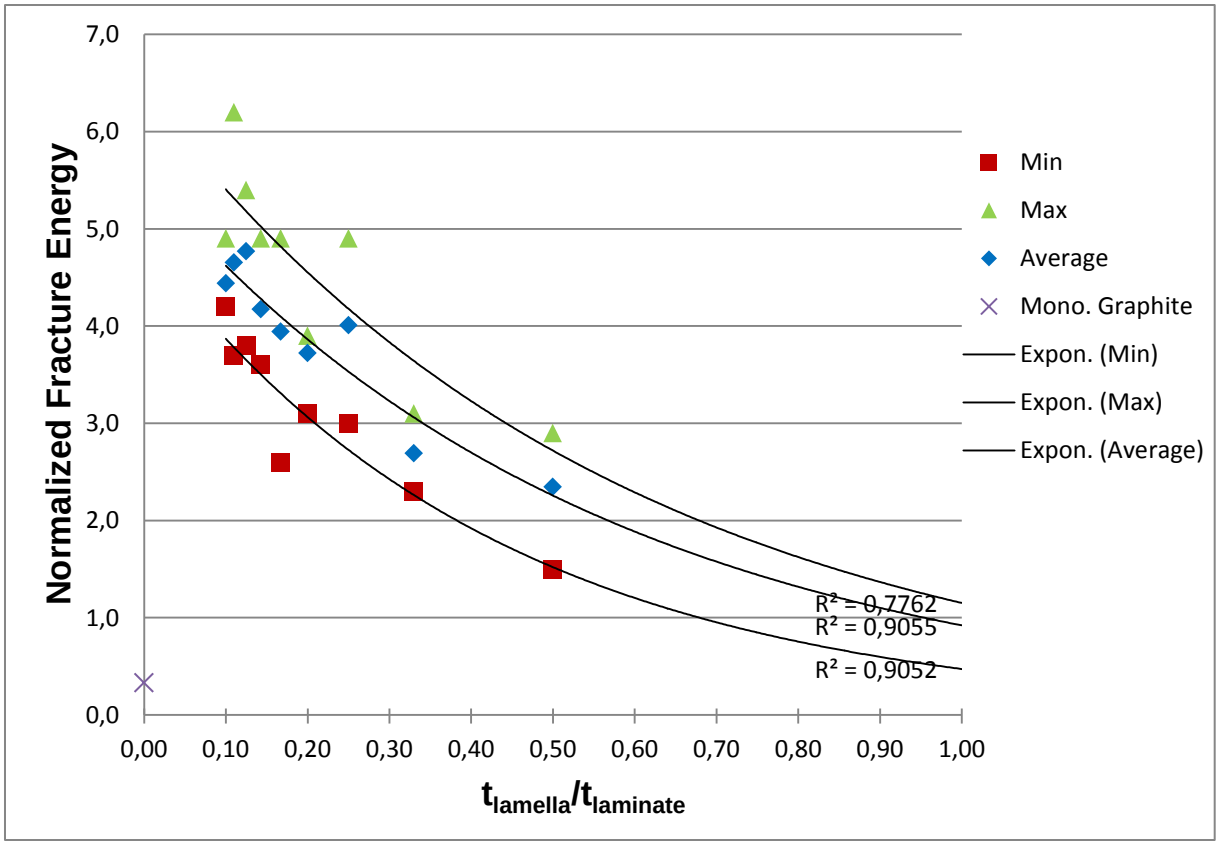


Figure 57: Normalized fracture energy against the thickness ratio $t_{lamella}/t_{laminate}$.

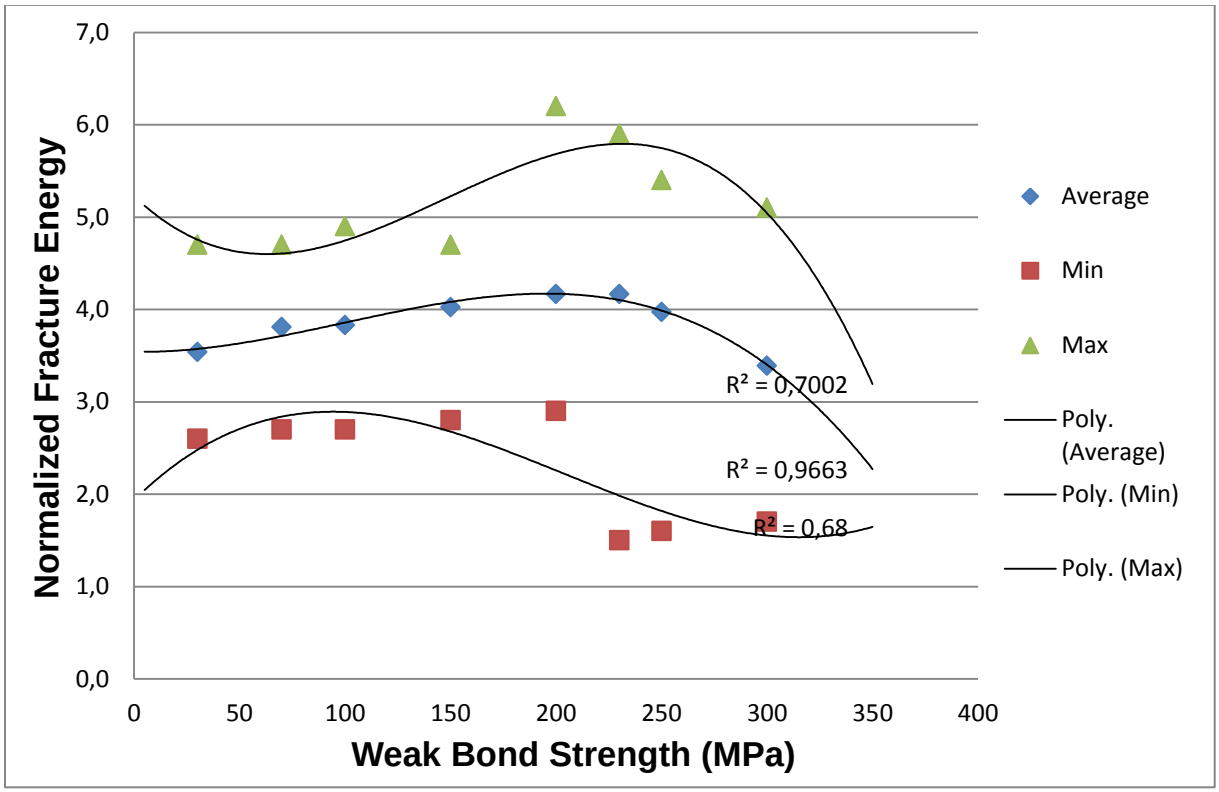


Figure 58: Normalized fracture energy against the weak bond strength.

4. Discussion

Introducing weak interfaces into ceramic matrices to make composites opened a new field in toughening ceramics. Although synthesis of such composites is difficult and expensive, several successful and inexpensive ways to manufacture those composites have been reported [3, 11, 17, 18]. Due to the discontinuous nature of DEM, fracture behaviors in brittle materials can be explicitly modeled. To numerically reproduce and investigate the fracture behaviors of ceramic composites, the feasibility of applying discrete element method (DEM) was examined. Starting with a two dimensional bonded-particle-model (BPM) of SiC, the BPM of SiC-C laminate with graphite as weak interfaces has been created. Up to nine weak interfaces in the SiC-C laminate were investigated; comparisons between those laminates and the normal bulk SiC were made. To date, there is no study available yet, in which the numerical analysis of dynamic crack propagation in the ceramic laminate with weak interfaces was conducted.

In this chapter, the discussion will be divided into three parts. The application of DEM, *i.e.* the synthesis and calibration of BPM for SiC and graphite will be first discussed. Then, results of fracture modeling of SiC-C laminates presented in chapter 3 will be analyzed. At last, some drawbacks of applying DEM on fracture modeling will be mentioned.

4.1 About Discrete Element Method

PFC2D, as the only commercially available DEM codes of its kind, uses an explicit solution scheme that gives stable solutions to unstable processes. This made PFC2D very suitable for solving fracture problems which are no-linear. The using of BPM, which can be implemented in PFC2D, has been first proved by modeling rocks [40]. Although the application of DEM on ceramic fracture is not widespread, DEM studies on ceramic machining were successful [46-49]. Moreover, the fact that the bonds existed at the particle contacts in the BPM offer the possibilities ("paths") for crack growth (energy dissipation), is a favorable feature of DEM in respect of modeling fracture features. Considered all these aspects, DEM has been chosen to perform the study on fracture behaviors of ceramic laminate.

The preparation of BPMs for SiC and graphite is followed by the general procedures which are standardized in PFC2D [38, 39]. To start the preparation of BPM, one of the important parameters is the particle size. There are two considerations regarding to the determination of the particle size. One is the resolution of the model; the other is the match with other model parameters according to Eq. (25). For the resolution, a balance between the resolution of the model and the calculation cost should be achieved. From our experiences and the computational resources available, a limit of 12000 for the total number of particles is first set which is, however, not the capacity limit of the PFC2D itself. Consider the features of laminate structure (*e.g.* high length to width ratio and very high lamella thickness to interlayer thickness ratio) and the desired maximum number of weak interfaces (in this study is 9), meanwhile take the limit of 12000 particles into account, a suitable average particle size of 4.4 *μm* is determined for a particle assembly with a size of 0.4 *mm* x 2 *mm*. The length of time required for the installation of isotropic stress for the particle assembly is very expensive, usually took 480 hours on a *DELL Precision* 470 (Intel® Xeon™ 3.6 GHz, 2GB RAM).

Since there is no direct relation between macro-properties exhibited from the material and micro-properties applied to the particles in the BPM, a calibration is needed before the BPM is used to present the desired material. Usual calibration tests including the unconfined compression, the Brazilian test and the three-point-bending test (for samples with and without a notch) are performed virtually. Well matched elastic modulus, Poisson's ratio and compressive strength of the BPM are obtained from the unconfined compression test, which is used to determine the E_c and k_n / k_s for particles ($\overline{E}_c$ and $\overline{k}_n / \overline{k}_s$ for parallel-bonds). The Brazilian tensile strength of BPM is nearly double of the reported value, this may due to the dependence of Brazilian tensile strength on the ratio of particle size to the diameter of Brazilian test disk [47, 60, 61]. By performing the three-point-bending test, the bending strength of BPM with value of 787 *MPa* which lies in the range from different reports, is obtained [52, 53, 64]. With the notched sample the fracture toughness of 4.8 *MPa* $m^{1/2}$ for the SiC-BPM is calculated. The value is about 10% higher than the assigned value during the determination of the particle size (in chapter 2.1), two facts may be responsible to this. One fact might be that the eventual average particle size of the BPM is slightly larger than the assigned value, since particle sizes are expanded during the preparation of

the BPM (in the steps of isotropic stress installation and "floating" particles elimination). Another fact might be the values of the two non-dimensional constants α and β used in Eq. (25), α=2.26 and β=0.66 were obtained from self-similar tests on the cubically packed assembly of rock [41], nevertheless, the BPM prepared in this study is an irregularly packed particle assembly and no self-similar tests for the BPM were performed. During the calibration of SiC material, parameters reported by Tan *et. al.* [47] are used as reference for determining the micro-properties of the BPM. Although, the calibrated mechanical properties of SiC in this study are not identical to those appeared in that work, they are in the range from other reported data [52, 53, 64].

Depending on the application field, different mechanical properties of graphite are reported [54, 55]. To produce SiC-C laminate, the colloidal graphite is coated on the SiC matrix layers to give the weak interlayer [3, 50]. No high strength value of this graphite interlayer is therefore expected. For our study, we have chosen the mechanical properties of graphite in the range close to the minimum values which are listed in Tab. 3 (in 2.2.2.1). Since the graphite interlayer is thin and weak, the adopted values are suitable to present these features. The determination of the micro-properties of BPM for graphite was as similar as the calibration of SiC. The value for the fracture toughness of graphite was first assumed to be 0.4 $MPa\ m^{1/2}$ (which is close to the minimum value reported for commercial graphite products), then the bond strength for the parallel-bond in BPM of graphite is determined as 100 *MPa*. The E-modulus and Poisson's ratio are calibrated close to the average value (since the scattering of these two properties is small). The bending strength is depended on the bond strength of the parallel-bond, and a corresponded bending strength of 15 *MPa* is obtained. The value of the bond strength is determined by the desired fracture toughness [54], therefore, no further calibration of the bending strength is performed. The Brazilian tensile strength is barely reported for commercial graphite products and is therefore not testified in this study.

It has to be noted that all particles have the unit thickness, which is the assumption of PFC2D. This is suitable for plane strain loading cases. In the fracture modeling of laminate structure, this is even favorable for simplification and saving computation resources.

4.2 About the Fracture Modeling of SiC-C Laminate

The purposes to perform DEM modeling on fracture of SiC-C laminate by using PFC2D are:

1) To examine the feasibility of PFC2D on capturing fracture details and graphically describing the dynamic progress of crack growth in SiC-C laminate;

2) To reproduce fracture features of SiC-C laminate such as "graceful failure", de-bonding, de-lamination, crack deflection and R-curve behavior with a simple and explicit PFC2D model;

3) To establish a parameterized model/procedure for SiC-C laminate and composites which have the similar structure as SiC-C laminate (*i.e.* the layered structure with weak interfaces), with the model design optimizations of the laminate should be achievable.

When modeling the SiC-C laminate, the key feature to be implemented is the thin graphite interlayer (weak interface). Two different ways to implement the weak interface were tested, *i.e.* include and exclude the physical thickness of the thin weak interface. Comparisons between these two different implementations have shown that, the thickness of the thin weak interface can be excluded without significant variation of the modeled mechanical properties. The implementation of excluding the thickness can be easily done by detecting bonds which are located along the weak interfaces (Joint-Plane) and assigning a relatively lower value to their bond strength. It is reasonable and economic to do so. Without considering the thickness of the thin weak interfaces, the BPM of SiC-C laminate becomes simple and economic. If the thickness of the thin weak interface has to be considered, then the required resolution of the BPM has to be increased, *i.e.* the number of particles has to be raised.

Besides, for one weak interface with thickness, two contact interfaces with the neighboring matrices are generated. As a result, the BPM will become complicated and expensive in computation. This treatment for weak interfaces (see also the chapter 2.3) can be verified by introducing one such weak interface into the BPM of SiC. As presented in Figure 21 and 26, the laminate with one weak interface (without thickness) has shown different failure pattern from the monolithic material (graceful

vs. catastrophic). Although the maximum load is nearly unchanged, the deformation of the laminate is increased 2.4-fold. Fracture features of the laminate including de-lamination and crack deflection can be dynamically pictured at the characteristic points (Fig.27). Other laminates have shown similar fracture behaviors. By comparing the modeled fracture features by models which have considered the thickness of the weak interface as illustrated in Fig.22 and 24 to Fig.26, more similar results are obtained in Fig.24 (as the modeled weak interface get thinner, from 30 *μm* to 10 *μm*). Therefore, it can be said that the fracture details are captured explicitly by the simple BPM which implemented the weak interface without the thickness. The model implementing the thickness of the thin weak interface, however, can be applied to study interfacial issues of the laminate. For instance, fiber reinforced composites can be modeled by turning the thin weak interface into thin strong interface (*i.e.* by changing the micro-properties of the particles illustrated as red particles in Fig.18).

The simplicity and explicitness of the BPM of SiC-C laminate are argued above, meanwhile, application of PFC2D on modeling laminate fracture is examined and proved to be feasible. As one of the purposes is to establish a parameterized model for laminate with weak interfaces, up to nine weak interfaces are implemented to the BPM of SiC by using Joint-Planes. Two main parameters of the BPM of SiC-C laminate are the number of weak interfaces and the bond strength value assigned to the weak bonds. The maximum number of weak interfaces that can be implemented is depended on the resolution of the BPM. The accurate data about the bond strength between the weak interface and the matrix is unavailable, thus only assumed values are discussed in this study. Both qualitative and quantitative comparisons are made between these laminates and the monolithic material to investigate the fracture behaviors of SiC-C laminate in detail. Some arguments regarding the parameters of the model are also mentioned.

In order to make it easier to name these different laminate samples, numbers will be labeled according to the number of weak interfaces implemented to the laminates. For instance, sample 0# for monolithic material, 1# for sample with single weak interface, 2# for two weak interfaces and so on.

4.2.1 Qualitative Comparison

As mentioned in 3.1, the phenomenon appeared around point B (the load plateau and/or small load peaks occurred between B and C as like in Fig.24, 26, 28 *etc*.) is due to the position of certain particles in the BPM. When the parallel-bond is oriented crossing the tensile stress field generated during the bending test, and then might cause a so called "break unfavorable" situation. If this appears along/ahead the crack path, the mentioned phenomenon will occur, i.e. the load increased slightly or stopped to drop. The effect of this phenomenon on the simulated fracture feature can be ignored, since during the appearance of the phenomenon no fracture (break of the bond) is happened and the magnitude of the load increase is negligible compare to the maximum load. However, such an occasion is inevitable in a randomly synthesized BPM.

For comparison, the load vs. displacement curve of 0# serves as a reference. In comparison to Figure 21, all the 9 samples (1#~9#) failed gracefully as in Fig.2 [3]. The meaning of graceful failure for ceramic material is significant, since more detectable deformations can be used as signs for failure prediction in engineering. The dynamic process from crack initiation at the notch till to the final failure of the sample is documented by snap-shooting the crack status at certain interested stages. These interested stages are marked by characteristic points in the load diagram for all the samples. Fracture details of all samples are compared qualitatively with the 0# sample.

De-bonding is referred to a bond failure at spot (point failure) while de-lamination is along the weak interface (line failure). Except in 1#, de-bonding at the weak interface nearest to the notch takes place before the crack growth begins, this can be observed from the slight vibration at the end of the line during elastic deformation (O to A). As suggested by Cook and Gordon [4], the interface will de-bond ahead of the main crack to allow deflection when the theoretical tensile strength of the interface is less than 20% of that of the matrix. The weak bond strength was set to be less than 10% of the strength of the SiC matrix (100 *MPa* vs. 1200 *MPa*), and the observed results from the modeled laminates supported the conclusion from Cook and Gordon. Although the interfaces are weak enough, no de-lamination will occur before de-bonding. A higher stress threshold for de-lamination to start is therefore expected.

In this study, de-lamination is found to be a more probable toughening mechanism than crack deflection in the laminate with weak interfaces. The first drastic drop in the loading curve from stage A to B indicated the first crack growth after crack initiation at the notch. According to the ascent of the loading curve after point A in all samples, *e.g.* from B to C (for all laminates) and from D to E (for laminates except 1#, 2# and 3#), pictures of the crack propagation have shown that the main crack has been arrested and de-lamination was the only phenomenon during these periods. In 1#, the load at C only reached 80% of the level at A, whereas in 2# the load reached almost the same level as at A. Loads at point A are related to crack initiation stresses, however, loads for further crack growth (re-initiation) can achieve an even higher level as in samples from 3# to 9#. This may reveal that a minimum amount of weak interfaces must be present for a significant toughening effect.

In 1# and 2#, the strengths of laminates are not increased by introducing weak interfaces, however, the interfaces contributed to the enlarged deformations before the final failure of the samples. From 3# to 9#, R-Curve behavior is clearly demonstrated (Fig.53). Every drastic drop of the loading curve is accounted for crack growth traverse the interfaces. Beside the first crack initiation at the point A, point C, E and G are the points for re-initiation as well. Increases of the load from A to C, even to E (only for 7# and 9#), are proofs for the R-Curve behavior in these laminates. In the sense of toughening, the effectiveness of the de-lamination as toughening mechanism is reduced after the maximum load is reached, then de-lamination can only lead to short ascent or constant of the loading curve. Generally, the crack growth and de-lamination occur alternately as considered also by Phillips *et. al.* in their model [28], however, they may occur simultaneously as well. Unlike the usual load drops are drastic; some observed load drops near the end failure are gradual when crack growth and de-lamination took place at the same time, *e.g.* D to E in 3#, H to I in 4# and E to F in 6#. Near the loading end, the de-lamination mainly results the effect of the gradual decrease of the load rather than toughening.

In Figure 21 the crack propagated rapidly from the notch after initiation and travelled through the whole bulk without any obstacle. In the laminates, however, crack deflection can occur if the crack arrived at the weak interface and has been arrested there. The arrested main crack re-initiates from somewhere else at the interface and propagates further till it meets the next interface. Without de-lamination ahead, crack

deflection cannot occur solely. In the pictures of the dynamic fracture process, crack deflection has been observed to occur by the growth of the interfacial de-bond ahead of the through-thickness crack. From the pictures of crack propagation, it can be seen that the interface in front of crack tip is completely de-laminated before the crack meets the interface. As the main crack arrives at the interface, it first deflects in both directions along the interface. The propagation of the crack along the interface can be treated as de-lamination of the weak interface. When a sufficient amount of de-lamination is achieved, then the second deflection occurs, *i.e.* a new crack re-initiates from the de-laminated interface and travels across the matrix to meet the next interface. The spot where the re-initiation takes place seems random, however, Clegg and Seddon [22] suggested that the re-initiation of the main crack starts from an existing defect within the SiC lamina, which has been later on confirmed by Lee and Clegg [23, 35] in their experiments on poly (methyl methacrylate) laminates. In our model, the interfacial flaws are implicitly implemented. Since pores belong inevitably to a particle assembly, the pores at the weak interface can be treated as interfacial flaws. In some occasions, crack propagates through the interface without deflection, *e.g.* from C to D in 3#, from I to J in 7# and from G to H in 9#.

R-curve behavior was observed in the laminate, the resistance of crack growth was increased as the crack extended (Fig.53). Responsible effects for the R-curve behavior were the de-lamination at the weak interfaces and the crack branching in the SiC lamina (as like in 2#, 5#~9#), which plays a role for the energy dissipation. A quantitative discussion about the R-curve behavior is presented in 4.2.2.

Regarding the thickness of the weak graphite interlayer, two different models are tested. The load-steps diagram and the crack propagation of the laminate which contains a 10 *μm* thick graphite layer is closer to that of the sample 1# (see Fig.24 and Fig.26). The laminate which contains a 30 *μm* thick graphite layer exhibits, however, different patterns of fracture behaviors as the experimentally tested SiC-C laminates (see Fig.22 and Fig.2). In this study, the fracture features of the SiC-C laminate have to be modeled explicitly and simply. Therefore, the model without considering the thickness of the thin graphite interlayer has been employed to model the SiC-C laminates. Depending on different composites, both models can be applied. The model considering the thickness is suitable for composites which has comparable thickness of the constituent layers, *e.g.* the layered Al_2O_3/ZrO_2 composite

[17] and layered piezo-ceramics [67]. In such composites, the fracture at the interfaces between two different constituent layers and the crack growth inside the constituent layer are more concerned. Conversely, the one without the thickness is appropriate for composites which have interlayer much thinner than the matrix layer. In such cases, the thickness of the interlayer is comparable to the radius of the crack tip, thus the consideration of the interlayer is unnecessary. According to our objectives, we proposed the model without thickness to model SiC-C laminates and evaluated the results.

4.2.2 Quantitative Comparison

The calibration of BPM for SiC is based on the technical data of SiC products [52, 53, 64], while the calibration of graphite is based on the range of reported technical/product data [54, 55]. Both BPMs for SiC and graphite are representative. In order to verify the BPM of SiC-C laminate, results from virtual three-point-bending test of notched SiC-C laminates are first compared with the reported experimental data. Afterwards, the self-comparison among the SiC-C laminates (1#~9#) and the monolithic notched SiC sample (0#) is conducted.

Clegg *et. al.* [3] performed three-point-bending test on SiC-C laminates (50 *mm* x 2 *mm* x 2 *mm*, including 9 weak graphite interfaces) and monolithic SiC sample with the same geometry. The average three-point-bending strength of 500 *MPa* and 633 *MPa* were obtained for the monolithic and laminated material, respectively. A 4-fold increase of the apparent fracture toughness (from 3.6 *MPa* $m^{1/2}$ to 15 *MPa* $m^{1/2}$) for the laminated material was achieved. Results of 0#, 8# and 9# were chosen to compare with the test results from Clegg. The bending strength of 0#, 8# and 9# were 530 *MPa*, 657 *MPa* and 724 *MPa* in this study, respectively. The resistance of crack growth for cracks propagating normal to the weak interfaces was increased 3.9-fold for 8# (from 2.6 *MPam*$^{1/2}$ to 10.2 *MPa* $m^{1/2}$) and 4.2-fold for 9# (from 2.5 *MPa* $m^{1/2}$ to 10.5 *MPa* $m^{1/2}$). The deviations may come from: a) the geometry difference, the sample sizes were different; b) the BPM was in 2-dimensional and assumed a unit thickness for all the particles, this has been modeled by a plane-strain loading case; c) the strength of the weak interfaces used in this study were 100 *MPa*, which is reasonable to represent the calibrated graphite (as discussed in 4.1). This may lead to a mismatch with the graphite used by Clegg. It should be noted that the resistance of crack growth increased 3.8-fold for 1# (from 3.9 *MPa* $m^{1/2}$ to 14.9 *MPa*

m$^{1/2}$), which is very close to the absolute values from Clegg (4-fold increase, from 3.6 *MPa m*$^{1/2}$ to 15 *MPa m*$^{1/2}$). The reason was considered to be the similarity of the 1# to the real laminate prepared by Clegg, *i.e.* the thickness of SiC-layer was 200 *μm* in 1# as well as in the real laminate material prepared by Clegg.

The resistance of crack growth was plotted versus the crack extension for each laminate in Fig.53. The first three specimens (1#~3#) have shown a linear increase of the crack growth resistance, since only two values of the resistance at characteristic points are available for them. The other six specimens (4#~9#) have shown a plateau of the curve after the initiation of crack growth. The values of the initial resistance of crack growth (starting from the notch) varied between 2.5 and 4.0 *MPa m*$^{1/2}$, decreased as the number of weak interfaces increased. The plateaus were placed between 8.0 and 12.0 *MPa m*$^{1/2}$, whereas 6# and 8# was the upper and lower boundary, respectively. In 6#, the resistance of crack growth increased 3.7-fold as the crack extended to half thickness of the specimen (200 *μm*). According to Fig.55, the maximum load (1.53-fold, normalized to 0#) among the 9 specimens with the weak bond strength of 100 *MPa* was appeared in 6#. R-curve behaviors also have been observed in other SiC-C laminates with different weak bond strengths, the influence of the weak bond strength on the resistance of crack growth is shown in Fig.54. The reason to plot the resistance values at point A is the data availability for all the laminates to make the common comparison. It has been shown in Fig.54 that the resistance of crack growth will decrease as the weak bond strength is reduced. Moreover, for every weak bond strength, as the ratio $t_{lamella}/t_{laminate}$ approaches 0.1 (corresponds to nine introduced weak interfaces) the resistance approaches to the minimum value. The resistance varied between 2.0 and 4.0 *MPa m*$^{1/2}$ for the laminates with the lowest weak bond strength of 30 *MPa*, whereas, for the weak bond strength of 300 *MPa* the resistance varied only between 3.8 and 4.0 *MPa m*$^{1/2}$. A certain amount of the initial fracture resistance (at point A) reduction is required for the toughening to occur, however, uncontrolled resistance reduction by reducing the weak bond strength and layer thickness may yield adverse results. Fig.54 can provide useful information regarding the initial fracture resistance of the laminate, *e.g.* for the selection of a favorable combination of the weak bond strength and the layer thickness for specific application.

4.2.3 Fracture Energy of SiC-C Laminates

Up to 22-folds of the normalized fracture energy was estimated by counting the length of the transversal crack and the de-laminated crack in the laminate (Fig.56), however, this was inaccurate (overestimated), since this has to assume the surface energy of SiC and graphite are equal. By assuming that all the external work done were consumed/dissipated by the new surface creation during crack propagation, the fracture energy can be accurately estimated by calculating the area under the load-deformation curves. The obtained fracture energy of monolithic SiC is 36 J/m^2, which is in the range of 30-50 J/m^2 reported by Mecholsky [68]. The fracture energy of monolithic graphite is 12 J/m^2, which is close to the value of 13 J/m^2 estimated by using the formula proposed by Knott [69]. Sestakova *et. al.* [70] reported the work of fracture enhancement of about one order of magnitude compared to the monolithic ceramics for weak interface toughened ceramics. According to Table 9, among the modeled laminates the normalized fracture energy is between 1.5 to 6.2-folds, which are in the reported range.

As the two most important parameters of the BPM of SiC-C laminate, the influences of the weak bond strength and number of introduced weak interfaces on the fracture energy were investigated. However, it is difficult to investigate the influence of one of those two parameters by excluding the other. The data in Table 9 have been averaged in a row and column manner, respectively. In the row manner, the influence of the number of introduced weak interfaces on the fracture energy is illustrated in Fig.57. Similarly, the influence of the weak bond strength on the fracture energy is presented in Fig.58 by averaging the data in the column manner. Regression lines with the coefficient of determination R^2 [65, 66] were fit for the curves in Fig.57 and 58. The R^2 varies between 0 and 1, with values closer to 1 indicating better fits and 1 represents a perfect fit [66]. Regression lines can be used to predict the future outcomes based on the available data. As can be seen, if the thickness ratio $t_{lamella}/t_{laminate}$ equals 1, i.e. the laminate turns to be the monolithic SiC, the normalized fracture energy approaches to 1. Conversely, as the thickness ratio $t_{lamella}/t_{laminate}$ infinitely approaches 0, i.e. the laminate turns to be the monolithic graphite, the normalized fracture energy should be infinitely close to the normalized fracture energy of graphite. Although the regression line in Fig.57 captured the tendency well for the $t_{lamella}/t_{laminate}$ range from 0.1 to 0.5, the feature in the range from 0 to 0.1

cannot be predicted by this regression line. However, it can be suggested that the fracture energy should solely increase with the $t_{lamella}/t_{laminate}$ value between 0 and 0.1, and eventually merge with the regression line. Therefore, according to Fig.57 and Table 9 a peak value of the normalized fracture energy can be determined (averagely) as 4.8-folds for the $t_{lamella}/t_{laminate}$ value of 0.125 (7#). Moreover, it has to be noted that in this study the distribution of the weak interfaces was axial symmetric, the $t_{lamella}/t_{laminate}$ should not have values between 0.5 and 1.

In Fig.58, the influence of weak bond strengths on the fracture energy has been presented. Extra weak bond strength of 150 *MPa* was added into Table 9 for the completeness. The polynomial fit (third order) regression lines have shown a maximum in the range of 100 to 200 *MPa* among all the investigated laminates. According to the regression line for the average (with the highest R^2 value), the fracture energy is predicted to approach to a constant value as the weak bond strength closes to 0 (stack of lamellas). Therefore, the weak interface can be quantitatively defined here as the interfaces have strength lower than 200 *MPa*, i.e. the toughening mechanism of "weak interfaces" is only valid for the strengths below this value. As can be predicted by the regression lines, if the weak bond strength further increases the toughening effect of "weak interfaces" should minify.

4.2.4 Parameters of BPM for SiC-C Laminates

In order to generalize the model, the BPM of SiC-C laminate is parameterized. The two most important parameters are: the weak bond strength and the number of weak interfaces. Other geometric parameters as like the length and width of the specimen can be modified depending on the resolution of the model. Nevertheless, new calibration is necessary, if the particle size and fracture toughness are modified, *i.e.* a new material will be modeled. Here, the weak bond strength as one of the main parameters of the BPM is discussed.

In Fig.55, the normalized maximum loads of the laminates (from 1# to 9#) were plotted. By varying the value of the weak bond strength at the weak interface, different curves were obtained. Generally, the tendencies of the curves were similar, as the weak bond strength increased/reduced the curve moved upward/downward. If the laminate contains less than two weak interfaces, the influence of the weak bond strength on the maximum load was ignorable, suggesting that a minimum presence

of the weak interface was the precondition of the toughening mechanism (in respect of increasing the bending strength) to take effect as also argued in 4.2.1.

According to Fig.55, in the case of 100 *MPa*, the whole curve was above 1. In the case of 70 *MPa*, the curve was oscillating around 1. And in the case of 30 *MPa*, the curve was mainly below 1. From this, it can be argued that the weakness of the weak interface has a lower limit. If the bonding strength is lower than this certain limit, the toughening mechanism of the weak interface would disappear. The adopted weak bond strength value of 100 *MPa* has shown somehow the feature of this lower limit, since the minimum of the curve was near 1. As the value of the weak bond strength increased from 100 *MPa* to 230 *MPa*, the curves moved upwards, however, further increase of the value from 250 *MPa* to 300 *MPa* have caused the downwards movement of the curve, as can be seen in Fig.55. A higher limit for the weakness of the weak interface can therefore be determined as 230 *MPa*, which means, above this strength limit the toughening mechanism would also fail. It is reasonable to understand the lower and higher limits. As if the weak interfaces are weaker than the lower limit, the lamellas are then weakly bonded with each other which can be viewed as badly laminated. On the opposite, if the interfaces are stronger than the higher limit, then the laminate is approaching to the bulk material or when the interface are even more stronger than the lamella, the laminate will turn out to be the fiber-/platelet-reinforced material. By studying this parameter, useful and instructive information can be obtained and applied to support the manufacture of the weak interfaces toughened laminates.

4.3 Limitations

Although the features of the dynamic crack growth in ceramic laminates can be reproduced explicitly by the breaking bonds at the particle contacts, one of the drawbacks of using discrete element method on such issues is the efficiency of computation. Since the code records every information of each particle and contact through the whole time-scale, the amount of the data is enormous. Therefore, the resolution of the model in this study is essentially been limited by the available computational resources. Although the specimen size is small, the investigation is still reasonable. In our study, the fracture toughness of the laminate was investigated. As a material property, the fracture toughness should be independent of the specimen size. However, a more sophisticated model (e.g. three-dimensional, finer particle size)

should be employed in the future as far as the computational resources are available. The size of the prepared BPM for SiC-C laminate was in meso-scale, the transferability of this model to the macro-scale real size sample requires further investigation and confirmation.

Unlike the continuous numerical method, macro-properties cannot directly assign to the BPM, therefore a time consuming calibration has to be conducted to obtain reliable micro-properties. Inherent 2-dimensional limitations, *e.g.* only two force components, no out-of-plane force component can be considered in PFC2D simulation, has to be noted. Experimental verification of the findings from the modeled results was not conducted yet, although the model really captures the mechanical properties of the constituent materials of the laminate.

No residual stress or mismatches of the different layers were considered in the DEM model. A study of ceramic-ceramic laminates with residual stresses has been conducted by Sestakova *et. al.* [70]. Other chemical effects, such as the reaction between the graphite and the SiO_2 existing on the surface of the SiC lamina during sintering, which may change the mechanical property of the interface, were excluded. Although Clegg [23] argued that the oxidation of graphite has influence on the toughened laminates, issues regarding the oxidation of the graphite layer are excluded in this work. The properties of graphite employed in our study were calibrated from the reported industrial data of graphite products. However, properties of graphite after oxidation might be subject for modification.

The notch root radius has pronounced influences on the measured value of K_{Ic} [71, 72]. Fischer *et. al.* [73] have shown that the wider the notch root radius was, the higher was the measured fracture toughness. The optimum notch root radius can be related to the so called major micro-structural feature size [74, 75]. In this study, the major micro-structural feature size of the modeled SiC material was unknown; meanwhile the particles in the BPM of the SiC material cannot be related directly to the real micro-structural details of the real SiC material. Thus, the effect of the notch root radius was excluded. The notch root was represented by the parallel bond between the two contacted particles which were positioned at the notch root. Whether this radius is appropriate for the modeled SiC-C laminate requires experimental verification with the measured results. In order to minimize the effect of

the notch root radius, in the BPM the notch root radius was achieved the minimum, *i.e.* the resolution of the BPM (Fig.20).

Due to the high computational cost, all the modeled laminates were based on the same particle assembly, *i.e.* the same particle arrangement. The packing of the particles was irregular and stochastic; however, from the statistical point of view a serial test of the particle assembly should be conducted to investigate the randomness of the particle arrangement. Moreover, the statistical study on the particle arrangement may help to explain and understand the periodic up and down pattern of the curves in Fig.55 and the phenomenon discussed in 4.2.1.

5. Conclusions and Future Work

The dynamic modeling of crack propagation in ceramic laminates by means of the application of discrete element method has been performed. By modeling the notched laminate specimens tested in three-point-bending, the dynamic sequences of the crack growth, de-bonding, de-lamination, crack deflection and R-curve behavior have been determined both qualitatively and quantitatively. Toughening mechanism of the weak interfaces in ceramic laminates has been confirmed. By ignoring the thickness of the thin weak interlayer, the model became simple and retained explicitly, although the computational cost of using discrete element method is relatively high. With the model, further fracture investigations on materials with the laminate-alike structure become possible, *e.g.* bio-inspired materials with the brick-and-mortar structure.

The feasibility of applying BPM to model crack growth in ceramic laminates was approved. Dynamic crack growth progress was fully captured by modeling three-point-bending test of the notched SiC-C laminates. An optimal construction of the laminate was determined in respect of the exhibited mechanical behavior of the modeled laminate. In the following, conclusions from this study are summarized:

(1) Applying BPM to model the fracture behaviors of ceramic laminate is feasible, the "Joint-Plane" employed in the discrete element model has been proved capable to represent the thin weak graphite interlayer.

(2) Qualitative and quantitative comparisons conducted between the BPMs of SiC-C laminate and experimental results revealed that the BPM of SiC-C laminate is reliable to reproduce the fracture behaviors of the real SiC-C laminate.

(3) The weak bond strength and thickness of the lamella determine the initial fracture resistance of the laminate (at point A). A certain amount of reduction of the initial fracture resistance is required for the toughening to occur, however, uncontrolled resistance reduction by reducing the weak bond strength and/or the layer thickness may yield adverse results.

(4) A minimum number of weak interfaces in the laminate is required to increase the bending strength of the laminate.

(5) The strength of the weak interface influences the mechanical behavior of the toughened laminate. In order to have the toughening effect (*e.g.* increased bending strength and R-curve behavior), the strength of the weak interface should be assured to be in the range between 100 *MPa* and 200 *MPa*.

(6) An optimal $t_{lamella}/t_{laminate}$ value of 0.125 is predicted for the SiC-C laminates in respect to the enhancement of work of fracture for 4.8-folds.

(7) The models are parameterized, by varying the bond strength of the interfaces, different type of composites can be modeled, *e.g.* by strengthening the interfaces fiber-reinforced composites can be simulated.

This work offers a good basis for more achievements in the fields of laminate modeling and manufacturing. By expanding the size of the model to the real specimen size, a full comparison is therefore possible between modeled results and the experimental data from the real size sample. Regarding to the manufacturing, this work suggests that SiC material can be toughened with weak interfaces which have the strength in the required range. However, experiments are necessary for finding a suitable way to introduce the weak interface into the matrix. Further applications of DEM to study the layered structure in the ceramic field become convenient. The proposed model can be further developed according to different engineering applications, as like for CO_2 separation membrane's coating layers and gradient laminate materials which have the similar layered structure as the SiC-C laminate. Different designs of the laminate could be analyzed by modifying the thickness of the ceramic lamella and the weak interlayer. Integration of thermal shock and creep simulations into the laminate model should further complete the application of the BPM of laminate.

A new 3-dimensional BPM of ceramic laminates should be realizable, if sufficient computational resources are available. Experimental verifications of the 3D model with the real laminates could be more convincing. With the 3D model, the so called "crumple-zone" which can be observed in MAX-phase materials would be modeled and better understood. More complicated layered structures as in the geo-mimic and bio-mimic materials would be capable to be simulated.

Reference

1. R. Danzer, T. Lube, P. Supancic, R. Damani. Fracture of ceramics. Adv. Eng. Mat. 10, 275-298 (2008).
2. D. Munz, T. Fett. Ceramics: Mechanical properties, failure behaviour, materials selection. Germany: Springer-Verlag (1999).
3. W. J. Clegg, K. Kendall, N. McN. Alford, T. W. Button, J. D. Birchall. A simple way to make tough ceramics. Nature 347, 455-457 (1990).
4. J. Cook, J. E. Gordon. A mechanism for the control of crack propagation in all-brittle systems. Proc. R. Soc. A282, 508-520 (1964).
5. J. E. Gordon. The new science of strong materials. Pitman Publishing, London (1976).
6. P. S. Nicholson. Nature's ceramic laminates as models for strong, tough ceramics. Can. Ceram. Q. 64, 24-30 (1995).
7. M. A. Meyers, P. Y. Chen, A. Y. M. Lin, Y. Seki. Biological materials: Structure and mechanical properties. Prog. Mater. Sci. 53, No.1, 1-206 (2008).
8. J. Aizenberg, J. C. Weaver, M. S. Thanawala, V. C. Sundar, D. E. Morse, P. Fratzl. Skeleton of Euplectella sp.: Structural hierarchy from the nanoscale to the macroscale. Science 309, 275-278 (2005).
9. G. Mayer. Rigid biological systems as models for synthetic composites. Science 310, 1144-1147 (2005).
10. C. Ortiz, M. C. Boyce. Bioinspired structural materials. Science 319, 1053-1054 (2008).
11. S. Deville, E. Saiz, R. K. Nalla, A. P. Tomsia. Freezing as a path to build complex composites. Science 311, 515-518 (2006).
12. A. P. Jackson, J. F. V. Vincent, R. M. Turner. The mechanical design of nacre. Proc. R. Soc. Lond. B 234, 415-440 (1988).
13. H. Gao, B. Ji, I. L. Jager, E. Arzt, P. Fratzl. Biological nanocomposites: nature's design of hard and tough materials. Proc. Nat. Acad. Sci. USA 100, 5597-5600 (2003).
14. P. Fratzl, H. S. Gupta, E. P. Paschalis, P. Roschger. Structure and mechanical quality of the collagen–mineral nano-composite in bone. J. Mater. Chem. 14, 2115-2123 (2004).

15. G. Fu, S. R. Qiu, C. A. Orme, D. E. Morse, J. J. De Yoreo. Acceleration of calcite kinetics by abalone nacre proteins. Adv. Mater. 17, 2678-2683 (2005).
16. B. Ji, H. Gao. Mechanical properties of nanostructure of biological materials. J. Mech. Phys. Solids 52, 1963-1990 (2004).
17. I. Zlotnikov, A. Dorogoy, D. Shilo, I. Gotman, E. Y. Gutmanas. Nanoindentation, modeling, and toughening effects of zirconia/organic nanolaminates. Adv. Eng. Mat. 12, 935-941 (2010).
18. E. Munch, M. E. Launey, D. H. Alsem, E. Saiz, A. P. Tomsia, R. O. Ritchie. Tough, bio-inspired hybrid materials. Science 322, 1516-1520 (2008).
19. J. H. Fendler. Self-assembled nanostructured materials. Chem. Mater. 8, 1616-1624 (1996).
20. C. Sanchez, H. Arribart, M. M. Giraud Guille. Biomimetism and bioinspiration as tools for the design of innovative materials and systems. Nat. Mater. 4, 277-288 (2005).
21. H. M. Chan. Layered ceramics: Processing and mechanical behavior. Annu. Rev. Mater. Sci. 27, 249-282 (1997).
22. W. J. Clegg, L. R. Seddon. The failure of tough ceramic laminates. In 2nd Europ. Conf. on Advanced Materials, Euromat'91 (edited by T. W. Clyne and P. J. Withers), Institute of Materials, Cambridge, UK, Vol. 2, 266-269 (1992).
23. W. J. Clegg. The fabrication and failure of laminar ceramic composites. Acta Metall. Mater. 40, 3085-3093 (1992).
24. S. Baskaran, J. W. Halloran. Fibrous monolithic ceramics: II, flexural strength and fracture behavior of the silicon carbide/graphite system. J. Am. Ceram. Soc. 76, 2217-2224 (1993).
25. S. Baskaran, J. W. Halloran. SiC-based fibrous monolithic ceramics. Ceram. Eng. Sci. Proc. 14, 813-823 (1993).
26. S. Baskaran, J. W. Halloran. Fibrous monolithic ceramics: III, mechanical properties and oxidation behavior of the silicon carbide/boron nitride system. J. Am. Ceram. Soc. 77, 1249-1255 (1994).
27. G. Hilmas, A. Brady, U. Abdali, G. Zywicki, J. W. Halloran. Fibrous monoliths: non-brittle fracture from powder-processed ceramics. Mater. Sci. Eng. A195, 263-268 (1995).

28. A. J. Phillipps, W. J. Clegg, T. W. Clyne. Fracture behaviour of ceramic laminates in bending—I. Modelling of crack propagation. Acta Metall. Mater. 41, 805-817 (1993).
29. C. A. Folsom, F. W. Zok, F. F. Lange. Flexural properties of brittle multilayer materials: I, modeling. J. Am. Ceram. Soc. 77, 689-696 (1994).
30. C. A. Folsom, F. W. Zok, F. F. Lange. Flexural properties of brittle multilayer materials: II, experiments. J. Am. Ceram. Soc. 77, 2081-2087 (1994).
31. V. Gupta, J. Yuan, D. Martinez. Calculation, measurement, and control of interface strength in composites. J. Am. Ceram. Soc. 76, 305-315 (1993).
32. K. Kendall. Transition between cohesive and interfacial failure in a laminate. Proc. R. Soc. London A344, 287-302 (1975).
33. D. Martinez, V. Gupta. Energy criterion for crack deflection at an interface between two orthotropic media. J. Mech. Phys. Solids 42, 1247-1271 (1994).
34. M. Y. He, J. W. Hutchinson. Crack deflection at an interface between dissimilar materials. Int. J. Solids Struct. 25, 1053-1067 (1989).
35. W. Lee, W. J. Clegg. The deflection of cracks at interfaces. Key Eng. Mater. 116-117, 193-208 (1996).
36. P. A. Cundall. In: Proceedings of the Symposium of International Society of Rock Mechanics, vol. 1, Nancy: France, Paper No. II-8 (1971).
37. P. A. Cundall, O. D. L. Strack. A discrete numerical model for granular assemblies. Géotechnique 29, 47-65 (1979).
38. Itasca Consulting Group Inc. PFC2D User's Guide. Minneapolis, Minnesota (2004).
39. Itasca Consulting Group Inc. FISH in PFC2D. Minneapolis, Minnesota (2004).
40. D. O. Potyondy, P. A. Cundall. A bonded-particle model for rock. Int. J. Rock Mech. Mini. Sci. 41, 1329-1364 (2004).
41. D. Robertson, M. D. Bolton. In: Y. Kishino, editor. Powders and grains. Lisse, The Netherlands: Balkema, 623-626 (2001).
42. D. O. Potyondy, J. Autio. In: D. Elsworth, J. P. Tinucci, K. A. Heasley, editors. Rock mechanics in the national interest, vol. 2. Lisse, The Netherlands: Balkema, 1553-1560 (2001).
43. J. Autio, T. Wanne, D. O. Potyondy. In: R. Hammah, W. Bawden, J. Curran, M. Telesnicki, editors. Particle mechanical simulation of the effect of schistosity

on strength and deformation of hard rock. Toronto: University of Toronto Press, 275-282 (2002).

44. W. McGuire, R. H. Gallagher. Matrix Structural Analysis. New York: John Wiley & Sons (1979).
45. T. L. Anderson. Fracture mechanics: Fundamentals and applications. Boca Raton, Florida: CRC Press (1991).
46. Y. Tan, D. Yang, Y. Sheng. Study of polycrystalline Al_2O_3 machining cracks using discrete element method. Int. J. Machin. Tools & Manu. 48, 975-982 (2008).
47. Y. Tan, D. Yang, Y. Sheng. Discrete element method (DEM) modeling of fracture and damage in the machining process of polycrystalline SiC. J. Eur. Cer. Soc. 29, 1029-1037 (2009).
48. S. Jiang, Y. Tan, G. Zhang, R. Peng, D. Yang. DEM simulation and experimental investigation of silicon carbide on pre-stressed machining. Adv. Mat. Res. 126-128, 241- 245 (2010).
49. S. Jiang, Y. Tan, G Zhang, D. Yang. DEM simulation of machining damage in SiC pre-stressing cutting process. Adv. Mat. Res. 177, 165-169 (2011).
50. W. J. Clegg. Design of ceramic laminates for structural applications. Mater. Sci. Tech. 14, 483-495 (1998).
51. D. B. Marshall, J. J. Ratto, F. F. Lange. Enhanced Fracture Toughness in Layered Microcomposites of Ce-ZrO_2 and Al_2O_3. J. Am. Cer. Soc. 74, 2979-2987 (1991).
52. Product information, Accuratus Coporation, Phillipsburg, New Jersey 08865, USA. Website resource http://accuratus.com/silicar.html.
53. Product information, CoorsTek Incorporation, Golden, Colorado 80403, USA. Website resource http://www.coorstek.com/materials/ceramics/carbides.
54. J. Boylan. Smooth Operators: Carbon-graphite materials. Materials World 4 (12), 707-708 (1996).
55. Product information, GTD Graphit Technologie GmbH, TOYO TANSO Group, Langgöns, Hessen 35428, Germany. Website resource http://www.gtd-graphit.de/produkte-werkstoffe/graphit.html.
56. H. Huang. Discrete element modeling of tool-rock interaction. Ph.D. thesis, University of Minnesota, USA (1999).

57. W. Zhang, R. Telle, J. Uebel. R-curve behaviour in weak interface-toughened SiC-C Laminates by discrete element modelling. J. Eur. Cer. Soc. 34, 217-227 (2014).
58. W. Zhang, M. Titze, B. Cappi, D. C. Wirtz, R. Telle, H. Fischer. Improved mechanical long-term reliability of hip resurfacing prostheses by using silicon nitride. J. Mater. Sci.: Mater. Med. 21, 3049-3057 (2010).
59. E. Özkol, W. Zhang, J. Ebert, R. Telle. Potentials of the "Direct inkjet printing" method for manufacturing 3Y-TZP based dental restorations. J. Eur. Cer. Soc. 32, 2193-2201 (2012).
60. R. C. Yu, G. Ruiz, A. Pandolfi. Numerical investigation on the dynamic behavior of advanced ceramics. Eng. Frac. Mech. 71, 897-911 (2004).
61. Z. Bazant, E. P. Chen. Scaling of structural failure. Appl. Mech. Rev. ASME 50(10), 593-627 (1997).
62. L. Hermansson, J. Adlerborn, M. Burström. Tensile testing of ceramic materials—a new approach. Amsterdam: High Tech Ceramics, 1161-1167 (1987).
63. A. F. Bower. (2009). Applied mechanics of solids. CRC Press, 583-581 (2009).
64. G. D. Zhan, M. Mitomo, Y. W. Kim. Microstructural control for strengthening of silicon carbide ceramics. J. Am. Cer. Soc. 82, 2924-2926 (1999).
65. N. J. D. Nagelkerke. A note on a general definition of the coefficient of determination. Biometrika 78 (3), 691-692 (1991).
66. C. R. Rao. Linear statistical inference and its application. 2nd edition. New York: Wiley, 1973.
67. R. Bermejo, L. Sestakova, H. Grünbichler, T. Lube, P. Supancic, R. Danzer. Fracture mechanisms of structural and functional multilayer ceramic structures. Key Eng. Mat. 465, 41-46 (2011).
68. J. J. Mecholsky. Evaluation of Mechanical Property Testing Methods for Ceramic Matrix Composites. J. Am. Cer. Soc. Bull. 65, 315-322 (1986).

69. J. F. Knott. Fundamentals of fracture mechanics. London: Butterworths, 134 (1981).

70. L. Sestakova, R. Bermejo, Z. Chlup, R. Danzer. Strategies for fracture toughness, strength and reliability optimisation of ceramic-ceramic laminates. Int. J. Mat. Res. (formerly Z. Metallkd.) 102 (6), 613-626 (2011).

71. T. Nishida, Y. Hanaki, G. Pezzotti. Effect of notch-root radius on the fracture toughness of a fine-grained alumina. J. Am. Cer. Soc. 77, 606-608 (1994).

72. R. Damani, R. Gstrein, R. Danzer. Critical notch-root radius effect in SENB-S fracture toughness testing. J. Eur. Cer. Soc. 16, 695-702 (1996).

73. H. Fischer, A. Waindich, R. Telle. Influence of preparation of ceramic SEVNB specimens on fracture toughness testing results. Dent. Mat. 24, 618-622 (2008).

74. T. Fett, D. Munz. Stress intensity factors and weight functions for one-dimensional cracks. KfK-Report Nr. 5290, Kernforschungszentrum Karlsruhe, Germany, 1994.

75. T. Fett. Notch effects in determination of fracture toughness and compliance. Int. J. Fracture 72, R27-30 (1995).

CURRICULUM VITAE

Person

Name:	Zhang, Wen
Date of birth:	08. 08. 1982
Place of birth:	Hunan, P. R. China
Marital Status:	Married, one child
Nationality:	Chinese

Education

09/2004 - 06/2007:	Master Program of Metallurgical Engineering
	RWTH Aachen University, Germany
	Study major: Mineral Materials
09/2000 - 07/2004:	Bachelor of Inorganic Non-metallic Materials Engineering
	Department of Inorganic Non-metallic Materials Engineering
	University of Science and Technology Beijing, China

Job experience

07/2007 - now :	Research assistant
	Department of Ceramics and Refractory Materials
	Institute of Mineral Engineering
	RWTH Aachen University, Germany
02/2007 - 04/2007:	Practice in CeramTec Ltd.
	Division of Research and Development
	Lauf an der Pegnitz, Bavaria, Germany
07/2003:	Practice in Qinghua Refractories Ltd., Liaoning, China

Abstract

Tough ceramics can be made by introducing weak interfaces which deflect a growing crack. The presence of weak interfaces in a brittle material can cause a consequent increase in the resistance of crack growth. The failure patterns of the toughened ceramics demonstrate the so-called "graceful failure" feature. In order to numerically reproduce the dynamic process of the crack propagation in such toughened ceramic laminates, discrete element method (DEM) is employed to study the crack growth in the SiC-C laminate with the graphite as weak interfaces. The two-dimensional Bonded-Particle-Model (BPM) is employed to model and calibrate the SiC and graphite. Regarding the thickness of the thin interlayer, two different BPMs are testified, and a simple and explicit model is proposed to model the SiC-C laminate. The feasibility of applying BPM to model fracture behaviors of laminate has been verified. By modeling the three-point-bending test of the laminate, fracture behaviors like de-lamination and crack deflection are observed dynamically. The loading curve shows the "graceful failure" feature and significant R-curve behaviors are found in the modeled laminates. It is found out that, for the toughening effect to occur, the strength of the weak interface has to be in a certain range. In order to increase the strength of the toughened laminate, a minimum presence of the weak interface is required.

Crack deflection as toughening mechanism has direct analogues in some biological structures like bone, wood and nacre. With very complex hierarchical designs in their highly sophisticated structure, these materials are generally difficult to mimic and synthesize. From the DEM modeling, effective design optimizations and production suggestions can be gained for the bio-mimic laminate, as like the suitable strength of the weak interface and the optimum number of weak interfaces in respect to certain laminate geometry. With further development of this discrete element model to three-dimensional, other applications would be possible, for instance the dynamic modeling of the crack propagation in fiber reinforced composites and the reproducing and understanding of the complex "crumple-zone" which are observed in MAX-phases.

Zusammenfassung

Keramik kann durch die Einführung schwachen Schnittstellen, die einen wachsenden Riss abzulenken kann verstärkt werden. Die Anwesenheit von schwachen Grenzflächen in einem spröden Material besteht daraus folgende Zunahme des Risswachstumwiderstands. Das Versagen der verstärkten Keramiken zeigen die sogenannten "graceful failure" (nicht katastrophal versagen). Um den dynamischen Prozess der Rissausbreitung in solchen verstärkten keramischen Laminaten numerisch zu reproduzieren, das Risswachstum in den SiC-C Laminat mit dem Graphit als schwache Schnittstellen wird mit Diskreten-Elemente-Methode (DEM) untersucht. Die zweidimensionale Bonded-Particle-Model (BPM) wird für Modellieren und Kalibrieren für die SiC und Graphit verwendet. In Bezug auf die Dicke der dünnen Zwischenschicht, werden zwei verschiedene BPMs getestet, und ein einfaches und explizites Modell ist für die Modellierung von SiC-C Laminat vorgeschlagen. Die Machbarkeit der Anwendung von BPM zu modellieren Bruchverhaltensweisen von Laminat wurde bestätigt. Durch die Modellierung der Drei-Punkt-Biegeversuch des Laminates werden Bruchverhaltensweisen wie Delamination und Rissablenkung dynamisch beobachtet. Die Beladungskurve zeigt die "graceful failure" Eigenschaften und in den modellierten Laminate werden wesentlichen R-Kurve Verhaltensweisen gefunden. Es wird darauf hingewiesen, dass für das Verstärkungseffekt aufzutreten, die Festigkeit der schwachen Schnittstelle muss in einem bestimmten Bereich liegen. Um die Festigkeit des Laminates zu erhöhen, ist eine minimale Präsenz der schwachen Schnittstelle notwendig.

Rissablenkung als Verstärkungsmechanismus hat direktes Analogon in einigen biologischen Strukturen wie Knochen, Holz und Perlmutt. Bei sehr komplexen hierarchischen Designs in ihrer hochentwickelten Struktur sind diese Materialien in der Regel schwer zu imitieren und zu synthetisieren. Aus DEM Modellierung können effektiv Designs Optimierungen und Vorschläge zur Herstellung bio-imitieren Laminat gewonnen werden, wie z.B. die geeignete Festigkeit der schwachen Schnittstelle und der optimalen Anzahl von schwachen Grenzflächen in Bezug auf bestimmte Laminat Geometrie. Mit der Weiterentwicklung dieser Modell (dreidimensionale), würden andere Anwendungen möglich sein, z.B. die dynamische Modellierung der Rissausbreitung in faserverstärkten Verbundwerkstoffen und das Verständnis des komplexen "Knautschzone", die in MAX-Phasen beobachtet werden.